Torque magnetometry studies on the breakdown of the quantum Hall effect

Kathryn Louise Phillips, BSc (Hons)

Submitted in candidature for the degree of
Doctor of Philosophy

June 2004

Department of Physics and Astronomy,
University of Wales, Cardiff

ProQuest LLC
789 East Eisenhower Parkway
P.O. Box 1346
Ann Arbor, MI 48106-1346

Acknowledgements

Many thanks go to my supervisors Martin Elliott and William Herrenden-Harker for their continual support and patient perseverance throughout my studies.

I am indebted to those who have contributed in so many ways to this work: Jeff Trivett for his hours of effort in the workshop on our excellent new probe, Rob Tucker for his extensive help and instruction on all things electrical, Paul Jones for his continual tweaking of my programming muddles, Ian Robinson for his assistance with cryogens and those pesky safety issues (!), Chris Dunscombe and Rhodri Baker for your support and help as well as always making time to find the bits and pieces I've needed. I have been amazed and humbled by the help, support, encouragement and generosity you have offered with your time, equipment and skills; I will always be grateful for your friendly faces and big hearts.

Many thanks also to some friends I have made, most of whom have also helped me technically along the way (those computers again): Dan (thanks for listening), Mei, Rich, Mozz, Owen, Hannah and Dave. You have kept me sane ... just.

Mum, Dad, Keef – thanks for getting me through and keeping my perspective.

Finally, my soul-mate, my rock – I wouldn't have made it without you.

Where then does wisdom come from?
Where does understanding dwell?

The fear of the Lord is the beginning of wisdom;
all who follow his precepts have good understanding.
To him belongs eternal praise.

Job 28 v 20
Psalm 111 v 10

Abstract

Torque magnetometry techniques have been employed to study the quantum Hall effect in several AlGaAs/GaAs-heterostructure two-dimensional electron gas samples at filling factors between 1 and 4. Two magnetometers were employed to acquire measurements for three samples; an existing instrument was used to acquire data for two samples and a novel instrument has been developed in which the output signal sensitivity is increased by ~700% during experiments on a third sample. The third sample was also illuminated *in situ*. The samples exhibit breakdown-like behaviour in two forms. The first is the saturation of the magnetic moment peak size with respect to increasing sweep rate. A simple charge-up model, which treats the charge density of the sample in terms of a capacitance around the edge of the sample, was used to analyse experimental data. Temperature dependence of the longitudinal conductivity is analysed with respect to a published model of Polyakov and Shklovskii. The charge-up time constant, $\tau_c \approx (10 - 10^5)$ seconds, decreased with increasing temperature and was found to follow a straight line when plotted on a logarithmic scale against temperature. Characteristic temperatures extracted from the data lie in the range $T_0 \approx (0.2 - 2.0)$ Kelvin. Decay time measurements were performed to acquire the decay time constant τ_d. Two regimes of decay were observed, the first exhibiting a time constant of the order of several seconds followed by a second phase with a much larger time constant many minutes or hours. The second form of breakdown was demonstrated as a type of noisy breakdown clearly observed at filling factor 2 in two samples. This noise, of the form of sudden jumps followed by more gradual growth, was interpreted using an edge charge-up model and is thought to be consistent with the sand-pile model of the theory of self-organised criticality. As a result the frequency of occurrence of noisy jumps as a function of their particular size is seen to follow a power law. Time constants of individual noise jumps were found to lie mainly in the range (1–10) seconds.

Contents

Chapter 1: Introduction

This thesis concerns measurements taken on a modulation-doped semi-conductor heterojunction. If electrons or holes in a sample are confined to less than three dimensions then the sample is known as a low-dimensional system. An example of such a system is that of the two-dimensional electron gas (2DEG), a commonly used and investigated structure with a reduced sample thickness, which restricts the charge carriers to a thin film. Examples of 2DEGs are found in the metal-oxide field-effect transistor (MOSFET) and the semiconductor heterojunction, the interface between two separate semiconductors. Confinement of the space within which carriers can move modifies the density of states (DOS) in energy, the number of allowed quantum states, and gives rise to a number of electrical and optical properties. Applying a magnetic field can bring about further adjustments to the DOS. Chapter 2 discusses the 2DEG, its formation and properties, including the density of states with and without a magnetic field applied.

In addition to an applied magnetic field, some effects can only be detected at very low temperature, where the thermal energy of the system has been reduced such that it is comparable with the energy associated with the effect. One effect in particular is that of the quantum Hall effect which also requires the application of a large magnetic field to quantise the energy levels of the sample. In the classical Hall effect a voltage, known as the Hall voltage, is measured perpendicular to both the direction of the applied current and the magnetic field it is placed in. The Hall voltage is directly proportional to the magnitude of the current and the magnetic field. However, when a 2DEG sample displays the integer quantum Hall effect (IQHE), the Hall conductance becomes quantised in units of e^2/h, and for constant current the voltage rises in steps as the magnetic field is swept up. The Hall resistance values observed along the Hall voltage plateaux are related simply and precisely to fundamental constants and an integer. Also in the regions where the Hall resistivity is seen to display plateaux, the longitudinal resistivity approaches zero. Chapter 3 provides more detailed background to the classical and integer quantum Hall effects, and briefly introduces the fractional quantum Hall effect.

The experimental techniques employed to acquire the data contained in this thesis are presented in chapter 4. It is necessary to cool the 2DEG sample to less that around 1.1K and apply a magnetic field; as a result the sample is placed inside a sorption-pumped helium-3 refrigerator which sits within the bore of a 14T superconducting magnet. Torque magnetometry is the technique exploited in order to collect sample data. By sweeping the magnetic field, tiny eddy currents are induced in the sample which then generate magnetic moments. The torque produced between the magnetic moment and the magnetic field cause a small deflection in the sample position and this deflection is measured. Two different probes have been used to gather data on several samples; one was developed by a former

PhD student, while the second has been developed recently. The objective of producing the latest probe was to improve signal-measuring sensitivity and afford enhanced adjustment of the probe mechanics *in situ*. Chapter 4 explains the features and development of this probe in detail.

Three samples were measured in three separate experimental runs (two with the existing probe and one with the new probe) and the data analysed. Chapter 5 serves as an introduction to each sample and reports on the main features and effects demonstrated by each sample in turn.

Chapter 6 discusses the idea of the breakdown of the quantum Hall effect, beginning with a literature review of previously published work. A charge-up model [1, 2] is introduced which describes the mechanisms involved when a 2DEG sample is subjected to a sweeping magnetic field in the quantum Hall regime. Experimental data initially presented in Chapter 5 is then analysed with respect to the model. A number of characteristic parameters, such as temperatures and time constants are brought out of the model and discussed. The model is evaluated and improvements are suggested.

The concept of self-organised criticality, manifest in noisy structure at filling factor 2 for two samples, is the subject of Chapter 7. The topic is introduced as a discussion on complexity, before the more specific sand-pile model is presented. This model is then applied to experimental data, and the mechanism of such noise examined. Further measurements are suggested in order to improve the quality of the existing data.

[1] Y. Lu, M. Elliott, W. G. Herrenden-Harker, K. L. Phillips, A. Usher, A. J. Matthews, J. D. Gething, M. Zhu, M. Henini and D. A. Ritchie, submitted to *Physical Review Letters,* April 2004.

[2] Y. Lu, PhD thesis: *Study of the quantum Hall effect using a contactless method*, Cardiff University, 2002.

Chapter 2: The Two-Dimensional Electron Gas

A low dimensional system is one in which the carriers are confined in one or more dimensions. Examples include thin films, regarded as two dimensional due to their reduced thickness, one-dimensional fine wires where only their length is large, and dots which are zero-dimensional because all three dimensions are small. The properties of reduced dimension systems can differ from bulk ones and the quantum Hall effect is an interesting effect that when discovered in 1980 in a two-dimensional electron gas (2DEG) had not previously been observed in a three-dimensional system.

2.1 Formation of a 2DEG

A 2DEG can be formed at a heterojunction, the interface between two different semiconductors. Through the process of molecular beam epitaxy it is possible to grow semiconductor structures on an atomic level and so exactly pre-define the chemical composition. Consider as an example a layer of $Al_xGa_{1-x}As$ grown epitaxially on GaAs as shown in Figure 2.1.

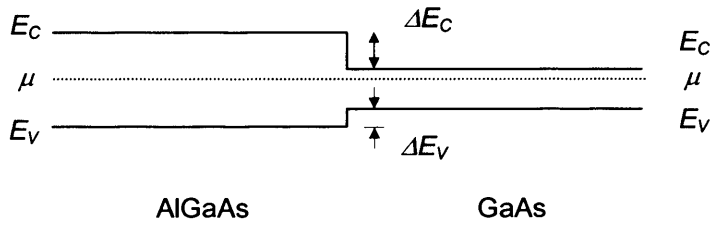

Figure 2.1: *Energy band diagram of an AlGaAs/GaAs heterojuction; no doping.*

The $Al_xGa_{1-x}As$ is undoped, with a larger energy gap than GaAs that depends on the fraction, x, of aluminium to gallium. The Fermi levels, denoted by μ, have been aligned before contact, which produces discontinuities in the conduction and valence band energies, labelled as ΔE_C and ΔE_V, respectively.

It is possible to alter the positions of the Fermi level during the growth process by introducing a dopant, such as silicon, to the AlGaAs, making it n-type. The Fermi level in the AlGaAs has now become much closer to the conduction band than in the GaAs, which is undoped, but will be essentially p-type, with vacant states near the top of the valence band. This situation is shown in Figure 2.2.

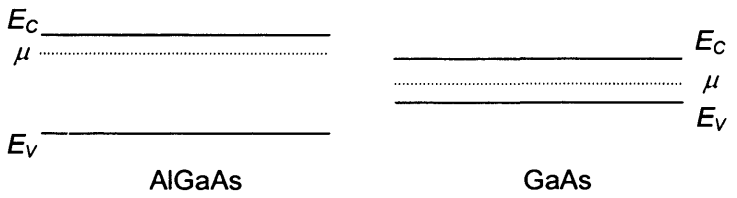

Figure 2.2: *Energy band diagram of an AlGaAs/GaAs heterojunction with doped n-type AlGaAs.*

Mobile electrons from the silicon dopant atoms now move from the conduction band in the AlGaAs to that of the GaAs, filling up the states in the valence band as well as the lower energy states in the conduction band. The silicon atoms are now effectively positively charged and draw the electrons back due to a Coulomb attraction. However the electrons cannot return, due to the potential barrier between the regions. This effect binds the electrons to the interface and produces an electric field. As the charge transfers, the Fermi levels align and the conduction and valence bands bend, leading to a potential well in the conduction band, shown in Figure 2.3.

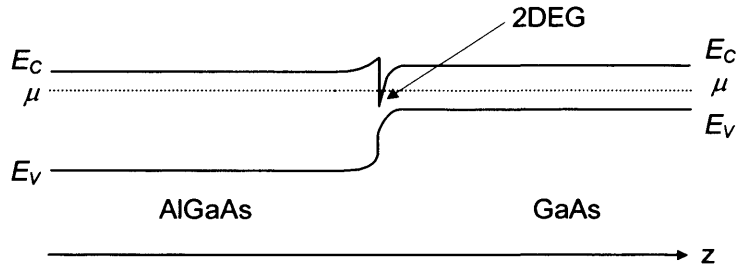

Figure 2.3: *Energy band diagram of an AlGaAs/GaAs heterojunction, showing band bending and the formation of a 2DEG*

If the bands bend so much that the conduction band falls below the Fermi level then states can exist in this new region, producing an electron gas of approximately 10nm in thickness. The electron energies are quantised in the z-direction, which confines the electron motion to a 2D plane.

To reduce electron scattering caused by the dopant in the AlGaAs, an undoped AlGaAs layer is grown between the regions to isolate the 2DEG from the dopants, which increases the mobility beyond that of the sample's bulk mobility.

2.2 Properties of a 2DEG

2.2.1 The electron states of a 2DEG

Assume the electrons in the 2DEG are confined to a film of thickness, *d*, by barriers of infinite potential at *z=0* and *z=d* as shown in Figure 2.4:

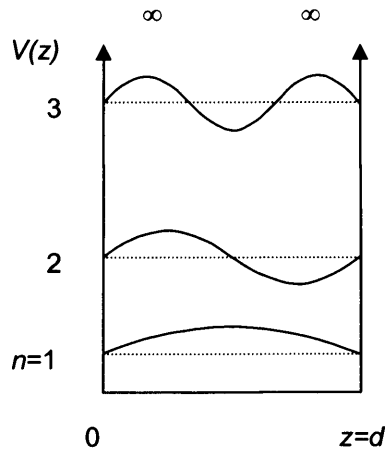

Figure 2.4: *The bound states of a two dimensional infinite square well [1].*

We need to solve the Schrödinger equation in the effective mass approximation:

$$-\frac{\hbar^2}{2m^*}\nabla^2\psi = E\psi \tag{2.1}$$

where m^* is the effective mass of the electron, and ψ and E are the wavefunctions and energies of the electrons. We assume that motion of the electrons in the *x-y* plane is unconfined, and, taking the periodic boundary conditions,

$$\psi(x+L,y+L,z) = \psi(x,y,z), \tag{2.2}$$

the resulting wavefunction has the form,

$$\psi(x,y,z) = e^{ik_x x}e^{ik_y y}\sin(k_z z) \tag{2.3}$$

which is a travelling wave in the *x* and *y* directions and a standing wave in the *z*-direction, and in which k_x, k_y, k_z are wavevectors given by:

$$k_x = \frac{2\pi p}{L} \qquad k_y = \frac{2\pi q}{L} \qquad k_z = \frac{\pi n}{d} \tag{2.4}$$

where *n* is a positive integer and *p* and *q* can be positive and negative integers.

The energy associated with the wavefunction of Equation 2.3 is

$$E = \frac{\hbar^2}{2m^*}\left(k_x{}^2 + k_y{}^2 + k_z{}^2\right) = \frac{\hbar^2}{2m^*}\left(k_x{}^2 + k_y{}^2\right) + \frac{n^2h^2}{8m^*d^2} \tag{2.5}$$

where the second term corresponds to the energy levels of the one-dimensional infinite square well potential, and the first term corresponds to the energy due to motion in the *x-y* plane.

2.2.2 The density of states

To determine the occupation of states of the 2DEG at low temperature we consider the density of states. At low temperature, motion of electrons in the *z*-direction is effectively frozen and the electrons move in a two-dimensional space, the *xy* plane, where the momentum vectors are given by k_x and k_y as before.

We can plot the allowed states in two dimensional k-space as shown in Figure 2.5, where k_x and k_y are the components of the two dimensional vector $\underline{k}$.

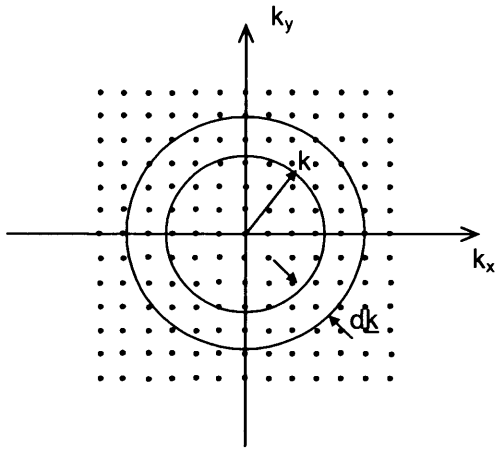

Figure 2.5: *Density of states in k-space of a 2DEG [1].*

Each state can hold two electrons as given by the Pauli Exclusion Principle. They are plotted on a square lattice of side (2π/L) and each state occupies and area of $(2\pi/L)^2$. The area between two concentric circles at $\underline{k}$ and ($\underline{k}$ + $d\underline{k}$) is $2\pi\underline{k}d\underline{k}$, where $\underline{k} >> d\underline{k}$. So the number of allowed states with a wavevector of magnitude $k = (k_x{}^2 + k_y{}^2)^{1/2}$ between $\underline{k}$ and ($\underline{k}$ + $d\underline{k}$) is

$$g(k)dk = \frac{2\pi k dk}{(2\pi/L)^2} = \frac{k}{2\pi}dk \quad \text{per unit area} \tag{2.6}$$

This is the density of states (DOS) in k-space. To rewrite the DOS in terms of energy we must use the relation

$$g(E) = 2g(k)\frac{dk}{dE} \tag{2.7}$$

(where the '2' accounts for the two possible spin states of the electron), and revisit Equation 2.5, i.e.

$$E = \frac{\hbar^2 k^2}{2m^*} + E_n \tag{2.5}$$

where $E_n = \frac{n^2 h^2}{8m^* d^2}$, obviously independent of k.

We differentiate Equation 2.5 with respect to k and substitute it into Equation 2.7 to give the DOS in energy:

$$g(E) = \frac{m^*}{\pi\hbar^2} \tag{2.8}$$

Therefore, the DOS in energy of the 2D electrons is actually independent of energy. When we add together the densities associated with all the bound states we get the total density as shown in Figure 2.6.

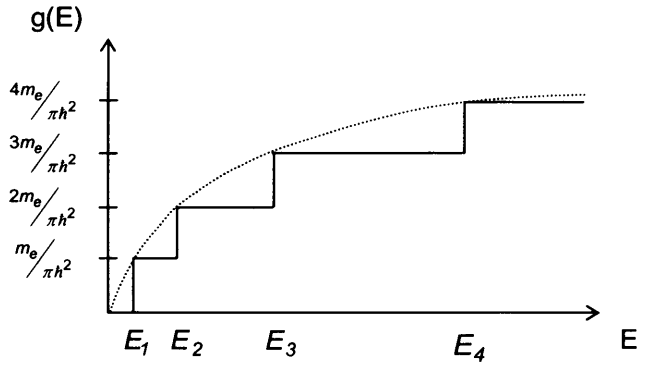

Figure 2.6: *The step-like density of states of 2-D electrons, shown in solid line, including the 3-D density of states superimposed in a dotted line.*

The bound state energies become more closely spaced as the film thickness increases, i.e. as the sample tends towards three dimensions. This makes the steps in the density of states more difficult to observe, and the shape begins to approach the parabolic form of the density of states for 3D free electrons, also shown in Figure 2.6, and given by

$$g(E) = \frac{\left(2m^*\right)^{3/2}}{2\pi\hbar^3} E^{1/2} \tag{2.9}$$

2.2.3 The density of states in crossed magnetic and electric fields

The Quantum Hall regime requires low temperatures and high magnetic fields, so we reconsider the occupation of electron states of a 2DEG in a confining potential *V(z)* but now with a magnetic field applied in the *z*-direction and a uniform electric field, *E*, in the *y*-direction. We adopt a quantum mechanical approach, first published by Landau in 1930 [2], to solve the Schrödinger equation.

In the presence of a magnetic field the quantum mechanical operator fro a free electron is

$$\underline{p} = \frac{\hbar}{i}\underline{\nabla} + e\underline{A} \tag{2.10}$$

where *e* is the electronic charge; $\underline{A}$ is defined as

$$\underline{B} = curl\left(\underline{A}\right) = \underline{\nabla} \times \underline{A} \tag{2.11}$$

and is called the magnetic vector potential. There are several possible forms for $\underline{A}$, but in this case we shall use the Landau gauge which produces a magnetic field in the z-direction, i.e.

$$\underline{A} = (By, 0, 0) .$$

We know that

$$\left|\underline{p}\right| = \left(p_x{}^2 + p_y{}^2 + p_z{}^2\right)^{1/2}, \tag{2.12}$$

and so applying Equation 2.11 and breaking the momentum vector up into its constituent parts gives

$$p_x = \frac{\hbar}{i}\frac{\partial}{\partial x} - eBy \tag{2.13}$$

$$p_y = \frac{\hbar}{i}\frac{\partial}{\partial y}$$

$$p_z = \frac{\hbar}{i}\frac{\partial}{\partial z} .$$

The Schrödinger to be solved is written as

$$\frac{1}{2m^*}\left[-\hbar^2\frac{\partial^2}{\partial x^2} + 2i\hbar eBy\frac{\partial}{\partial x} + e^2B^2y^2 - \hbar^2\frac{\partial^2}{\partial y^2} - \hbar^2\frac{\partial^2}{\partial z^2}\right]\psi + V(z)\psi + eEy\psi = \mathrm{E}\psi . \tag{2.14}$$

where E is the electric field and E is the energy eigenvalues. If we use a trial solution of the form $\psi = e^{ik_x x}\varphi(y)u(z)$, the motion in the z-direction can be separated to give sub-bands which are the eigensolutions of

$$\left(-\frac{\hbar^2}{2m^*}\frac{\partial^2}{\partial z^2}+V(z)\right)u(z)=\varepsilon u(z) \tag{2.15}$$

with energy eigenvalues ε_i. Therefore, we can write

$$\left(-\frac{\hbar^2}{2m^*}\frac{\partial^2}{\partial y^2}+\frac{m^*\omega_c{}^2}{2}\left(y-\frac{\hbar k}{m^*\omega_c}\right)^2+eEy\right)\varphi(y)=(\mathrm{E}-\varepsilon_i)\varphi(y)\,. \tag{2.16}$$

This can be written in the form of a 1-dimensional simple harmonic oscillator, moving in the y-direction, as

$$\left(-\frac{\hbar^2}{2m^*}\frac{\partial^2}{\partial y^2}+\frac{m^*\omega_c{}^2}{2}\left(y-\left(\frac{\hbar k}{m^*\omega_c}-\frac{eE}{m^*\omega_c{}^2}\right)\right)+\frac{\hbar kE}{B}-\frac{m^*E^2}{2B^2}\right)\varphi(y)=(\mathrm{E}-\varepsilon_i)\varphi(y)\,, \tag{2.17}$$

where y_k, the centre of motion, is given by

$$y_k=\frac{\hbar k}{m^*\omega_c}-\frac{eE}{m^*\omega_c{}^2}=\frac{\hbar k-m^*v_d}{eB}\,, \tag{2.18}$$

and $v_d = E/B$ is the classical drift velocity. Therefore the full solutions for Equation 2.17 are now given as

$$\mathrm{E}=\left(n+\tfrac{1}{2}\right)\hbar\omega_c+eEy_k+\tfrac{1}{2}m^*v_d{}^2+\varepsilon_i \tag{2.19}$$

with n = 0, 1, 2... etc.

Thus the motion of the free electron is a superposition of a cyclotron motion and a drift motion with constant velocity v_d, perpendicular to both the magnetic and electric fields. The energy of the electron is now quantised; each different n-value is known as a Landau level and includes a contribution from the electrostatic potential and a kinetic energy term. When the electron spin is taken into account, each level splits into two. This is known as Zeeman splitting and requires an extra term in Equation 2.22, which becomes

$$E = \left(n + \tfrac{1}{2}\right)\hbar\omega_c + eEy_k + \tfrac{1}{2}m^* v_d^{\,2} + \varepsilon_i \pm \frac{1}{2}g^*\mu_B \qquad (2.20)$$

with g^* is the effective Landé g-factor =0.44 for GaAs (2.0024 for the free electron), and μ_B = Bohr magneton = 9.27×10^{-24} J/T.

It can be seen from Equation 2.20 that not only do the energy levels depend on the magnetic field, but, interestingly, the separation between them does also, through the relationship between the cyclotron frequency ω_c, and the magnetic field B, given by

$$\omega_c = \frac{eB}{m^*}. \qquad (2.21)$$

The first term in Equation 2.23 gives energy levels known as Landau levels. The formation of these levels is the result of a redistribution of electron states in the electron gas. It is possible to compare Equations 2.5 and 2.23 to identify the Landau rings in the xy plane:

$$\frac{\hbar^2}{2m}\left(k_x^{\,2} + k_y^{\,2}\right) = \left(n + \tfrac{1}{2}\right)\hbar\omega_c. \qquad (2.22)$$

This equation gives a set of concentric cylinders, parallel to the z-axis (and field direction), which appear as rings on a 2D plot. Figure 2.7 shows the effect of a magnetic field on the electron states [1]. Figure 2.7(a) shows a section of k-space perpendicular to the z-axis with the simple square lattice of electron states that occurs in the absence of a field. The Landau rings are superimposed. In the presence of a magnetic field the states condense to the nearest level, shown in Figure 2.7(b), but the average density of states remains unchanged.

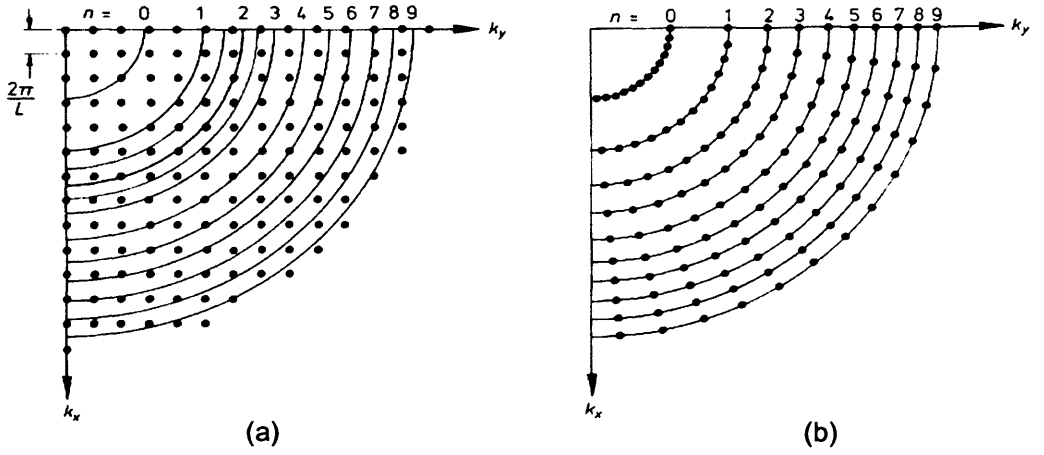

Figure 2.7: *Landau quantisation, (a); in zero magnetic field the states sit in the lattice structure (Landau levels superimposed), (b); on application of a magnetic field the states condense onto the Landau rings*

To find the area, A, of the n^{th} Landau ring,

$$A = \pi k^2 , \tag{2.23}$$

we apply Equations 2.24 and 2.25 to get

$$A = \pi\left(k_x{}^2 + k_y{}^2\right) = \left(n + \tfrac{1}{2}\right)\frac{2\pi eB}{\hbar} . \tag{2.24}$$

This also implies that the area between the n^{th} and $(n+1)^{th}$ ring is

$$\Delta A = \frac{2\pi eB}{\hbar} . \tag{2.25}$$

To find the density of states in k-space we repeat the procedure used earlier to derive Equation 2.6. Then, the density of states, per unit area and accounting for spin, is

$$g(k) = \frac{2\pi eB/\hbar}{\left(2\pi/L\right)^2} = \frac{eB}{h} . \tag{2.26}$$

We can plot the density of states against energy (Equation 2.22), which is shown in Figure 2.8a:

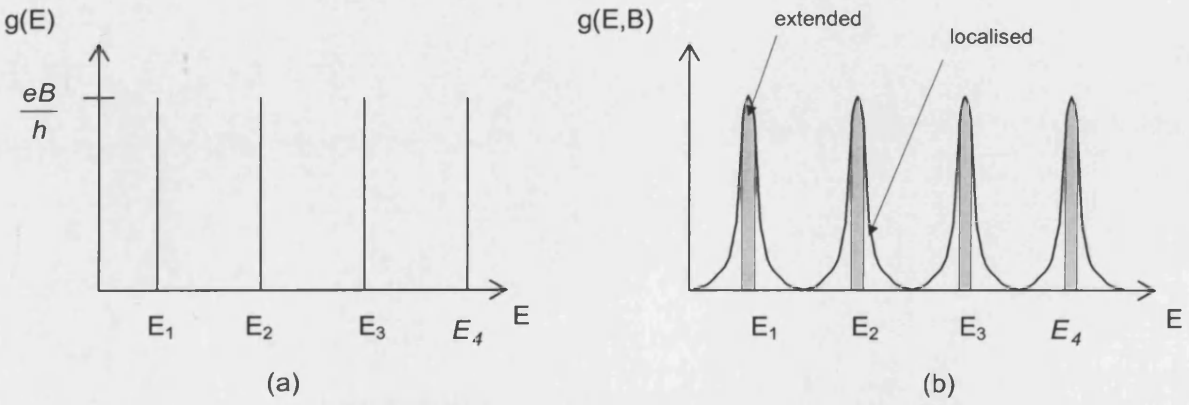

Figure 2.8: *The Density of states as a function of energy, (a); in an ideal 2DEG at 0 Kelvin, (b); in a real 2DEG, where the delta functions broaden out into peaks.*

This assumes a perfect sample and a temperature of zero Kelvin, and the plot consists of a series of delta functions. However, for real samples and non-zero temperatures the delta functions broaden out. They still peak at the energies given by Equation 2.22, but there exists some overlapping from neighbouring peaks. This broadening is shown in Figure 2.8b. The states close to the peaks, *extended states*, are thought to extend throughout the crystal and hence contribute to the conduction through mobile electrons. States nearer the troughs are known as *localised states* and do not contribute to conduction.

Conduction is thought to occur through an electron hopping from one essentially localised state to another. This can only occur if there are states close to the electron to which it can move. If the density of states falls below a particular value there will be less chance of the electron being able to move so conduction decreases significantly at these states.

The form of the peaks is dependent on temperature, level of disorder and magnetic field. As the temperature falls, level of disorder reduces or magnetic field increases, the broadening lessens and the peaks will become more prominent.

2.3 References

[1]. For a review see J R Hook & H E Hall, *Solid State Physics (Second Edition)*, Wiley (1991)

[2]. L D Landau, Z. Phys **64**, (1930), p629

Chapter 3: The Hall Effect

The Hall Effect was discovered by Edwin Hall in 1879, and provides a demonstration of the forces acting on the moving charges in a conductor positioned within a magnetic field.

3.1 The Classical Hall Effect

Consider a classical 3-dimensional Hall bar positioned in a magnetic field with an electric current passing through it in the directions shown in Figure 3.1:

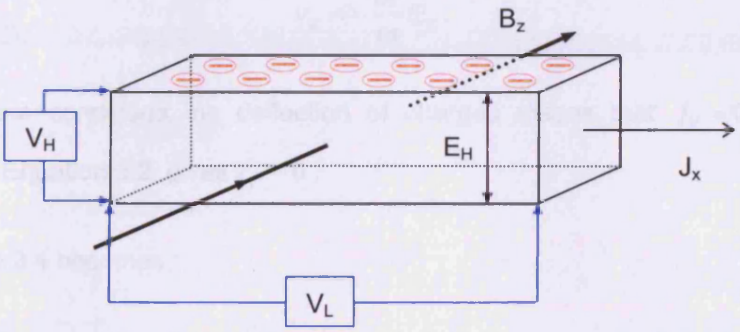

Figure 3.1: *The Hall Bar*

The current, $\underline{J_x}$, flows in the x-direction and a magnetic field, B_z, is perpendicular to the plane of the bar, in the z-direction. A charge, q, moving through the bar in a magnetic field $\underline{B}$ experiences the net force,

$$\underline{F} = q\left(\underline{E} + \underline{v} \times \underline{B}\right) \tag{3.1}$$

where $\underline{v}$ is the velocity of the electron. The direction of the force is perpendicular to both $\underline{v}$ and $\underline{B}$, and as the electrons travel they will be deflected towards the top of the bar, as illustrated. This collection of charge produces an electric field across the sample, called the Hall field, E_H. This field continues to grow until the force it produces exactly equals that provided by the Lorentz force. When this occurs no further charge collects along the top of the bar and the potential difference between top and bottom surfaces is denoted by V_H, the Hall voltage.

The current density is given by

$$\underline{j} = nq\underline{v} \tag{3.2}$$

and the drift velocity,

$$\underline{v} = \frac{\tau}{m}\underline{F}, \tag{3.3}$$

where τ is the time between scattering events.

Expanding Equation 3.3 into its components, and substituting for $\underline{F}$ from Equation 3.1:

$$v_x = \frac{e\tau}{m}\left(E_x + v_y B_z\right); \tag{3.4}$$

$$v_y = \frac{e\tau}{m}\left(E_y - v_x B_z\right); \tag{3.5}$$

$$v_z = -\frac{e\tau}{m}E_z. \tag{3.6}$$

Under equilibrium conditions, no deflection of charges means that $j_y = 0$ which, when substituted into Equation 3.2, gives $v_y = 0$.

Hence Equation 3.4 becomes

$$v_x = \frac{e\tau}{m}E_x, \tag{3.7}$$

and for Equation 3.5,

$$0 = \frac{e\tau}{m}\left(E_y - v_x B_z\right),$$

which implies

$$E_y = v_x B_z = \frac{e\tau}{m}E_x B_z. \tag{3.8}$$

The current density can also be defined using Ohm's law:

$$\underline{j} = \underline{\underline{\sigma}}\,\underline{E}$$

where $\underline{\underline{\sigma}}$ is the conductivity tensor

$$\underline{\underline{\sigma}} = \begin{pmatrix} \sigma_{xx} & \sigma_{xy} \\ \sigma_{yx} & \sigma_{yy} \end{pmatrix}. \tag{3.9}$$

The classical diagonal conductivity σ_{xx} is given by

$$\sigma_{xx} = \frac{ne^2\tau}{m} \tag{3.10}$$

for carrier concentration, n, and the definition of the Hall coefficient, R_H, is

$$R_H = \frac{E_y}{j_x B_z}, \tag{3.11}$$

so

$$R_H = \frac{1}{ne}, \tag{3.12}$$

enabling the carrier concentration to be calculated from a measurement of the Hall coefficient.

3.2 The Quantum Hall Effect

3.2.1 The Integer Quantum Hall Effect

The integer quantum Hall effect was originally discovered in 1980 by Klaus von Klitzing [1], who observed a change in the properties of 2D electron systems when subjected to low temperatures and high magnetic fields.

Consider the rectangular film in Figure 3.2:

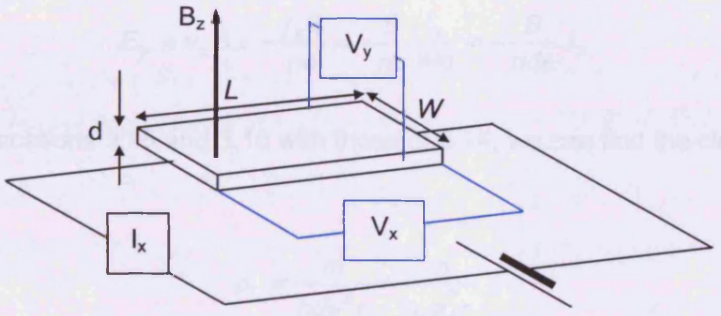

Figure 3.2: *Diagram to show geometry of Hall Effect measurement in a 2D electron system [2].*

It has dimensions W and L, and a thickness d, and a current I_x is passed in the x-direction. When a magnetic field (B_z) is applied in the z-direction, the longitudinal and transverse voltages (V_x and V_y) are measured by voltmeters as shown.

Using the relation

$$E = \frac{Voltage}{Length},$$

where E is the electric field, we can compute

$$E_x = \frac{V_x}{L}$$
$$E_y = \frac{V_x}{W}. \tag{3.13}$$

Equations 3.14 can be rewritten

$$E_x = \rho_L J_x$$
$$E_y = \rho_T J_x \tag{3.14}$$

where J_x is the 2D current density, defined as the current per unit width of film ($J_x = I_x/W$) and ρ_L and ρ_T are the longitudinal and transverse resistivities respectively.

Returning to the previous section we can rewrite Equation 3.7, and using the equation for current density

$$j_x = -nev_x,$$

then

$$E_x = -\frac{m}{e\tau}v_x = \frac{m}{e\tau}\frac{j_x}{ne} = \frac{m}{ne^2\tau}\frac{I_x}{Wd} = \frac{m}{nde^2\tau}J_x \tag{3.15}$$

Also, using Equation 3.5 and the condition that $v_y = 0$ in equilibrium,

$$E_y = v_x B = -\frac{j_x B}{ne} = -\frac{B}{ne}\frac{I_x}{Wd} = -\frac{B}{nde}J_x \tag{3.16}$$

If we compare Equations 3.15 and 3.16 with those of 3.14, we can find the classical relations for ρ_L and ρ_T:

$$\rho_L = \frac{m}{nde^2\tau} = \frac{m}{n_s e^2\tau}$$
$$\rho_T = -\frac{B}{nde} = -\frac{B}{n_s e} \tag{3.17}$$

n_s is the electron density and is related to the 3D (volume) density, n, by $n_s = nd$.

It can be seen that ρ_L is independent of B (i.e. will remain constant in a varying field), and that ρ_T is linearly dependent on B. However, when we measure ρ_L and ρ_T as a function of B we find that the experimental results do not meet classical expectations, as shown in Figure 3.3:

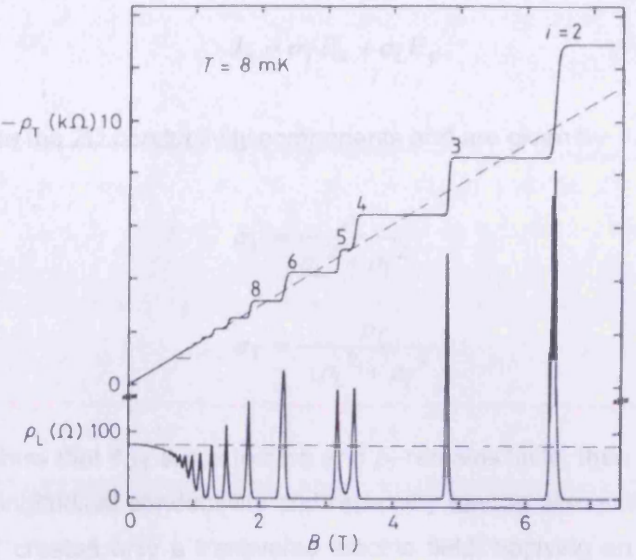

Figure 3.3: *The Integer Quantum Hall Effect [3]. The behaviour of the transverse and longitudinal resistivities can be seen, as well as those predicted by Equations 3.19 (shown as dotted lines). The sample was a typical GaAs-$Ga_{0.71}Al_{0.29}As$ heterostructure and the integer values correspond to the values of ρ_T as given in Equation 3.20.*

The transverse resistivity, ρ_T, which quantifies the Hall effect, rises in steps as the magnetic field increases. These horizontal steps are very flat and the values to which they move are related simply to fundamental constants:

$$\rho_T = -\frac{h}{\nu e^2} \tag{3.18}$$

where ν is an integer (shown as i in Figure 3.3) and is known as the Landau filling factor. This is the *integer quantum Hall effect.*

The longitudinal resistivity, ρ_L, also displays odd behaviour. At the times that ρ_T reaches a flat region, ρ_L is near zero; when ρ_T sharply steps up to the next flat region, ρ_L displays a fine peak.

One might think that if the longitudinal resistivity, ρ_L, tends towards zero then the longitudinal conductivity would tend to infinity, but this is not actually so.

We can generalise Equations 3.14 for arbitrary current flow in the xy plane:

$$\begin{aligned} E_x &= \rho_L J_x - \rho_T J_y \\ E_y &= \rho_T J_x + \rho_L J_y \end{aligned} \tag{3.19}$$

To obtain current density we can invert the above equations

$$J_x = \sigma_L E_x - \sigma_T E_y$$
$$J_y = \sigma_T E_x + \sigma_L E_y \tag{3.20}$$

where σ_L and σ_T are the 2D conductivity components and are given by

$$\sigma_L = \frac{\rho_L}{\rho_L{}^2 + \rho_T{}^2}$$
$$\sigma_T = -\frac{\rho_T}{\rho_L{}^2 + \rho_T{}^2} \tag{3.21}$$

These equations show that if ρ_L tends to zero and ρ_T remains finite, then σ_L also tends to zero. This means that longitudinal conductivity and resistivity tend to zero simultaneously. Hence, applying a current creates only a transverse electric field; applying an electric field creates only a transverse current.

To understand this effect we now look to the electron states again, but in the presence of a magnetic field. Figure 3.4 shows the changes in the Landau levels as the magnetic field is increased.

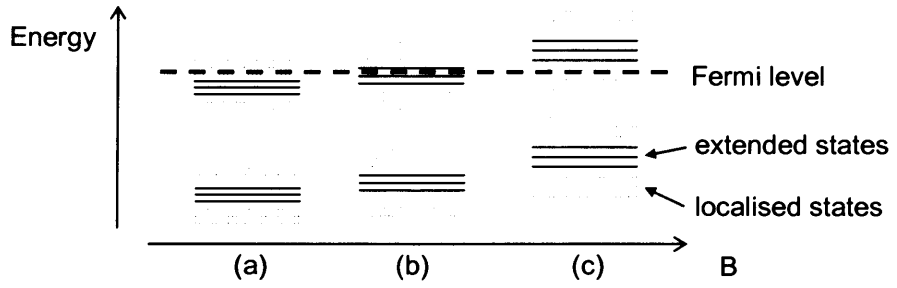

Figure 3.4: *Movement and behaviour of the Landau levels in an increasing magnetic field. The Fermi level remains constant.*

The Fermi level lies amongst a set of localised Landau states in the uppermost band. As the magnetic field is increased the levels increase in energy, as does the separation between them; the Fermi level remains still and so the localised states rise up and above it. The density of states of each level also increases with increasing magnetic field, so as the upper localised states pass out through the Fermi level, they empty as the electrons drop down to fill the newly available states in the lower levels. However, because the localised states do not contribute to conduction in the material, the depopulation of the states does not lead to any change in current flow. Hence the Hall resistance is unchanged and forms a plateau as given by Equation 3.18.

Increasing the magnetic field further causes the states to rise until the Fermi level enters a set of extended states, as shown in Figure 3.4b. As before the levels continue to empty of states as they pass over the Fermi level. Because these extended states do contribute to

conduction, their depopulation causes a drop in current, which is manifest in an increase of sample resistance. We can check this rise of resistance in the experimental data in Figure 3.3.

When all the extended states have passed over the Fermi level, we reach the next set of localised states, shown in Figure 3.4c. The resistivity again forms another plateau. As the magnetic field continues to increase this pattern repeats provided there is one full Landau level (i.e. one set of extended states, and two localised) below the Fermi level.

The density of states of a Landau level in a magnetic field is given by

$$g(E,B) = \frac{eB}{h}, \tag{3.22}$$

as shown in Figure 2.8. A Landau level is wholly occupied when $n_s/g(E,B)$ is equal to a whole number, ν, the Landau level filling factor. Combining this with Equation 3.22 gives

$$\nu = \frac{n_s h}{eB} \tag{3.23}$$

and when this relation for ν is inserted into Equation 3.18, we get the relation for the transverse resistivity, ρ_{xy}, in terms of fundamental constants:

$$\rho_{xy} = \frac{h}{\nu e^2}. \tag{3.24}$$

This is the same result for quantum Hall resistivity obtained from quantum theory. At precisely this value of ρ_{xy}, ρ_{xx} should vanish.

Useful applications of the quantum Hall effect are limited due to the requirement of such low temperatures and strong magnetic fields. However, the precise manner in which the Hall plateaus can be calculated purely from fundamental constants means that the quantum Hall effect can be used to define the electrical resistance standard where the ohm, R_K, is defined as

$$R_K = \frac{h}{e^2}.$$

3.2.2 The Fractional Quantum Hall Effect

In 1982 Tsui *et al* [4] made the first observations of what is now termed the fractional quantum Hall effect (FQHE) in an AlGaAs-GaAs heterojunction. It was previously thought that the quantised Hall conductivity could only take values of integer multiples of e^2/h, but the results of Tsui *et al* showed plateaus at 1/3 and 2/3 of e^2/h, implying that less than one whole level is occupied. Conversely, the Hall resistivity could be denoted as

$$\rho_{xy} = \frac{h}{\nu e^2} \tag{3.25}$$

where ν is certain rational fractions, for instance m = 1/3, 2/3. More recent FQHE data is displayed as an example in Figure 3.5.

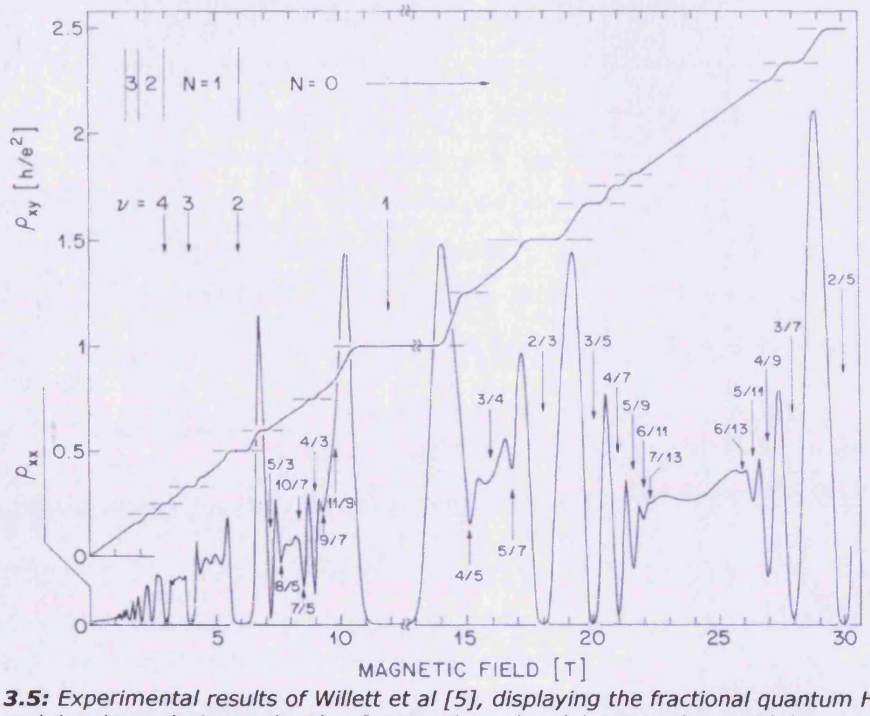

Figure 3.5: *Experimental results of Willett et al [5], displaying the fractional quantum Hall effect. Each peak has been designated with a fractional number (always with an odd denominator) as labelled.*

These results were unexpected because theory up until that point had only concerned single electron interaction and it could not explain this new result. It was now thought that electron-electron interaction would have to be considered to explain the FQHE, a successful example being the composite fermion approach [6]. However, no definitive model has been established.

3.3 References

[1]. K von Klitzing, G Dorda & M Pepper, Physical Review Letters Vol. 45, 494 (1980).

[2]. J R Hook & H E Hall, *Solid State Physics (Second Edition)*, Chichester: Wiley (1991).

[3]. K. von Klitzing, *Physica B+C*, Vol. 126, 242 (1984).

[4]. D.C.Tsui, H.L.Stormer & A.C.Gossard, *Physical Review Letters* 48, 1559 (1982).

[5]. R. Willett, J. P. Eisenstein, H. L. Stormer, D. C. Tsui, A. C. Gossard and J. H. English, *Physical Review Letters* Vol. 59, 1776 (1987).

[6]. For a review see T.Chakraborty & P.Pietilainen, *The Quantum Hall Effects: Integral and Fractional*, Springer-Verlag (1995)

Chapter 4: Experimental Techniques

To allow the study of the quantum Hall effect, a two-dimensional electron gas (2DEG) sample must be placed in a high magnetic field at very low temperature. This is known as the quantum Hall regime. To achieve this liquid helium cryogenic systems are used to cool the sample and variable magnets in-situ provide a sweeping magnetic field. This equipment is described in section 4.1. As the magnetic field varies, the tiny currents induced in the sample are measured, offering a direct observation of the quantum Hall effect. This is done by a process known as torque magnetometry, explained in section 4.2. Section 4.3 discusses and compares two probes used to study the quantum Hall effect, an existing and previously used probe, and the development of a new and improved one. This section also contains an explanation of signal detection and calibration, and probe sensitivity.

4.1 The Cryogenic System

In order to observe the quantum Hall effect in a 2DEG sample, the sample must be cooled to a temperature of less than around 4K. This is accomplished in the laboratory with the use of an aluminium and glass fibre cryostat, containing a high field superconducting magnet within a cryogen bath space. A Heliox sorption-pumped helium-3 (^{3}He) refrigerator insert is fitted in the centre, and all parts are separated from each other and the laboratory by vacuum chambers and multilayer superinsulation. A basic cross-section schematic of the cryostat is given in Figure 4.1. Such apparatus normally reaches a base temperature of 0.3K, and remains thermally stable up to around 1.2K. To achieve base temperature, the sample is submerged in liquid helium-3 (^{3}He)

4.1.1 Cryostat components

An outer vacuum chamber (OVC) thermally insulates a helium (^{4}He) bath containing the magnet. The magnet itself is made up of two coils, an inner coil of conducting niobium-tin alloy and an outer coil of superconducting niobium-titanium, providing a vertical magnetic field range of (0 – 12)T. A niobium-tin alloy modulation coil is also fitted within the main magnet and offers slight field modulations of ± 0.02T at 500Hz with a suitable power supply. The magnetic field sweep rate is controlled by a Cryogenic Ltd Superconducting Magnet Controller and can lie in the range (0 – 25.18)mTs^{-1}. Using the relation

$$B = 62.69(\mathrm{T/V}) \times V \qquad (4.1)$$

(which is specific to the 14T magnet used in Cardiff) it is possible to convert the voltage, V, measured across a standard resistor on the power supply of the magnet into a value for field, B. A Keithley 195A digital multimeter was used to measure the output voltage. The clear bore through the magnet centre is of diameter 40mm and radiation shields towards the top of

the reservoir space reduce heat transfer between the exterior and the reservoir. It is required that the magnet be completely covered with liquid helium to cause it to function as a superconducting magnet. A lambda point refrigerator is also installed within the cryostat which allows the helium reservoir and the magnet within to be cooled to around 2.2K which extends the upper limit of the magnet field range to 14T (although this facility is not currently exploited). An inner vacuum chamber (IVC) then isolates the helium bath from the experimental helium-3 insert which encloses the sample space.

Within the IVC an activated charcoal sorption pump (or sorb) and a 1Kpot are mounted against the wall of the probe space. The sorb is used to handle gas through adjustment of its temperature and a series of large slots in the wall of the probe space allows the sorb surface to be in direct contact with gas in the sample space. The sorb pumps between temperatures of 4.2K and ~40K, at a rate dependent on the temperature. Above 40K the sorb begins to outgas as the activated charcoal gives off any gas it has previously collected. To warm the sorb, two 68Ω heaters arranged in parallel are fitted to it, and the temperature of the sorb is controlled by balancing the cooling power of liquid helium drawn through the exchanger from the reservoir with the heating power of this heater. A four-terminal resistance measurement of a 270Ω Allen Bradley resistor fitted to the sorb is converted to temperature and then displayed by an Oxford Instruments ITC502 temperature controller, which also powers the heater.

The 1Kpot has a needle valve which is controlled on the top plate, and when opened it fills with liquid helium from the reservoir at 4.2K. By pumping on the 1Kpot and reducing the vapour pressure it is possible to reduce the temperature of the ^{4}He liquid within to ~1K. The 1Kpot can be used to cool the ^{4}He liquid in two ways: single-shot mode and continuous-fill mode. For single-shot mode the 1Kpot is completely filled and then the needle valve closed. The pumping rate is slowly raised to a maximum causing the 1K pot to fall to its lowest possible temperature. This mode is time limited owing to the set volume of ^{4}He available, which when exhausted causes the 1Kpot temperature to rise sharply. Continuous-fill mode allows prolonged use of the cooled 1Kpot by keeping it constantly supplied so that it may never empty. The 1Kpot is cooled as before with the needle valve closed and when the lowest temperature has been reached the needle valve is cracked open, admitting a continuous, if small, flow of ^{4}He liquid. The implication of this method is that the equilibrium temperature of the 1Kpot is always slightly raised compared to that of the single shot method, but it does have the advantage of extended measurement time. A four-terminal resistance measurement of a 470Ω Speer resistor provides a value for the temperature of the 1Kpot and is also displayed on the Oxford Instruments ITC502 temperature controller.

In addition, two further thermometers are fitted inside the cryostat. A second 470Ω Speer resistor is situated on the ^{3}He pot, and a further resistor is located on the base of the helium reservoir.

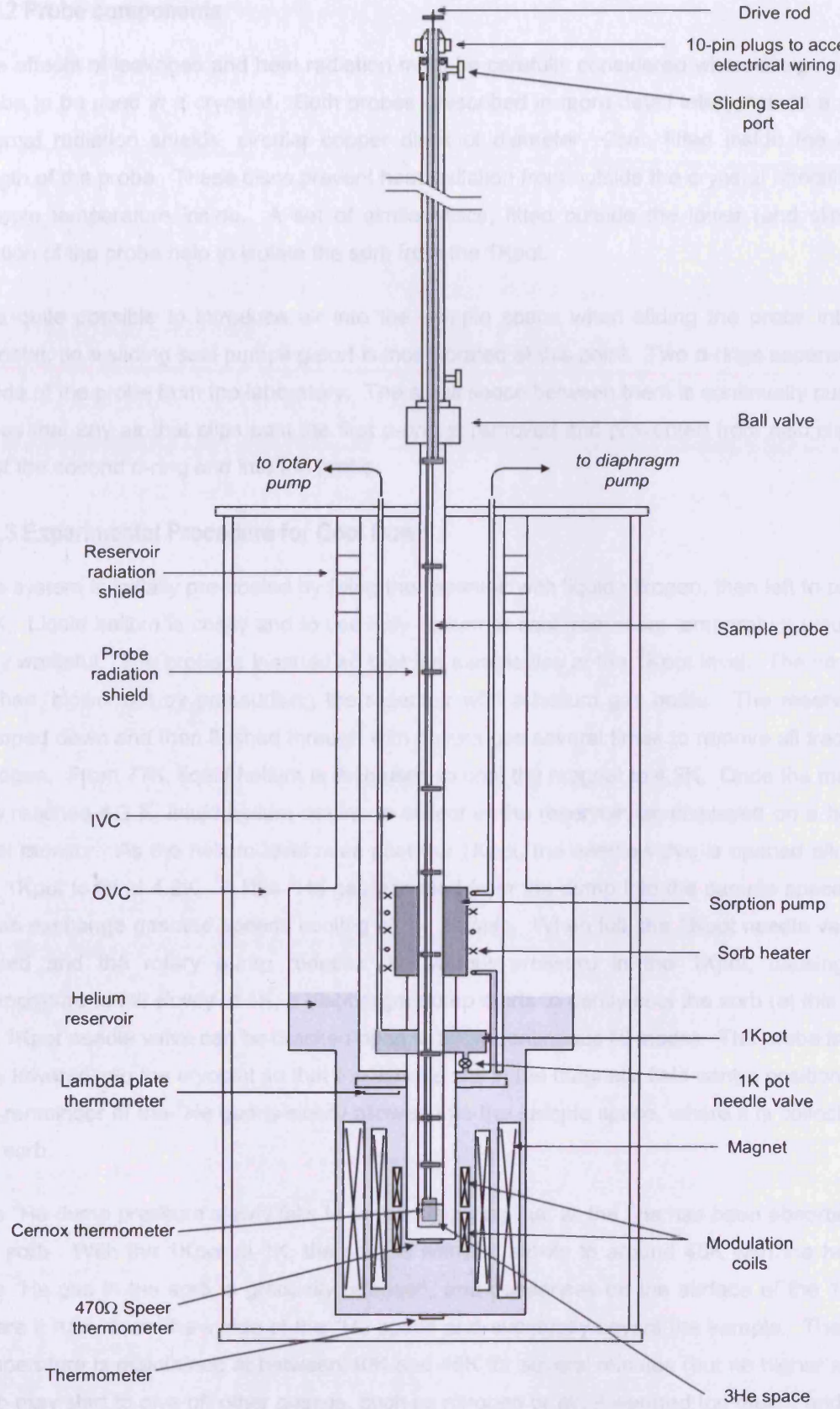

***Figure 4.1**: Simple schematic of the cryostat with top-loading probe fully inserted to measurement position*

4.1.2 Probe components

The effects of leakages and heat radiation must be carefully considered when designing any probe to be used in a cryostat. Both probes (described in more detail later) include a set of internal radiation shields, circular copper discs of diameter ~2cm, fitted inside the upper length of the probe. These discs prevent heat radiation from outside the cryostat affecting the sample temperature inside. A set of similar discs, fitted outside the lower (and slimmer) portion of the probe help to isolate the sorb from the 1Kpot.

It is quite possible to introduce air into the sample space when sliding the probe into the cryostat, so a sliding seal pumping port is incorporated at this point. Two o-rings separate the inside of the probe from the laboratory. The small space between them is continually pumped on so that any air that slips past the first o-ring is removed and prevented from also slipping past the second o-ring and into the probe.

4.1.3 Experimental Procedure for Cool Down

The system is initially pre-cooled by filling the reservoir with liquid nitrogen, then left to cool to 77K. Liquid helium is costly and to use only helium to cool from room temperature would be very wasteful. The probe is inserted so that the sample lies at the 1Kpot level. The nitrogen is then 'blown' out by pressurising the reservoir with a helium gas bottle. The reservoir is pumped down and then flushed through with helium gas several times to remove all traces of nitrogen. From 77K, liquid helium is then used to cool the magnet to 4.2K. Once the magnet has reached 4.2 K, liquid helium begins to collect in the reservoir, as displayed on a helium level monitor. As the helium level rises past the 1Kpot, the needle valve is opened allowing the 1Kpot to fill at 4.2K. A little ^{3}He gas admitted from the dump into the sample space acts as an exchange gas and speeds cooling of the sample. When full, the 1Kpot needle valve is closed and the rotary pump reduces the vapour pressure in the 1Kpot, causing the temperature to fall slowly to 1K; a diaphragm pump starts to gently cool the sorb (at this point the 1Kpot needle valve can be cracked open to allow continuous fill mode). The probe is then fully lowered into the cryostat so that the sample sits in the magnetic field centre position, and the remainder of the ^{3}He gas is slowly allowed into the sample space, where it is collected in the sorb.

The ^{3}He dump pressure slowly falls to 0mbar, implying that all the ^{3}He has been absorbed by the sorb. With the 1Kpot at 1K, the sorb is warmed slowly to around 45K with the heater. The ^{3}He gas in the sorb is gradually released, and condenses on the surface of the 1Kpot, where it runs down the inside of the ^{3}He space and eventually covers the sample. The sorb temperature is maintained at between 40K and 45K for several minutes (but no higher as the sorb may start to give off other gasses, such as nitrogen or air, if warmed too much) and then the heater is switched off and the sorb temperature falls to 4.2 K. The ^{3}He dump pressure rises slightly during out-gassing and then falls to 0mbar as all the ^{3}He gas condenses. The

sorb pump continues to pump on the ^{3}He vapour, so reducing the sample temperature to 0.3K.

The ^{3}He liquid remains at 0.3K for several hours, but will eventually be completely reabsorbed by the sorb. At this point the sorb needs to be heated back up to 40K and the condensing process started again. Overnight, the ^{4}He liquid in the reservoir usually completely boils off and requires refilling each day. The ^{3}He liquid boils off and is held in the sorb from where it must be out-gassed for cool down each day.

4.2 Torque Magnetometry

4.2.1 The Principle of Torque Magnetometry

As its name suggests a torque magnetometer measures the torque or the force exerted on a magnetic moment in a non-parallel magnetic field. The torque, $\underline{\tau}$, is related to the magnetic field, $\underline{B}$, and the magnetic moment, $\underline{m}$, through:

$$\underline{\tau} = \underline{m} \times \underline{B} = mB\sin\theta \tag{4.2}$$

where θ is the angle between $\underline{m}$ and $\underline{B}$. Most materials have a magnetic moment that lies either parallel to or antiparallel to the applied magnetic field; this implies that the induced torque on them would be equal to zero. However the 2DEG, has a magnetic moment which is independent of the applied magnetic field and always lies perpendicular to its plane.

A 2DEG sample is fitted to a rotor, suspended by two fibres, as illustrated in Figure 4.2:

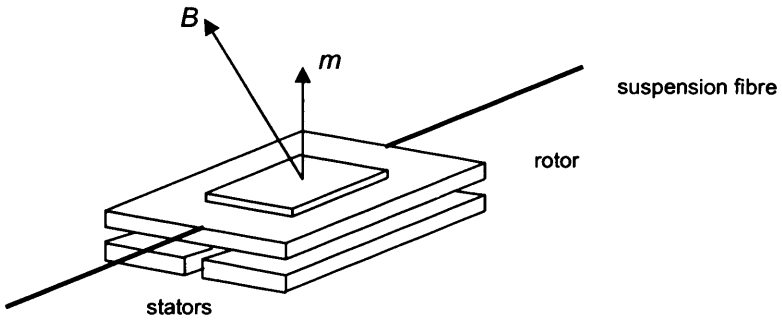

***Figure 4.2**: Diagram of sample attached to rotor, also showing positioning of stators, and direction of magnetic moment and field*

Beneath the rotor, separated by a tiny distance (< 1mm), are two stators, or fixed plates. When a torque is induced by the applied magnetic field, the sample and its rotor turn slightly until an equal and opposite torque in the suspension fibre balances the induced torque. The magnetic moment of the 2DEG can be found by measuring the angular deflection of the sample and rotor.

4.2.2 A Brief History of Torque Magnetometry

Eisenstein [1] designed and constructed the first torque magnetometer for use with 2DEGs. Figure 4.3 shows a schematic diagram of his system.

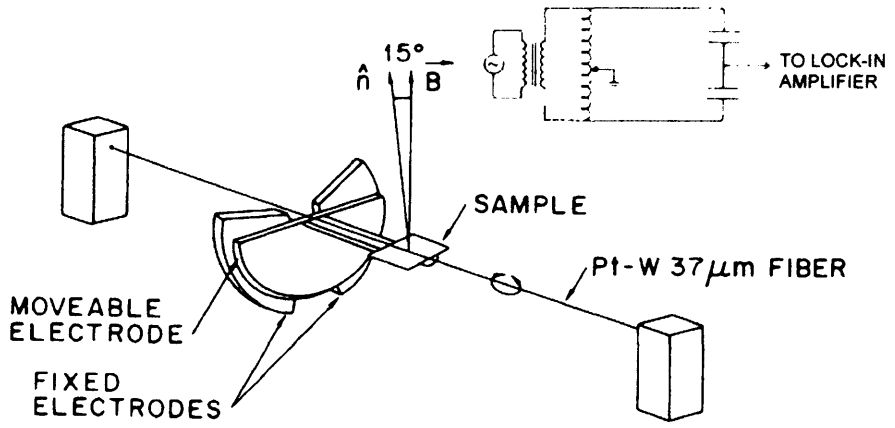

Figure 4.3: *Eisenstein's Torque Magnetometer [1]*

The rotor, a plastic disk, is mounted on, and perpendicular to, a fine suspension fibre held under tension by two supports. A thin layer of gold is evaporated to the back of the plastic rotor. The sample is mounted to the front of the rotor, but is oriented along the direction of the suspension fibre, and at an angle of approximately 15° to the applied magnetic field which is transverse in direction. A disk parallel to the rotor holds two electrodes, the stators, which remain fixed.

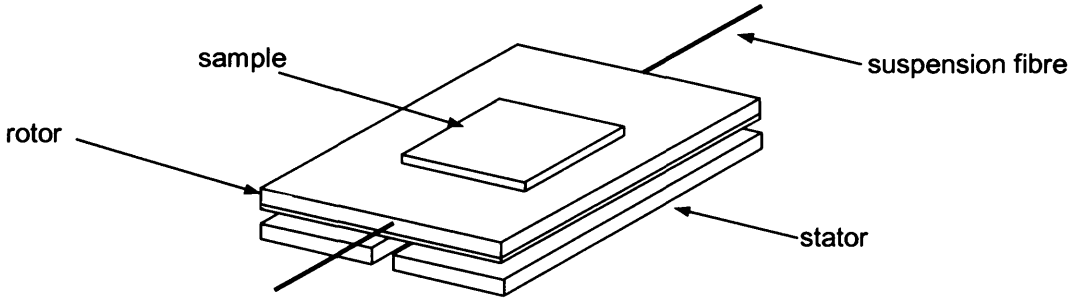

Figure 4.4: *Schematic diagram of Templeton's torque magnetometer [2].*

Later, Templeton [2] modified Eisenstein's design to one as shown in Figure 4.4 for a transverse magnetic field rather than parallel. Templeton positioned the rotor along the length of the suspension fibre, and mounted the sample directly to the rotor. Instead of plastic, he used a single crystal of sapphire for the rotor, with titanium and gold evaporated on its underside. The stators were made from printed circuit board. The suspension fibre was adapted so that it could be rotated by means of a spring mounting. This allowed the rotor to be balanced *in-situ*.

4.3 Instrumentation and Signal Detection

Two separate torque magnetometers were used to collect the quantum Hall effect data displayed in this thesis. The Mark IIIb probe already existed and had been developed and used by a previous student. The Mark IIIc, while utilising the same technique as the IIIb, has been recently developed in an attempt to improve upon the *in-situ* adjustment accessible through the use of these probes, and therefore to maximise the sensitivity. Both probes were used in conjunction with the 14T magnet system.

4.3.1 The Mark IIIb Probe

The 14T magnet system produces a vertical field, implying that the suspension fibre would lie horizontally, with the rotor tilted such that the angle θ, as described in Equation 4.1, could be formed, at around 20°. To accommodate this, the IIIb was designed with a wedge-shaped block on which the pair of stators is mounted, as shown in Figure 4.5 below.

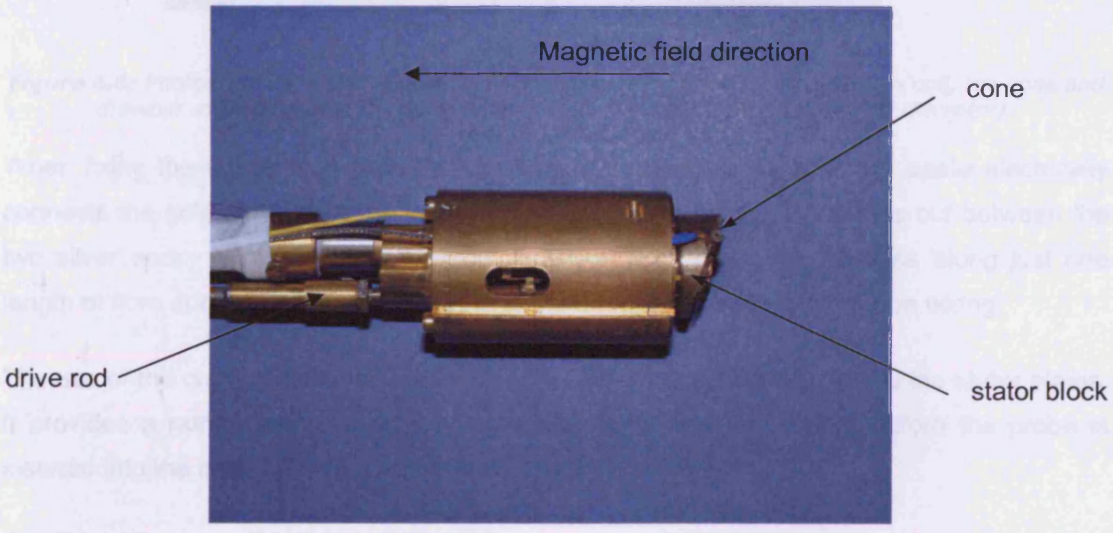

Figure 4.5: *Photograph of the Mark IIIb probe from the side, showing the wedge-shaped stator block, the fibre-mounting cone and the drive rod.*

The main body of the probe and the working metallic parts are machined from phosphor bronze, providing strength and good thermal conductivity, while remaining largely unaffected by any applied magnetic field. Two stator plates, each of area (9mm × 6mm) and also made of phosphor bronze, are mounted on the stator block so that they make an angle of 20° with the magnetic field. The rotor, a piece of 12mm × 12mm gallium arsenide with an evaporated gold layer on one side, is aligned parallel with the stators so that the gold side faces them. The 2DEG sample is fixed onto the rotor with a little vacuum grease. A phosphor bronze suspension fibre, of cross-section (17.25μm × 259.80μm) is attached to the rotor at two opposite edges with silver epoxy. The two free ends of suspension fibre each have a length of around 6mm. At one end of the fibre is soldered a tiny phosphor bronze drawbar, and this

locates in a sprung hook fibre support mounted alongside one stator. A small cone is soldered to the opposing end of the fibre and this locates in a mating cone mounted on a second fibre support alongside the other stator, as shown in Figure 4.6 below.

Figure 4.6: *Photograph of Mark IIIb, showing the GaAs rotor fitted with calibration coil, the cone and drawbar mountings and the fibre supports (stator plates concealed behind the rotor).*

When fixing the suspension fibre to the rotor, a small tail of silver epoxy paste electrically connects the gold surface on the rotor to the suspension fibre. The fibre is cut between the two silver epoxy joins so that the electrical signal from the rotor can pass along just one length of fibre and into the fibre support which is directly soldered to the probe wiring.

The use of the cone allows manual alignment of the rotor tilt with respect to the stator plates. It provides a rather coarse means of physically balancing the system before the probe is inserted into the cryostat.

For finer adjustment of rotor-stator balance, a system of gears is incorporated in the probe, and these are displayed schematically in Figure 4.7. Two gears (numbered (2) and (3) in the figure) attached to short rods which are in contact with the spring-mounted stator block, along the suspension fibre axis, sit inside the body of the probe. The short rods have screw threads along them so that as one gear is turned its rod moves up and down slightly inside the probe body. In so doing it presses gently on the stator block allowing the plate separation to be adjusted in this way. The two gears are controlled by a long, single drive rod which is controlled at the top of the probe. The drive rod has one matching gear near its end and can slide up and down within o-ring seals, so that it engages with only one (or neither) of the stator-adjustment gears at a time. At its very tip there is a screwdriver-like head which engages with a third screw-threaded rod. The end of this rod is positioned such that rotation of it causes the stator block to tilt about the axis of the fibre. The combination of the three gears allows the stator block to be brought very near to the rotor, while keeping the gap that separates them even across the rotor surface.

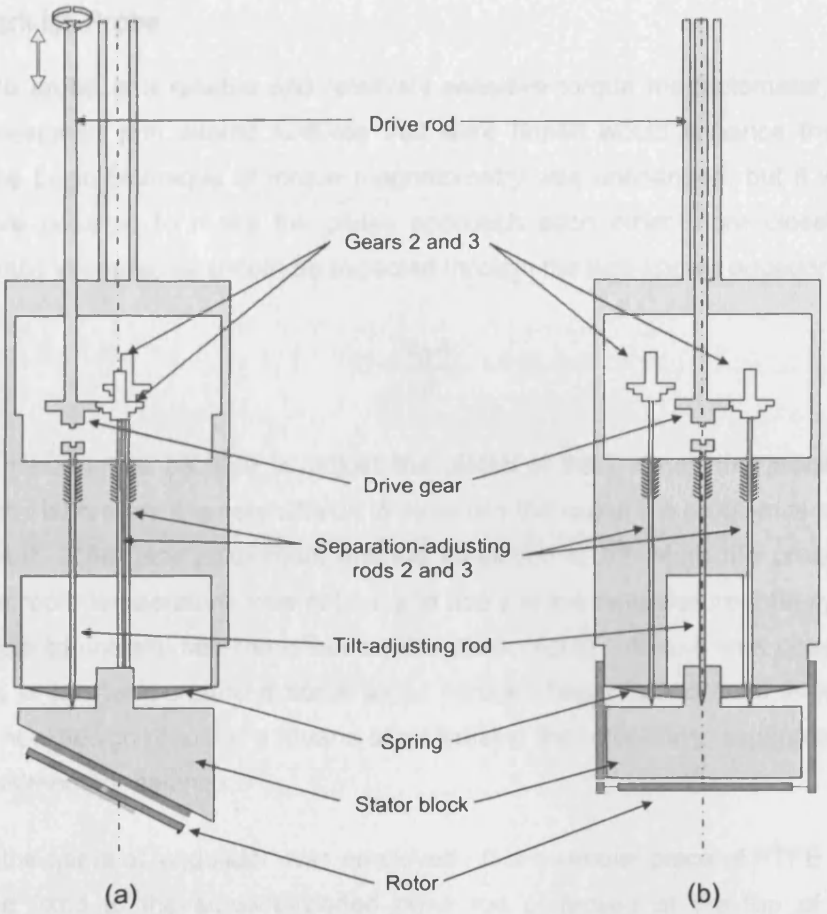

Figure 4.7: *Schematic cross-section of the Mark IIIb showing stator block adjustment available with drive rod. There is a 90° rotation between (a) and (b).*

The stator block and rotor parts are covered during experiment with a machined Perspex cap that is screwed onto the probe body securely. Inserted into a drilled hole in this cap, a calibrated Cernox thermometer measures the sample temperature. An LED is also housed within the cap.

4.3.2 The Mark IIIc Probe

The Mark IIIb probe is a reliable and relatively sensitive torque magnetometer, but a new probe was designed with altered features that were hoped would enhance the sensitivity attained. The basic technique of torque magnetometry was unchanged, but it was thought that if it were possible to make the plates approach each other more closely then the sensitivity would increase, as should be expected through the well-known equation

$$C = \frac{\varepsilon_0 A}{d}. \tag{4.3}$$

It was also important to be able to adjust the plates *in situ*. Once the probe has been balanced in the laboratory it is very difficult to ascertain the cause if a problem is encountered mid-experiment. The gear adjustment method employed in the Mark IIIb probe, although responsive at room temperature, was not easy to apply at low temperature, mainly because it was impossible to actually see the effect on the stator plates. Also, it was possible for the gears to jam at low temperature if some air or nitrogen happened to have leaked into the probe. The new design required a means of minimising the rotor-stator separation while still allowing adjustment for balance.

A tool given the name of 'undulator' was employed. It is a circular piece of PTFE of diameter 19.5mm, and fixed to the screw-threaded drive rod controlled at the top of the probe. Extending from the centre to its perimeter are machined small straight grooves (troughs) of width ~2mm, creating an undulating surface, as shown in Figure 4.8.

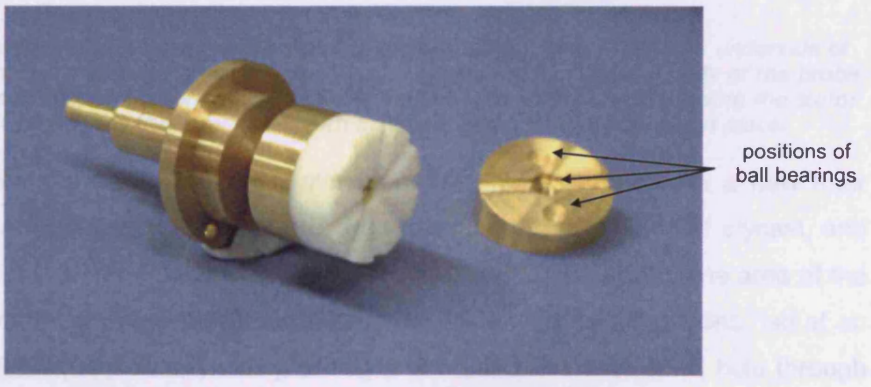

Figure 4.8: *The 'undulator' (white ertalyte) is fixed to a screw-threaded rod, which allows the undulator to traverse up and down as the rod is rotated.*

The stator block is again spring-mounted on a strip of phosphor bronze, and on the upper side of the block are drilled two indentations, displayed also in Figure 4.8. These indentations, together with one drilled in the spring-fixing screw in the centre, house three sapphire ball bearings in a row. As the undulator rotates and approaches the ball bearings, the outer two are forced against the altering surface of the undulator as it contacts them. The troughs are machined in such a way that for a trough on one side of the undulator, there is a

peak on the exactly opposing side. When a ball bearing moves out of a trough and onto a peak it pushes down on its side of the stator block, which is free to tilt under this force about the spring upon which it is mounted. The opposite ball bearing will, simultaneously, move from a peak into a trough. In this way the stator block will tilt back and forth over the central position while narrowing the rotor-stator separation.

A piece of commercially fabricated circuit board houses the stator plates (each of area (11mm × 5mm) and this is screwed to the underside of the stator block, see Figure 4.9(c). A separate ertalyte rotor base (see Figure 4.9(d)) holds the two phosphor bronze supports on which the rotor and its fibre are mounted. The rotor base is inserted up inside the main body until its ridge contacts the probe body and is screwed securely to it.

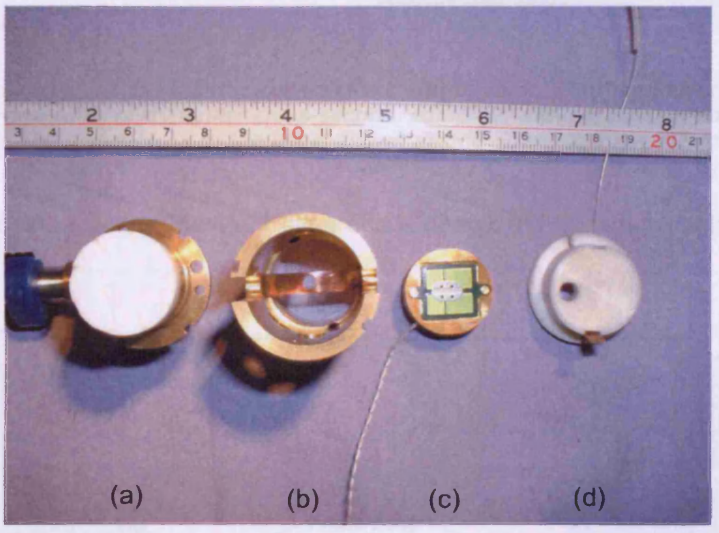

Figure 4.9: *Photograph showing the separate parts of the probe from above: (a). the underside of the undulator joined to the probe cap by its screw-thread; (b). the main cylindrical body of the probe showing the stator block supporting spring; (c). the underside of the stator block, showing the stator plates on circuit board; (d) the rotor base, with LED hole and one fibre support in place.*

Rather than incorporate a wedge-shaped stator block, the Mark IIIc includes a new rotor design, with triangular cross-section. The rotor was machined from a piece of stycast, and has a maximal area of (12mm × 12mm) on its square side, sufficient to match the area of the stators; a layer of gold was evaporated onto this square side. The sloping sides rise at an angle of 30° to the flat square side, yielding a height of around 2mm. A small hole through which to feed the suspension fibre was drilled between the two triangular cross-sections, and its position on this cross-section was calculated to lie at the point of the centre of mass.

This geometry provides a flat, rectangular surface with which to complete the capacitance plate pairs, but allows the 2DEG sample to be positioned on the other sloping side of the rotor at the required angle of 30° to the field. A photograph of a mounted rotor is shown in Figure 4.10. Fitting the sample to one half obviously causes the rotor to tilt so a balancing piece of gallium arsenide is fitted to the other sloping side. This balancing piece is of similar material to the 2DEG sample, but without the 2DEG. As the rotor base is a separate part, it is possible

to roughly balance the rotor by eye before inserting it into the probe where it can be more finely adjusted. The combination of drawbar and cone was used at either end of the suspension fibre, to mount the rotor to the rotor base, as used for the Mark IIIb probe.

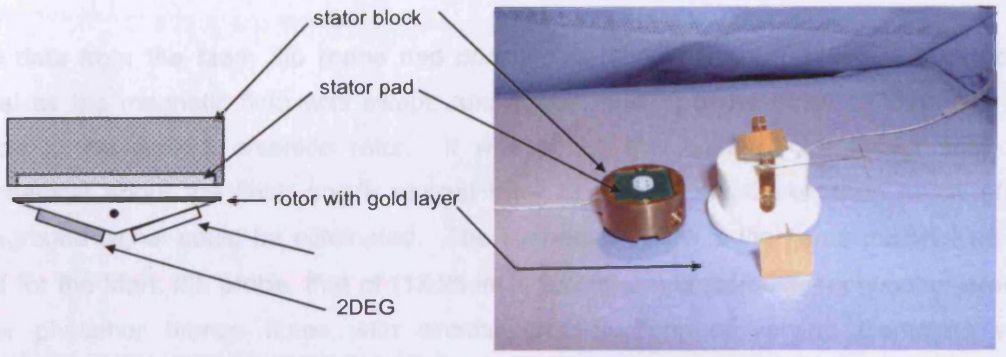

Figure 4.10: *(a) Diagram showing the set-up of the stator, rotor, 2DEG and balancer; (b) Photograph showing the stycast rotor of triangular cross-section, complete with suspension fibre, and mounted on the rotor base. The stator block to the left is shown upside-down, to allow viewing of the stator pad itself.*

A simplified cross-section of the Mark IIIc probe is shown in Figure 4.11 below.

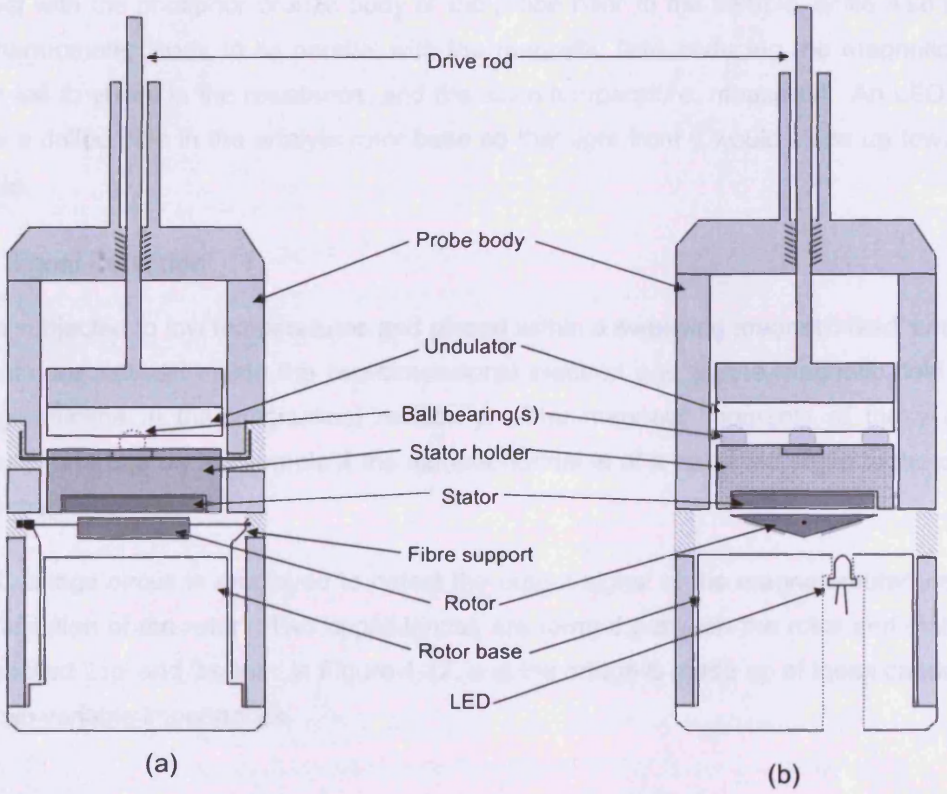

Figure 4.11: *Schematic cross-section of the Mark IIIc showing stator block adjustment available undulator. There is a 90° rotation between (a) and (b).*

Note also, in Figure 4.10, the reduced width of the stator pad with respect to the rotor. By recessing the stator pad into a block of phosphor bronze it is possible to reduce any capacitive coupling between the sample and the stator plates. This effect was also hoped to be minimised by replacing the gallium arsenide rotor with stycast.

Raw data from the Mark IIIb probe had consistently shown a normally-linear background signal as the magnetic field was swept, and it was thought to be down to magnetic field effects in the gallium arsenide rotor. It was hoped that with a rotor design that was symmetrical about the field, and a stycast rotor to replace the GaAs, then much of the background signal could be eliminated. The suspension fibre is the same material as that used for the Mark IIIb probe, that of (17.25μm × 259.80μm) cross-section phosphor bronze. Other phosphor bronze fibres with circular cross-sections of varying diameters were experimented with, but the rotor was found to oscillate more freely when the fibre had been rolled flat, i.e. with a rectangular cross-section, so this was applied again.

To measure sample temperature, the afore-mentioned calibrated Cernox thermometer is inserted into a hole along the probe body wall. Two such holes can just be detected in Figure 4.9(b) within the probe body. Placement of the thermometer in this way enables good thermal contact with the phosphor bronze body of the probe near to the sample, while also allowing the thermometer leads to lie parallel with the magnetic field, reducing the magnetic effects which led to errors in the resistance, and therefore temperature, measured. An LED is fitted inside a drilled hole in the ertalyte rotor base so that light from it would shine up towards the sample.

4.3.3 Signal Detection

When subjected to low temperatures and placed within a sweeping magnetic field, small eddy currents are induced inside the two-dimensional electron gas as the magnetic field passes through minima in the longitudinal resistivity. The magnetic moments of these currents generate a torque on the sample if the sample normal is at a non-zero angle to the direction of the magnetic field.

An AC bridge circuit is employed to detect the output signal of the magnetometer yielded by the deflection of the rotor. Two capacitances are formed between the rotor and stators and are labelled 'top' and 'bottom' in Figure 4.12, and the bridge is made up of these capacitances plus two variable impedances.

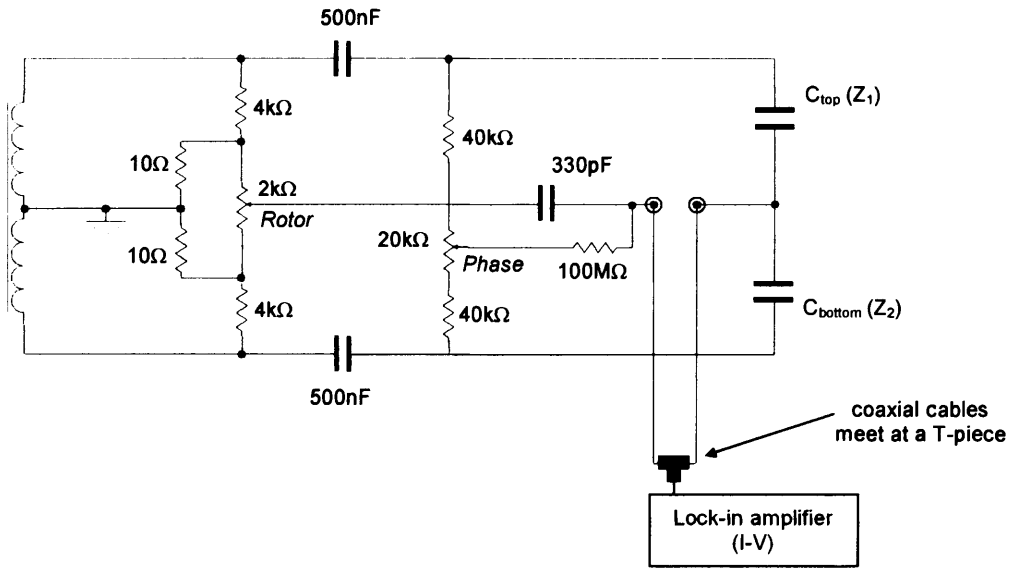

Figure 4.12: *Circuit diagram of simple bridge circuit.*

An AC voltage source provides an AC signal to the top and bottom of the parallel capacitances; these are in antiphase. Ideally, when the system is perfectly balanced (when there is an equal gap between both pairs of capacitors), there will be no output voltage signal. When the rotor is initially set up it is mechanically adjusted to lie as perfectly symmetrical with respect to the stators as possible (typical values of these capacitances were of the order 1pF). By incorporating additional potentiometers (marked *rotor* and *phase*) in the above circuit it is possible to electronically balance the circuit more accurately. As the magnetic field is swept, and the eddy currents induce a magnetic moment, the rotor deflects slightly. This alters the ratio of the capacitances and a lock-in amplifier detects the change in voltage at the measurement point labelled above. The lock-in amplifier combines this change in signal with a reference signal also provided by the AC voltage source.

When data is collected during a magnetic field sweep the computer logging program collects signal voltages from both channels of the lock-in amplifier. A data file then contains values for each channel with respect to field. An example of such data is displayed below in Figure 4.13.

To analyse the data more easily it is necessary to combine the two channels into a single signal that varies with field. Consider Figure 4.13 (c), where the signal is shown as an arrow on a real-imaginary plot. This is a simple schematic of what is experimentally measured, where the two axes are the two lock-in channels, and the arrow displays the magnitude of the channels. As the field sweeps over a peak, the length of the arrow will increase; then as the peak is passed over, the arrow shrinks. The phase angle does not change over the field sweep, and the arrow points in the same direction throughout. Figure 4.13(d) shows the same plot, but with rotated axes superimposed as dotted lines.

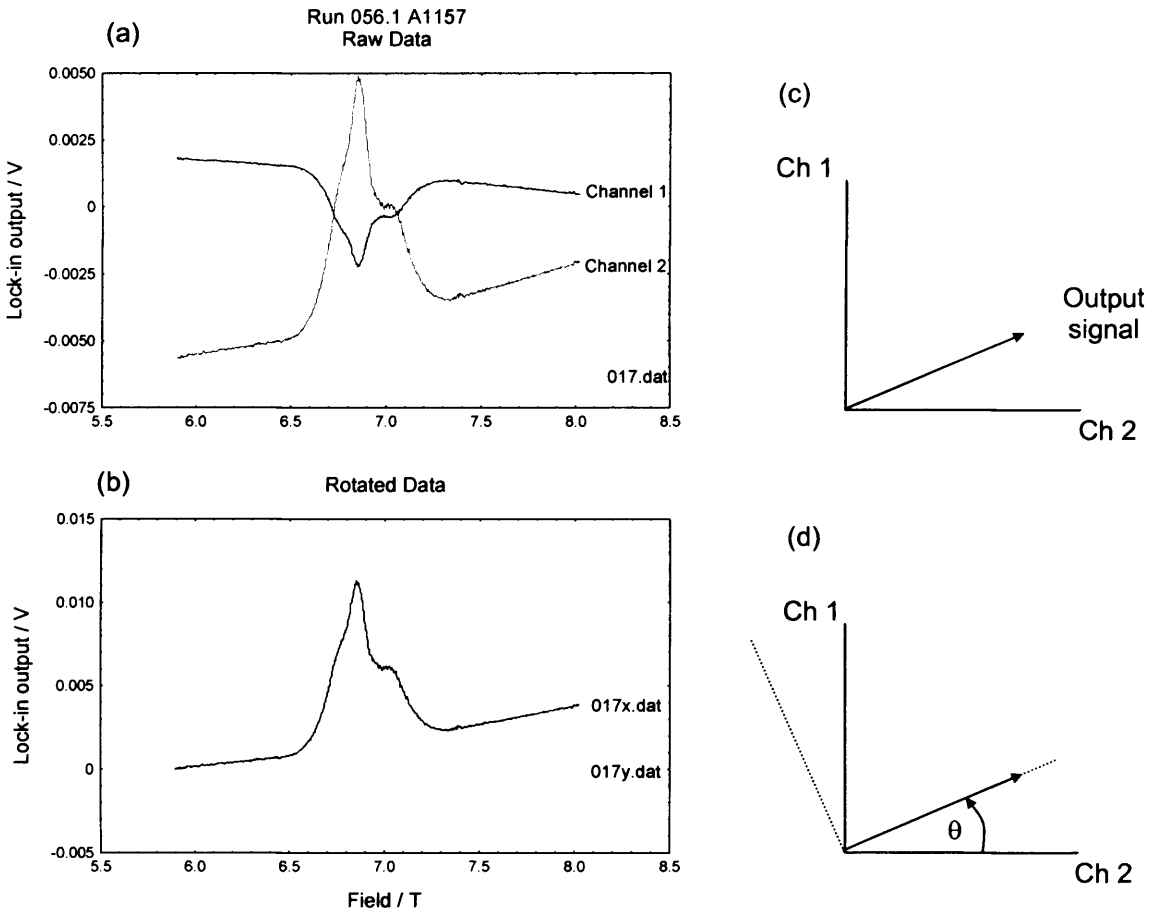

Figure 4.13: *Raw Data of the Mark IIIb magnetometer for sample T231, showing two lock-in channels that have a phase difference of 90°; (a) the original two lock-in channel signals, (b) the channels rotated such that one carries the majority of the signal while the other carries a mainly zero signal, (c) and (d) demonstrate schematically how the channels have been rotated.*

If the correct value for the rotation angle θ is found, it is possible to transform the data set for each channel so that the entire signal is directed through one channel. The other channel will exhibit a signal of zero. To accomplish this, the data file, say 017.dat, is passed through a rotation program where the user must input an estimate for θ. The result is two additional data files, 017x.dat and 017y.dat, one of which contains the signal magnitude with respect to magnetic field and the other contains zero signal with respect to magnetic field. Figure 4.13(b) shows the result for the example of data file 017.dat in Run 056.1; file 017x.dat contains the signal, and 017y.dat holds the zeros. From this point file 017x.dat would be used in analysis.

Provided there were no additional capacitive pick-up effects observed on the magnetometer, it was possible to simply adjust the lock-in amplifier phase setting as a time-saving technique that much reduced the analysis. If additional capacitive structure was observed in the magnetometer signal (as for one particular sample) then it was necessary to remove this first, for which the procedure involved is explained in section 5.1.

4.3.4 Signal Calibration Techniques and Sensitivity Measurement

When observing the quantum Hall effect in the manner described above, the output signal of the sample is in the form of a lock-in voltage. In each experiment the rotor and stators will be set up slightly differently, depending on sample size, plate separation and spring coefficient of the suspension fibre, and these will govern the value of the probe's sensitivity. It is therefore necessary to calibrate the instrument so that the output signal can be converted into a magnetic moment, the preferred result of the torque magnetometry technique. A *calibration constant, c,* provides a factor by which the raw output data can be multiplied to convert from lock-in voltage to magnetic moment, since it is known that

$$\tau = cV \tag{4.4}$$

where τ is the torque, in Nm, and V is the lock-in output signal, in volts. The calculation of such a constant provides a real numerical value of the sensitivity of the instrument. This is a particularly useful value in that it provides information about how responsive the instrument was in each experimental run; it also allows a direct comparison between the two probes. Further, converting a magnetic moment value into a torque through

$$\underline{\tau} = \underline{m} \times \underline{B} = mB\sin(\theta)\hat{\underline{n}}, \tag{4.5}$$

where $\hat{\underline{n}}$ is a unit vector parallel to the torque, takes account of the point in field in which the calibration was performed. This is important when the method of calibration involves properties that vary with magnetic field. By transferring all raw data into torque using multiplying factors specific to the run in which the data was acquired, all data may be directly compared, irrespective of the sensitivity of probe at that time, or which probe was indeed used.

Two differing methods of calibration were employed to calculate the calibration constant.

The Coil Method

The coil method has until recently been the favoured method, due to its accuracy, simplicity and ease of use.

It is known that the torque, $\underline{\tau}$, is expressed as a function of magnetic moment $\underline{m}$, and magnetic field $\underline{B}$, as

$$|\tau| = |\underline{m} \times \underline{B}| = mB\sin(\theta)$$

where θ is the angle between m and B. The magnetic moment m can be rewritten as

$$m = IA$$

where *I* is the current and *A* is the cross-sectional area. By passing a known current through a circular coil of known cross-sectional area, within an applied magnetic field, it is possible to add a small amount of known torque.

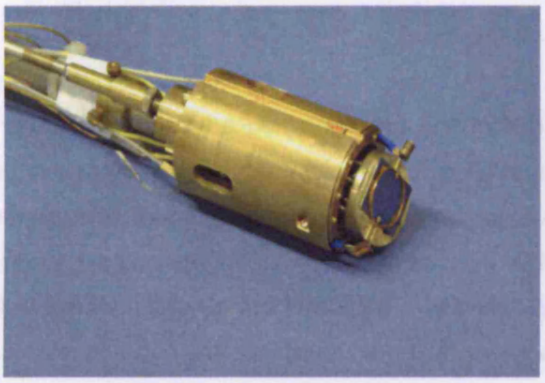

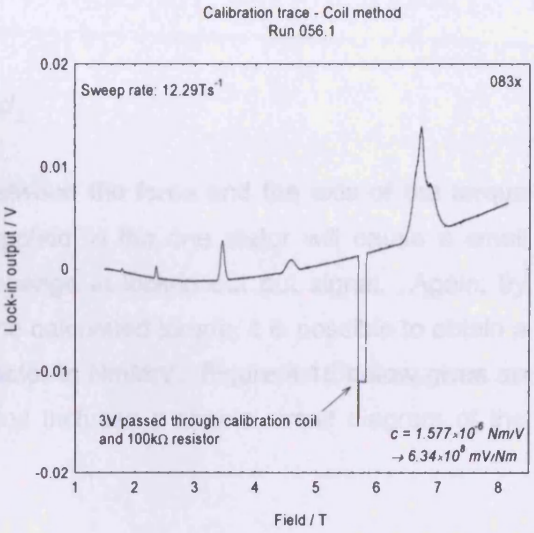

(a) (b)

Figure 4.14: *(a) The copper wire coil of 3 turns can be seen on the GaAs rotor on the Mark IIIb probe; (b) A typical calibration measurement. A current is passed through the calibration coil between two eddy current peaks; by calculating the induced torque it is possible to compute a calibration constant in Nm/V with which to convert the lock-in output voltage signal into torque.*

The photograph above in Figure 4.14 shows the Mark IIIb probe with a calibration coil fitted to its rotor. In practice, during an experimental run, the calibration constant is calculated daily to verify correct working function. As the field is swept upwards, a power supply delivers a known current to the coil for a short time, at a point in field either away from the peaks or between them. The rotor tilts a small amount under the influence of this extra torque, and the change in signal is recorded by the lock-in amplifier. Simply dividing the lock-in output voltage (in mV) by the calculated torque (in Nm) produces a value for sensitivity (in mV/Nm). Conversely, inverting this value gives the multiplying factor required to translate lock-in output voltage into torque.

The DC-Offset Method

The dc-offset method was derived in the development of Mark IIIc when the coil method was found to be unsuitable. It involves applying a known voltage to one of the stators, so inducing a force between the stator and rotor that causes a small change in their separation. It is known that the energy, *U*, of a capacitor is given by

$$U = \frac{1}{2}CV^2$$

The force, *F*, between the plates of a capacitor, is simply the differential of the energy with respect to the plate separation

$$F = \frac{dU}{dz} = \frac{1}{2}V^2 \frac{dC}{dz} = -\frac{1}{2}V^2 \frac{C^2}{\varepsilon_0 A} \tag{4.6}$$

By calculating the force between the plates, it is possible to know the torque of the suspension fibre through

$$\tau = F \cdot d_{\perp}$$

where $d_{\perp}$ denotes the perpendicular distance between the force and the axis of the torque (i.e. a quarter of the rotor width). The force applied to the one stator will cause a small deflection of the rotor which is recorded as a change in lock-in out put signal. Again, by dividing this change in lock-in output voltage by the calculated torque, it is possible to obtain a value for sensitivity in mV/Nm, or a multiplying factor in Nm/mV. Figure 4.15 below gives an example of a typical calibration measurement and includes a simple circuit diagram of the calibration connections.

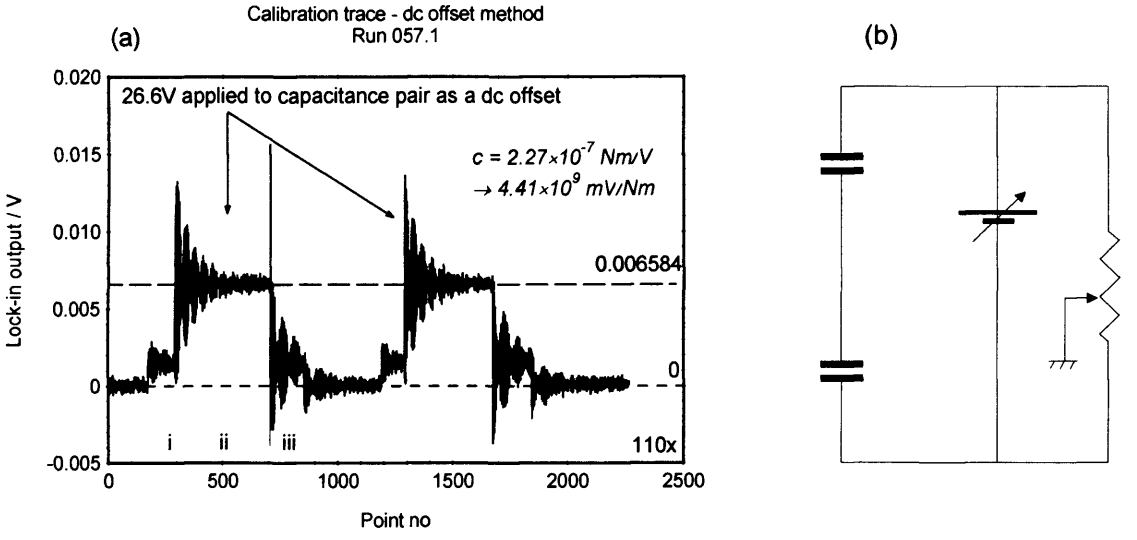

Figure 4.15: *Calibration trace for the Mark IIIc probe employing the dc offset calibration method at T=0.3K. A known voltage (26.6V) is applied to the capacitance plates producing a force that deflects the rotor as seen in the rise in signal. Dividing the calculated torque by the change in lock-in voltage output produces the calibration constant in Nm/V. A ringing in the signal is observed as the rotor oscillates after the initial deflection.*

The signal shape observed when the voltage offset is applied and when it is removed is different. This is due to the two-part process of the voltage application. First, a net potential difference of 26.6V is applied across the two stator leads. An equal force should be set up between each rotor-stator pair, but since the rotor will not be perfectly symmetrical at first there will be a slightly larger force between the pair which are closer to each other; this causes the first shift visible in Figure 4.15a(i). A variable resistor, in the form of a switch, then directs the potential difference so that the full 26.6V is applied either to one rotor-stator pair or the other, resulting in the large signal shift of Figure 4.15a(ii). The force between the rotor

and stator can then be calculated using equation 4.6 using V=26.6V. The variable resistor is then switched so that the potential difference is applied equally between the two rotor-stator pairs and the signal returns to the value of Figure 4.15a(i), as shown at point (iii).

Comparison of IIIb and IIIc

While developing the new Mark IIIc probe it was important to have a reliable method of judging its performance with respect to the existing Mark IIIb. The calibration constant proved very useful in this task as the two probes could be directly compared.

The results of room temperature calibration tests are shown in the table below.

	Mark IIIb		Mark IIIc	
	Calibration constant	Resonant frequency	Calibration constant	Resonant frequency
Coil method	8.4×10^{8} mV/Nm	22Hz	2.4×10^{8} mV/Nm	27Hz
DC-Offset method	9.3×10^{8}mV/Nm	-	1.33×10^{10}mV/Nm	5Hz

Table 4.1: *Comparison of probe sensitivities at room temperature. The two probes were calibrated through two different method with the resulting data displayed above.*

Coil measurements on each probe were attained by passing a known current through the calibration coil while the rotor was positioned within a horseshoe magnet of a field of ⅓T. Although the calibration value for the Mark IIIc was of an order comparable with the existing (Mark IIIb) probe, the sensitivity was clearly worse and not improved as had been hoped. The resonant frequency of each of the probes was also measured on a storage oscilloscope by perturbing the system (through light tapping on the bench) and recording the signal as it died away exponentially: the results are shown in the above table also. The resonant frequency of the Mark IIIc before the coil was mounted was also measured; a value for frequency in the absence of a coil was not determined for the Mark IIIb as it was deemed unwise to remove a perfectly useful coil from a working probe purely for this purpose. It was also easy to observe with the naked eye the 'ringing' of the coil-less rotor as it settled after the perturbation – this could not discerned for a rotor with a coil.

As the IIIc probe developed it became apparent that adding a coil greatly reduced the sensitivity of the instrument. While the coil itself did not cause a great deal of imbalance from its asymmetry, it was the pair of leads to it that added such restoring force to the suspension fibre that the response was so diminished. Figure 4.16 shows several variations of the placement of the leads in an attempt to minimise the damping effect.

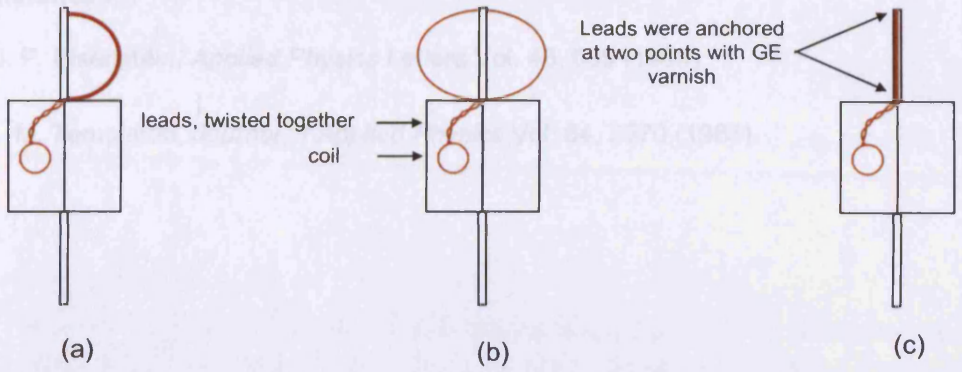

Figure 4.16: *View from above of the triangular-shaped rotor of probe IIIc, fitted with a calibration coil on one of its tilted sides. The leads are arranged in three differing ways: (a). both leads bow out to one side; (b) a lead bowing out to each side; (c) both leads, anchored at the rotor edge, protrude straight out and are anchored again at the fibre mounting spring.*

It was expected that arranging the coil leads so that they bowed out between the two anchoring points would have the least effect on the restoring force of the fibre as there would be less tension between the anchors. However this was not found to be the case. Counter-intuitively, the best result was obtained when the leads were arranged to lie in a straight line between the anchoring points, and more 'ringing' could be observed when disturbing the system. In spite of this, the sensitivity was still not ideal.

This led to the application of the dc-offset calibration method described above, so eliminating the need of a calibration coil. Room temperature calibration measurements on Mark IIIc gave a sensitivity almost 16 times better than that found with a coil for the Mark IIIb. Since it was uncomplicated to employ this method on the Mark IIIb also, the same measurement was performed as a check. The sensitivity for the Mark IIIb using the dc-offset method was found to be in agreement with that found with a coil as described above, and therefore judged as a reliable method of calibration in the new Mark IIIc probe.

4.4 References

[1]. J. P. Eisenstein, *Applied Physics Letters* Vol. 46, 695 (1985).

[2]. I. M. Templeton, *Journal of Applied Physics* Vol. 64, 3570 (1988).

Chapter 5: Quantum Hall Effect Measurements

Upon application of a sweeping magnetic field eddy currents are induced in any conductor. The integer quantum Hall effect (IQHE) is observed in a two dimensional electron gas (2DEG) when both the diagonal conductivity and the diagonal resistivity vanish at zero temperature, and the Hall conductivity is exactly quantised into integer multiples of e^2/h. The eddy currents produce a magnetic moment perpendicular to the plane of the sample as shown in Figure 5.1. This magnetic moment provides a means of examining the sample without making physical electrical contacts, which can perturb the system. High sensitivity torque magnetometry is an ideal testing technique in this respect.

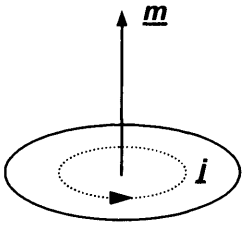

Figure 5.1: *A circular sample with circulating eddy currents, j, producing a magnetic moment, m.*

Three AlGaAs/GaAs heterojunction samples, denoted by the labels T231, A1157 and NU2055, were examined for this work, during three separate cool downs. In the following three sections, relatively detailed reports are presented to provide an introduction for each sample and its behaviour; specific effects and measurements will be described and presented in later chapters where results for the three samples will be collated.

5.1 Sample T231

T231 was grown at the Cavendish Laboratory, Cambridge. A layer profile is given in Table 5.1 and an example of raw experimental data taken is displayed in Figure 5.2. Classical Hall effect measurements taken after growth gave a number density of $1.25\times10^{15}m^{-2}$.

Layer description	Material	Dopant (cm^{-3})	Thickness (nm)	Notes
Cap	GaAs		17	
Active	AlGaAs	Si 1×10^{17}	200	
Spacer	AlGaAs		50	
Spacer	GaAs		2000	2DEG residing at upper edge
Superlattice buffer	AlGaAs		200	
Pre-buffer	GaAs		10	
Substrate				

Table 5.1: *Structure of T231 wafer.*

Sample T231, of size (12mm × 12mm) was tested during Run 055.1 using magnetometer Mark IIIb; measurements were taken at temperatures of 0.3K, 0.65K, 0.9K and 1.1K, and at total sweep rates of 0.45, 0.92, 1.64, 5.98, 12.29 and $25.18mTs^{-1}$ over a magnetic field range of (0 – 12)T. Two traces are plotted in each graph of Figure 5.2, the upper trace showing

data for upward-sweeping field, and the lower for downward-sweeping field. A calibration constant was found to be 3.11×10^{-6} Nm/V for this particular run (or if quoted as a sensitivity, 3.22×10^{8} mV/Nm). It can be seen that the peak direction reverses, due to the reverse direction of the induced eddy currents. A curving background is also visible between the integer filling factor peaks, and is thought to be due to magnetic effects within the gallium arsenide rotor of the Mark IIIb probe.

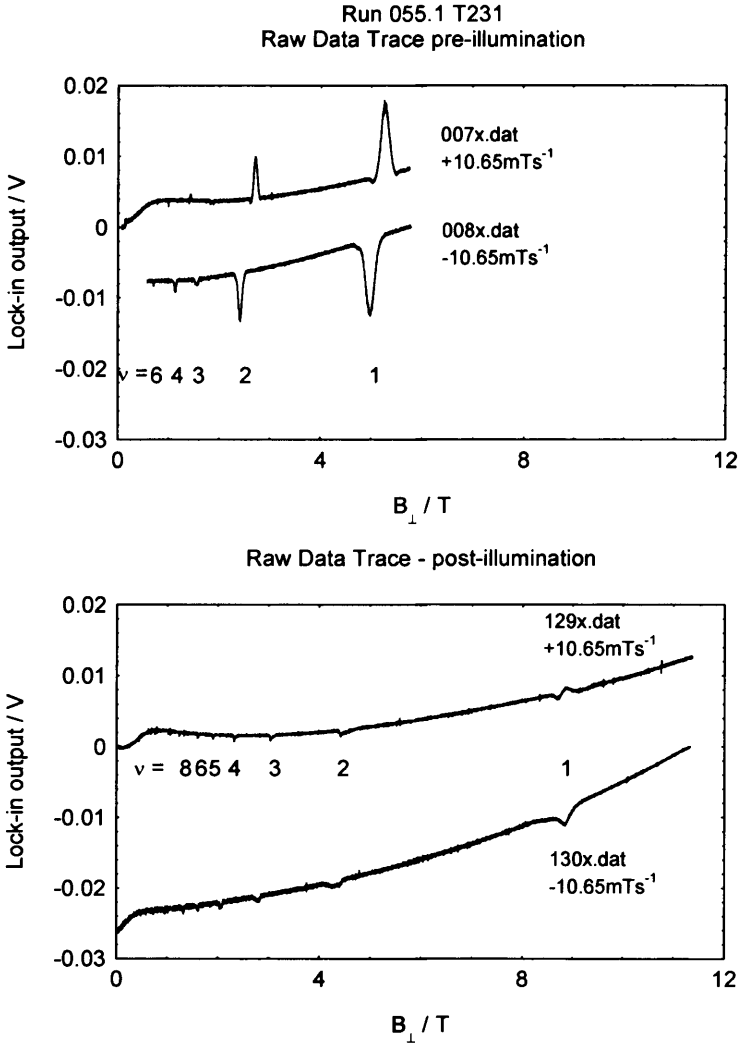

Figure 5.2: *Raw data from the torque magnetometer for sample T231. The lock-in output signal (in volts) is plotted against $B_\perp$, the component of magnetic field which lies perpendicular to the normal of the sample. The sweep rate has also been converted to its perpendicular component through multiplication of cos(ϕ) where ϕ=20° in this case. The eddy current peaks are labelled with their corresponding filling factor, ν.*

The peaks themselves are shifted in field, depending upon the sweep rate direction; sweeping up shifts the peaks up in field while sweeping down shifts them down in field, and a greater shift is observed at higher sweep rate. This is unexpected and not usually seen in published literature; the most likely cause is an effect of the switch heater of the superconducting magnet. The 14T magnet used to generate the magnetic field has an inductance of 20H, and the resistance of the switch heater is expected to be several ohms. This would give a time constant $\tau = L/R \approx 10s$. The time elapsed between the up and down sweep peaks is

calculated to be around 20s; this value is halved to give the amount of time elapsed from the real peak position (assumed to be in the middle of the shifted peaks) to 10s, which explains the occurrence of such a shift.

In order to be able to illuminate the sample it was necessary to raise the probe by about 3 feet to warm the LED sufficiently (to around 16K) such that a current could be passed; the sample was then illuminated by the LED for approximately 1 minute. The lower graph of Figure 5.2 shows the effects of illumination on the peak height and position in field.

In an experiment, having performed a preliminary sweep over the whole magnetic field range (0 – 12T), a series of reproducible peaks are observed at particular values of magnetic field as shown in Figure 5.2. It is known (from Equation 3.24) that the Landau filling factor is given by

$$\nu = \frac{n_s h}{eB}, \tag{5.1}$$

so, having found the peak positions in field, it is possible to plot ν against 1/B. If the values of ν are correctly estimated initially, a straight line can be fitted, allowing the number density to be calculated from its gradient. Figure 5.3 below shows two filling factor profiles for T231, both before and after illumination, with filling factor plotted against inverse field. The gradient of this straight line is given by $n_s h/e$. The number densities for T231 calculated from these slope values are displayed in Table 5.2 below and it can be seen that n_s is almost doubled after illumination.

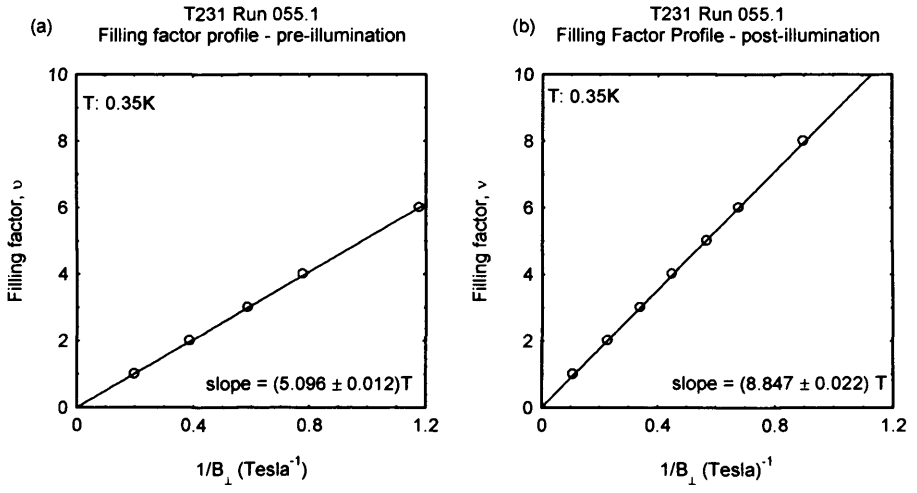

***Figure 5.3**: Calculation of number density ns: Estimated filling factor ν versus the inverted observed peak position in field, 1/B. (a) Pre-illumination; (b) Post-illumination.*

	gradient / T	n_s / m^{-2}
Pre-illumination	(5.096 ± 0.012)	(1.232 ± 0.003)×10^{15}
Post-illumination	(8.847 ± 0.022)	(2.139 ± 0.005)×10^{15}

Table 5.2: *Comparison of electron number density for T231 before and after illumination.*

It can be seen in Figure 5.2 that the eddy current peaks appear to have slight undulations in signal on the low field side. This effect was only seen in sample T231, and is thought to be due to capacitive coupling, described below.

Capacitive Coupling

Section 4.3.3 described how the two lock-in amplifier channels are transformed to produce a single signal. This procedure was performed on data acquired for sample T231, but it was found that no phase angle would completely eliminate one channel.

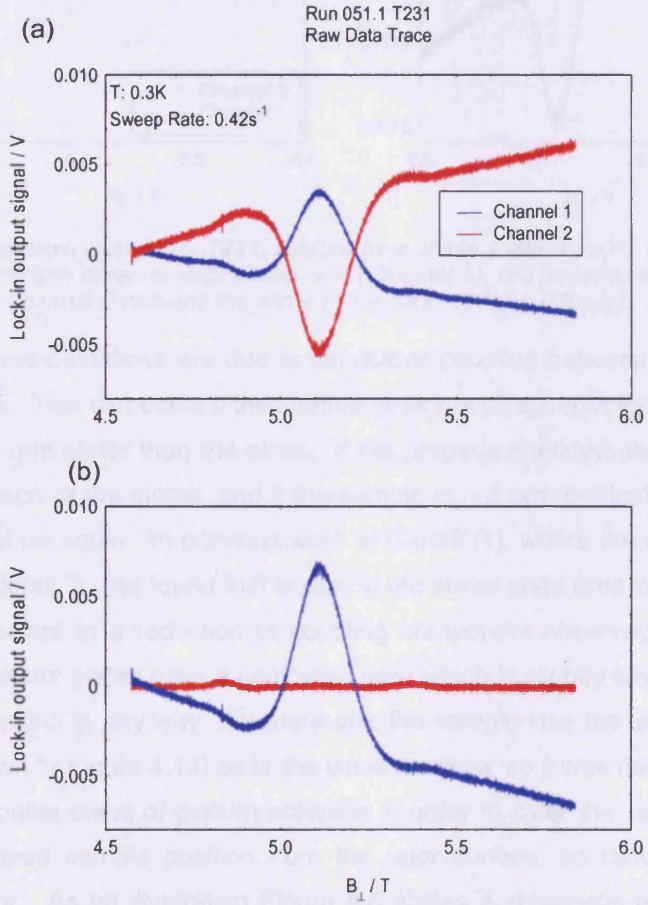

Figure 5.4: *Data for T231 at ν=1: (a) The original data file with both channels included; (b) The separate, transformed data files acquired after altering the phase angle (in this case, θ=60°). Magnetic field values ($B_\perp$) are given for the component perpendicular to the sample plane, i.e. parallel to the sample normal [Data files: 017.dat, 017x/y.dat].*

Figure 5.4 shows the raw data (top graph) and the altered data after transformation (bottom). The red trace in the lower graph, for 017y.dat, is not obviously zero over the whole field range

as expected, but displays small departures at the sides of the eddy current peak. Many values for θ were applied, but no single value would completely eliminate these fluctuations. This was also true for the down sweep, as shown in Figure 5.5 below. Reversing the sweep rate causes a reversal of the induced current direction and therefore a reversal of the peak direction, but the odd fluctuations on the 'zero' channel are observed to be independent of sweep direction and always point in the same direction.

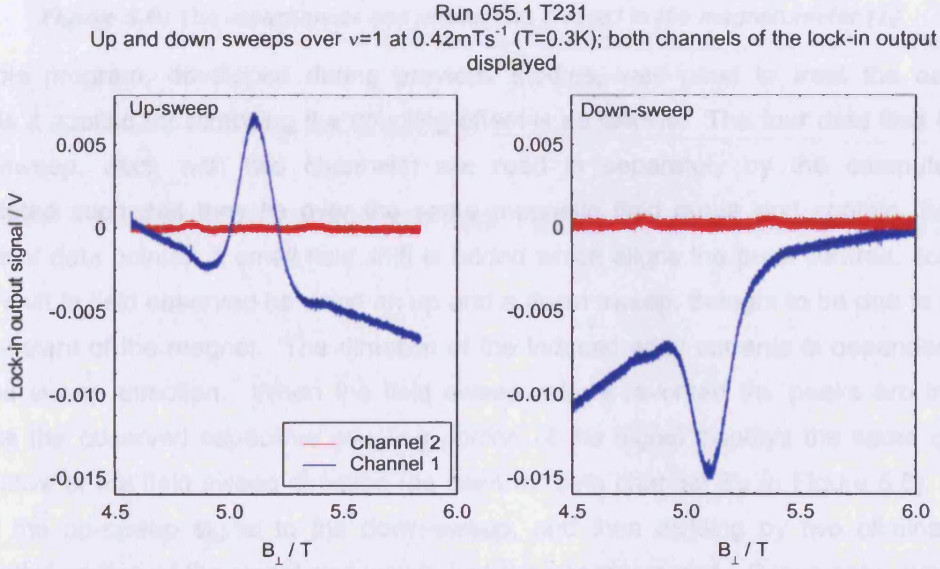

Figure 5.5: *Up and down sweeps for T231, rotated by a phase angle θ =60°. It can be seen that although the peak direction reverses with sweep rate (Channel 1), the direction of the fluctuations in Channel 2 remains the same [Data files: 017x/y, 070x/y].*

It is thought that these deviations are due to capacitive coupling between the 2DEG sample and the stator plates. This can occur if the sample does not sit symmetrically on the rotor and hence lies closer to one stator than the other. If not properly shielded, the sample can form capacitances with each of the plates, and if the sample is not symmetrically positioned these capacitances will not be equal. In previous work at Cardiff [1], where the capacitive coupling was researched in detail, it was found that ensuring the stator plate area was no greater than that of the rotor resulted in a reduction of coupling component observed. In the Mark IIIb magnetometer, the stator plates have a combined area which is slightly smaller than the rotor, but they are not shielded in any way. Furthermore, the sample was too large to fit within the calibration coil (shown in Figure 4.13) as is the usual practice, so it was necessary to mount it on an additional, smaller piece of gallium arsenide in order to clear the calibration coil. This resulted in an elevated sample position from the rotor surface, so reducing the shielding influence of the rotor. As an illustration Figure 5.6 shows a schematic of the capacitances and resistances set up when the sample is not perfectly central.

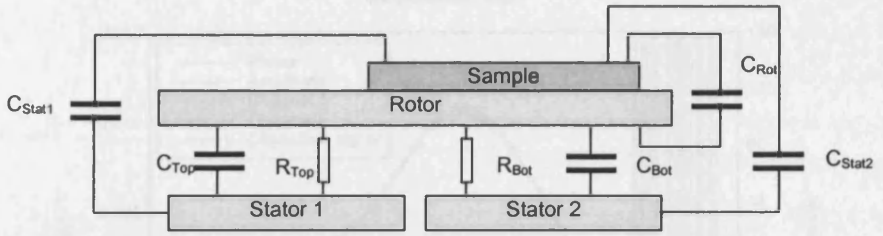

Figure 5.6: *The capacitances and resistances created in the magnetometer [1].*

A simple program, developed during previous studies, was used to treat the data; the principle it applied for removing the coupling effect is as follows. The four data files (up and down sweep, each with two channels) are read in separately by the computer, and interpolated such that they lie over the same magnetic field range and contain the same number of data points. A small field shift is added which aligns the peak centres, correcting for the shift in field observed between an up and a down sweep, thought to be due to the *L-R* time constant of the magnet. The direction of the induced eddy currents is dependent upon the field sweep direction. When the field sweep rate is reversed the peaks are inverted, whereas the observed capacitive coupling portion of the signal displays the same qualities irrespective of the field sweep direction (as seen for both channel 2's in Figure 5.5). Hence adding the up-sweep signal to the down-sweep, and then dividing by two eliminates the mechanical portion of the signal and leaves just the capacitive part. Conversely, subtracting the down-sweep signal from the up-sweep one (and again diving by two) removes the capacitive signal leaving only the mechanical signal, due solely to the deflection of the rotor. The program computes both signals. To find the mechanical signal alone, the user inputs slightly varying values of field shift until the phase becomes virtually constant across the field range, and, simultaneously, the amplitude is maximised.

The resulting data file achieved for the data shown in Figure 5.5 is given in Figure 5.7. The signal of significance, which is the purely mechanical signal with the capacitive signal removed, is labelled as Channel 1. For added interest the capacitive signal is also plotted.

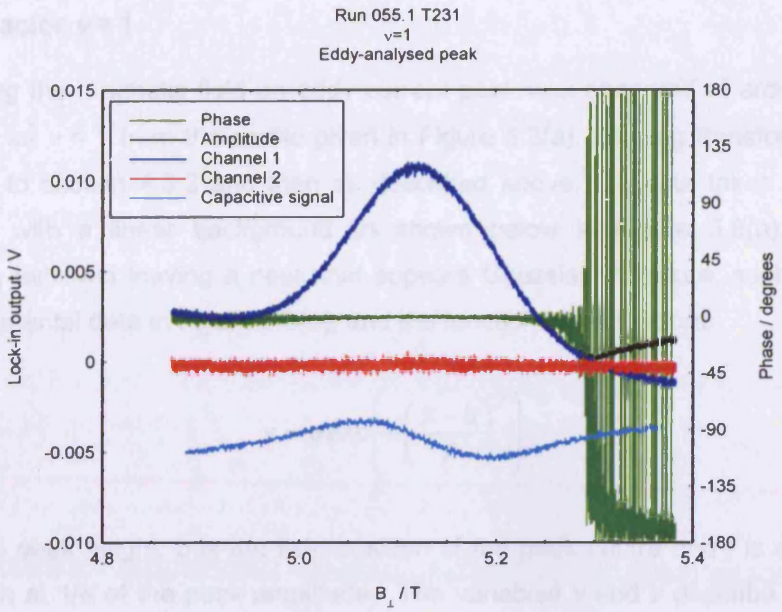

Figure 5.7: *Graph to show the results produced when the up and down sweeps are analysed together to eliminate coupling effects. Channel 1 is the required data set which is later used for analysis of the peak; channel 2 now exhibits the expected flat zero signal; the amplitude is calculated as the sum of the squares of Channels 1 and 2 so always takes a positive value; the phase appears flat at zero across the peak, until Channel 1 approaches zero mV and then becomes negative; the phase swings back and forth between ± 180° because the channels become close to zero and have varying polarity; the capacitive signal is found by adding the up-and down-sweeps, so eliminating any mechanical signal.*

This form of analysis provides us with an eddy current peak free from coupling effects while also generating the form of the coupling signal itself. Thus the capacitive coupling effect is eliminated and it is possible to treat the peak data as follows.

5.1.1 Filling Factor $\nu = 1$

Upon sweeping the magnetic field an eddy current peak was observed at around 5.1T, and was identified as $\nu = 1$ from the profile given in Figure 5.3(a). Having transformed the data file according to section 4.3.3 and then as described above, the data takes the form of a smooth peak with a linear background as shown below in Figure 5.8(a). The linear background is removed leaving a peak that appears Gaussian in nature; such a function is fitted to experimental data in Figure 5.8(d), and the function takes the form

$$y = a\exp\left(-\left(\frac{x-b}{f}\right)^2\right) \tag{5.2}$$

where a is the peak height, b is the field position of the peak centre and f is defined as the peak half-width at 1/e of the peak amplitude. The variables y and x describe lock-in output (V) and magnetic field (T) respectively.

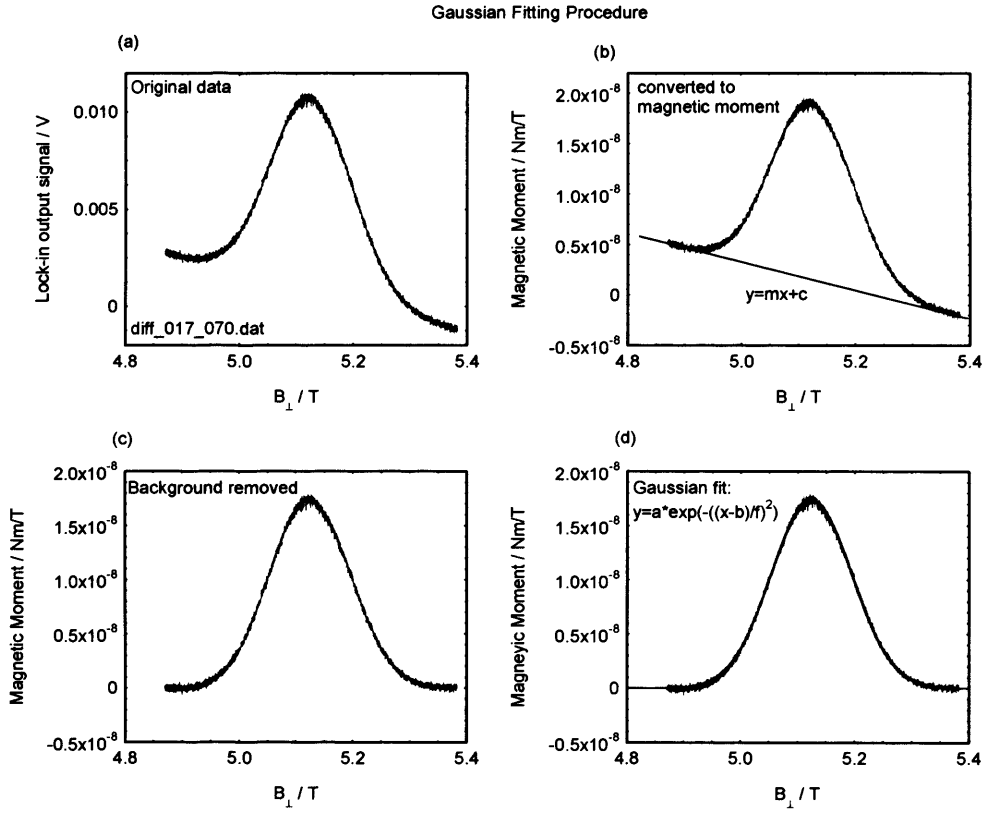

Figure 5.8: *Procedure for analysis of eddy current peaks and fitting of Gaussian curve. (a) The original data is transformed from lock-in voltage (a) to magnetic moment (b) via the calibration constant and instantaneous field; transformed data has a straight line fitted to its background which is removed (c). Then a Gaussian function is fitted to the peak in (d).*

From Equations 4.4 and 4.5 the magnetic moment m can be found through:

$$m = \frac{cV}{B\sin\theta} \tag{5.3}$$

where c is the calibration constant (Nm/V), V is the lock-in output signal (V), B is the instantaneous total field (T), and θ is the angle between the field and sample normal (= 20° in this case). As a result it is possible to convert the voltage signal into magnetic moment through use of the calibration constant; this has been performed in Figure 5.8(b).

The linear background is thought to be a result of magnetic field effects within the gallium arsenide rotor and as such, it is considered reasonable to remove it. By fitting Gaussian functions to this data, where the Gaussian function has parameters of peak height, peak field centre and width, it is possible to build a picture of how these parameters change with respect to sweep rate and temperature.

The magnetic field was swept over the ν=1 peak in both directions, at varying sweep rates and temperatures. Figure 5.9 below shows a series of data sets, taken at four different temperatures.

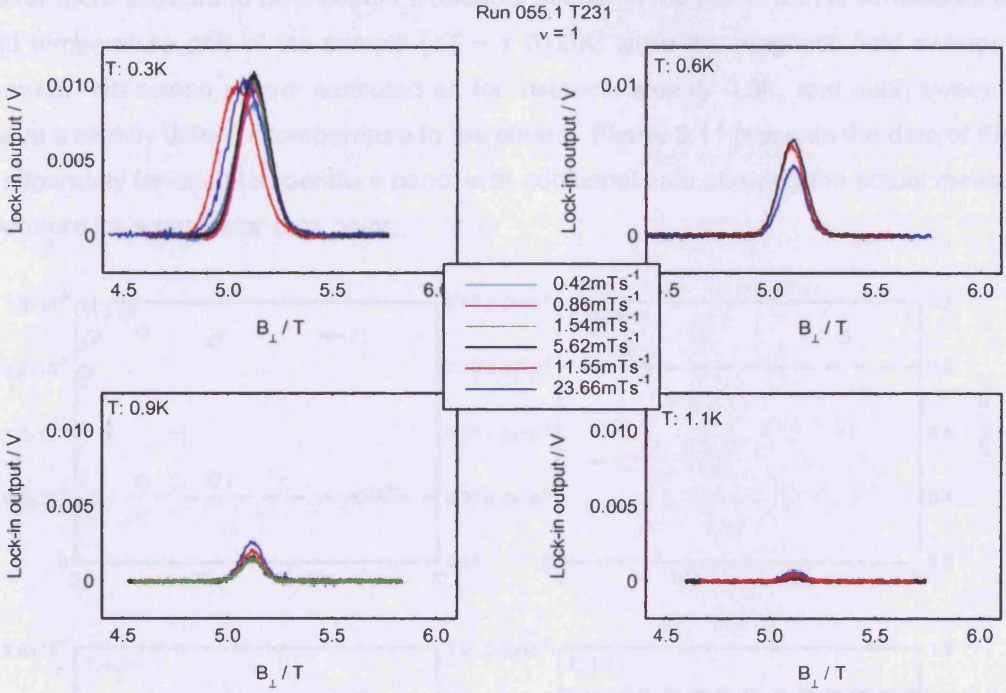

Figure 5.9: *Filling factor ν=1 for sample T231 at varying temperature: lock-in signal (V) versus perpendicular component of magnetic field (T).*

By converting the output signal into magnetic moment and fitting a Gaussian function to each of these peaks (as demonstrated in Figure 5.8), it is possible to examine the temperature and sweep-rate dependence of the peak. Figure 5.10 displays data for peak height in magnetic moment as a function of sweep rate, and at four temperatures. The magnetic moment tends to grow with increasing values of sweep rate and reach saturation at higher sweep rates. The largest signals appear at the lowest temperature and shrink as the temperature rises.

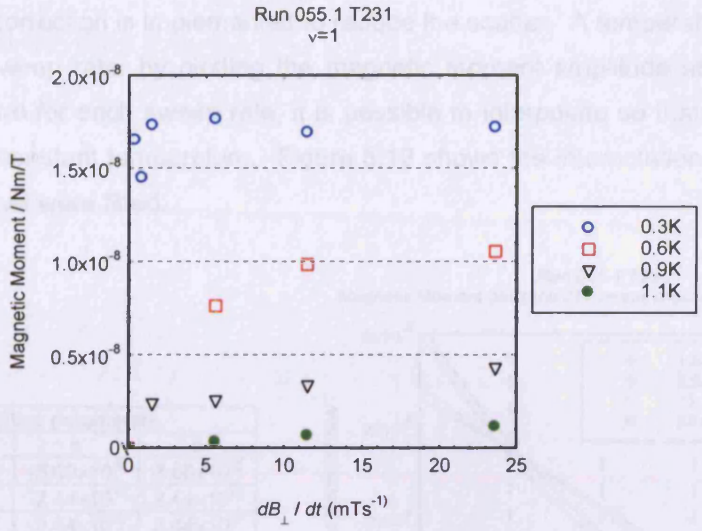

Figure 5.10: *Magnetic moment amplitude (Nm/T) versus sweep rate (mTs^{-1}) for T231. The total sweep rate is again converted to its perpendicular component through multiplication of cos(20).*

However there appears to be a certain amount of scatter in the points that is considered to be due to temperature drift of the sample ($\Delta T \sim \pm 0.05K$) while the magnetic field sweeps are performed. No sweep is ever executed at, for instance, *exactly* 0.3K, and each sweep rate will have a slightly different temperature to the others. Figure 5.11 presents the data of Figure 5.10 separately for each temperature band, with additional data showing the actual measured temperature for a particular data point.

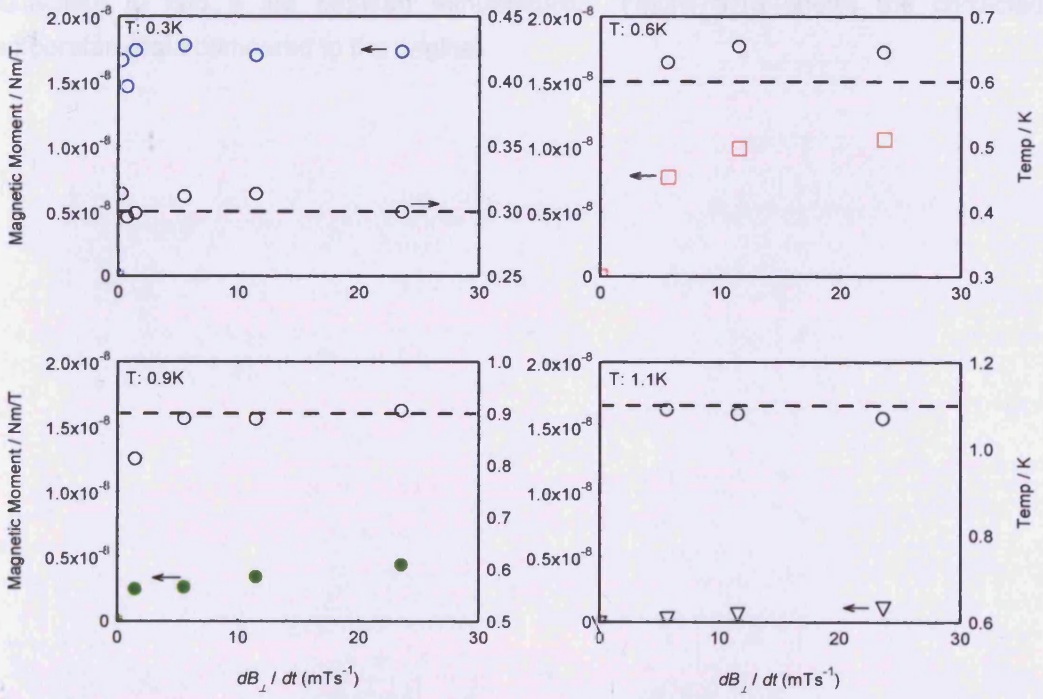

Figure 5.11: *Magnetic moment amplitude (Nm/T) versus perpendicular sweep rate (mTs^{-1}) for T231 with additional temperature data plotted on the right-hand axes. The dotted lines represent the intended temperature; it can be seen that there is a fair amount of scatter in temperature that is likely to affect sample behaviour.*

To adjust for this, a correction is implemented to reduce the scatter. A temperature reading is recorded for each sweep rate; by plotting the magnetic moment amplitude attained at this measured temperature for each sweep rate, it is possible to interpolate so that all points are considered to be at constant temperature. Figure 5.12 shows the interpolation data and the quadratic functions that were fitted.

Sweep Rate / mTs^{-1}	Fitting parameters		
	a	b	c
1.54	2.00×10^{-8}	-5.00×10^{-8}	3.00×10^{-8}
5.62	2.01×10^{-8}	-2.44×10^{-8}	2.44×10^{-8}
11.55	2.47×10^{-9}	-2.44×10^{-8}	2.44×10^{-8}
23.66	-2.20×10^{-9}	-1.82×10^{-8}	2.29×10^{-8}

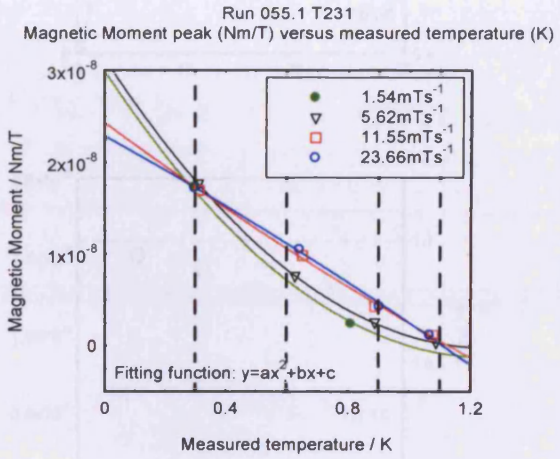

Figure 5.12: *Temperature correction data for T231. Magnetic moment amplitude is plotted for measured temperature and fitted with quadratic functions, the parameters for which are presented in the table.*

From the above graph it is possible to adjust the magnetic moment to the value it would be equivalent to had it the required temperature. Figure 5.13 shows the corrected-for-temperature data compared to the original.

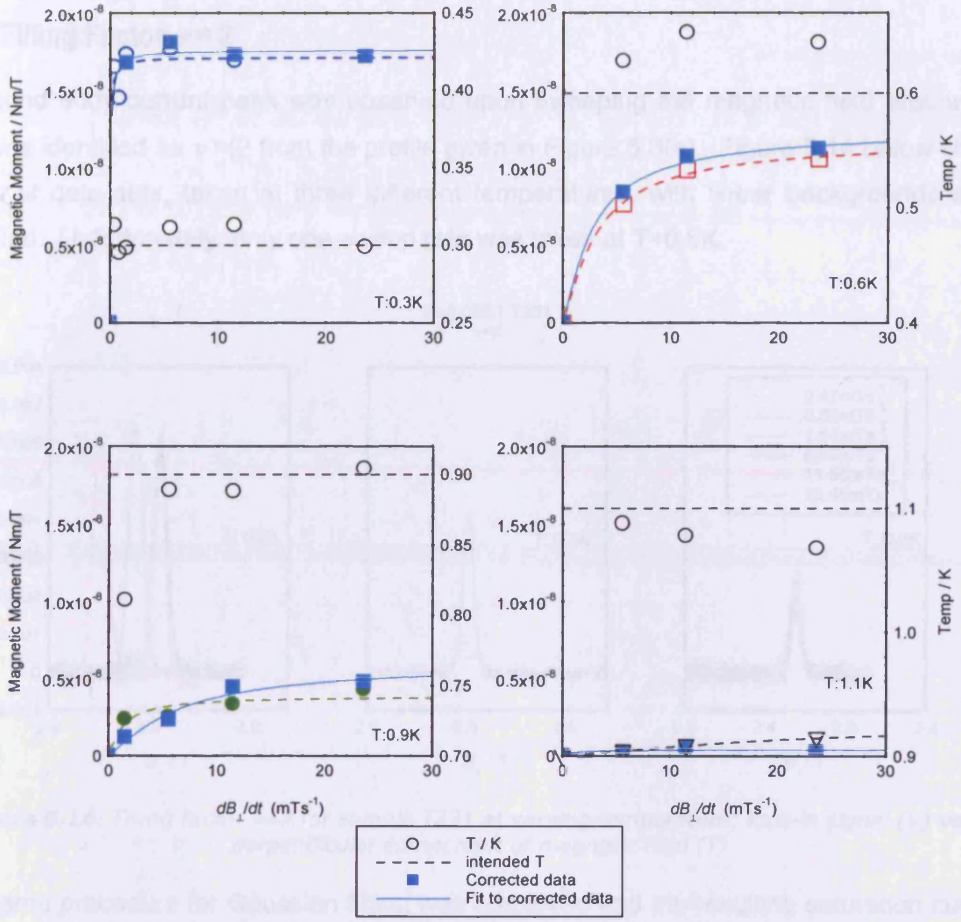

Figure 5.13: *Corrected-for-temperature magnetic moment amplitude (Nm/T) as a function of sweep rate (mTs^{-1}) for T231. The original data is shown with the same (coloured) markers as previously while the corrected data is shown as light blue solid squares for all temperatures. Temperature scatter is also plotted as black circles on the right-hand axes with a dotted line included to demonstrate the intended temperature. Fits of the function y=ax(1-exp(-b/x)) are shown to illustrate improvement of smoothing; this function and its derivation will be discussed in the chapter 6.*

The eddy currents induced in a sample are very dependent on temperature so it is important to reduce the drift as much as possible during measurements. However, it was impossible to hold the cryogenic system at a particular value of elevated temperature for a prolonged period of time so some scatter will inevitably occur. To counter this, the data is amended to smooth any discrepancies which are thought to be due to temperature fluctuations.

5.1.2 Filling Factor $\nu = 2$

A second eddy current peak was observed upon sweeping the magnetic field around 2.5T, and was identified as $\nu = 2$ from the profile given in Figure 5.3(a). Figure 5.14 below shows a series of data sets, taken at three different temperatures, with linear backgrounds already removed. Unfortunately, only one sweep rate was taken at T=0.6K.

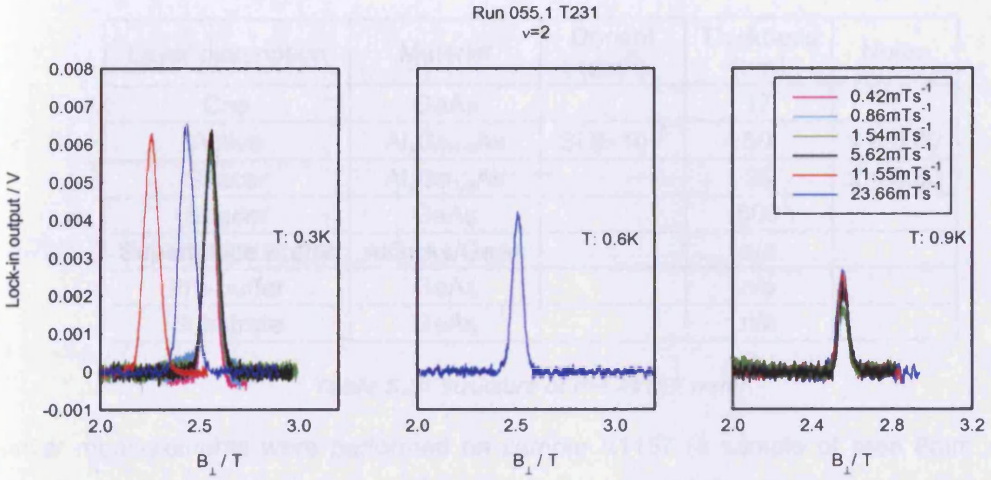

Figure 5.14: *Filling factor ν=2 for sample T231 at varying temperature: lock-in signal (V) versus perpendicular component of magnetic field (T).*

The same procedure for Gaussian fitting was employed and the resulting saturation curve for magnetic moment amplitude as a function of sweep rate for this filling factor is displayed below in figure 5.15.

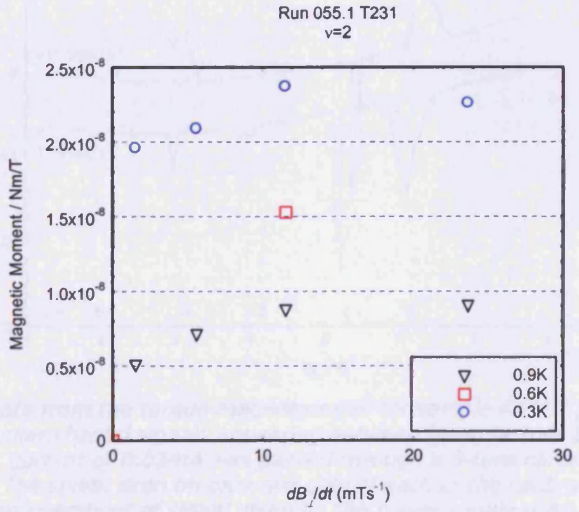

Figure 5.15: *Magnetic moment amplitude (Nm/T) versus sweep rate for T231. The data has been corrected for temperature as described in section 5.1.1.*

The signal is observed to grow with sweep rate until it reaches a saturation value and increases no further, and the eddy current peak height reduces in amplitude as the temperature rises.

5.2 Sample A1157

A1157 was grown by molecular beam epitaxy at the Department of Electronic and Electrical Engineering of the University of Glasgow. A classical Hall effect measurement after growth gave a number density of $4.5\times10^{15}m^{-2}$ at 77K. A layer profile is given in Table 5.3, and Figure 5.16 shows a raw data trace.

Layer description	Material	Dopant (cm^{-3})	Thickness (nm)	Notes
Cap	GaAs		17	
Active	$Al_xGa_{1-x}As$	Si 8×10^{17}	50	x = 0.30
Spacer	$Al_xGa_{1-x}As$		25	x = 0.30
Spacer	GaAs		500	
Superlattice Buffer	AlGaAs/GaAs		n/a	
Pre-buffer	GaAs		n/a	
Substrate	GaAs		n/a	

Table 5.3: *Structure of the A1157 wafer.*

Similar measurements were performed on sample A1157 (a sample of area 8mm × 8mm) using the same set of magnetic field sweep rates, but slightly differing temperature bands. The background signal produced by the rotor is again noticeable in Figure 5.3.

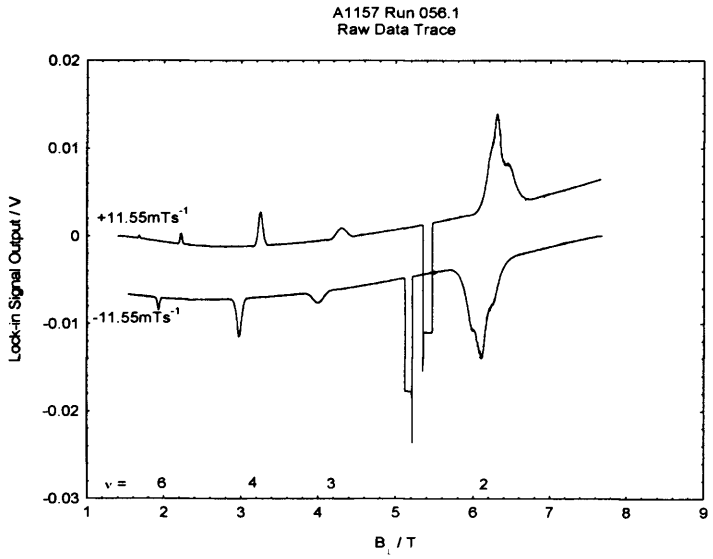

Figure 5.16: *Raw data from the torque magnetometer for sample A1157 [Data files: 083.dat, 084.dat]. The rectangular shaped signals appearing between filling factors 2 and 3 are calibration signals. A calibration current of 0.03mA was passed through a 3-turn calibration coil with cross-sectional area 1.1cm². The spike, seen on only one side of each of the calibrations, is assumed to be an overshoot of signal given by the power supply used.*

This trace also includes the application of a calibration current through the calibration coil, resulting in the deflection of the rotor. From this change in signal it is possible to calibrate the probe as described in section 5.3.4. The calibration constant was found to be 1.58×10^{-6} Nm/V (or 6.34×10^{8} mV/Nm), allowing the torque or magnetic moment to be realised from the lock-in voltage signal.

The number density for this particular sample is calculated from the filling factor profile shown below in Figure 5.17.

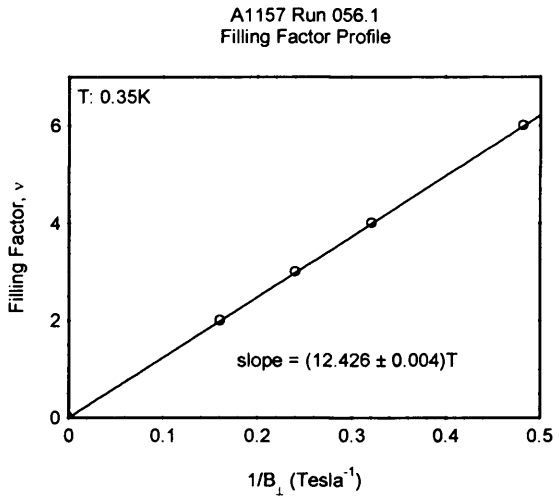

Figure 5.17: *Graph showing estimated filling factor ν against the inverted observed peak position in field, 1/B.*

The gradient of the line of best fit shown above is 12.426T which provides an electron density of n_s = (3.004 ± 0.001)×$10^{15}m^{-2}$. Illumination was not attempted for A1157 as had been for the previous sample.

There also appeared to be no capacitive coupling for this sample as for T231, so it was unnecessary to use the procedure outlined above to eliminate this additional signal. With an area of (8mm × 8mm) it is likely that the sample was better shielded from the stator plates by the rotor than the larger (12mm × 12mm) T231. In fact it was possible to fit A1157 within the cross-sectional area of the calibration coil so it is quite conceivable that the coil provided further shielding. In this case then, the procedure for data analysis was simply as follows: the raw data file was transformed so that the two portions of signal from each lock-in channel were converted into a single signal; then the linear background was removed.

5.2.1 Filling Factor $\nu = 2$

As expected a series of peaks were observed for sweeping magnetic field over the range (0 - 12T), the highest observed being that of $\nu = 2$. This was a particularly interesting peak, displaying a shape not seen for T231; as well as the main peak, two additional shoulder-like structures appeared on either side, with the more pronounced shoulder always occurring on the high-field side of the peak. Figure 5.18 shows a series of $\nu = 2$ peaks over a range of sweep rates and four temperatures.

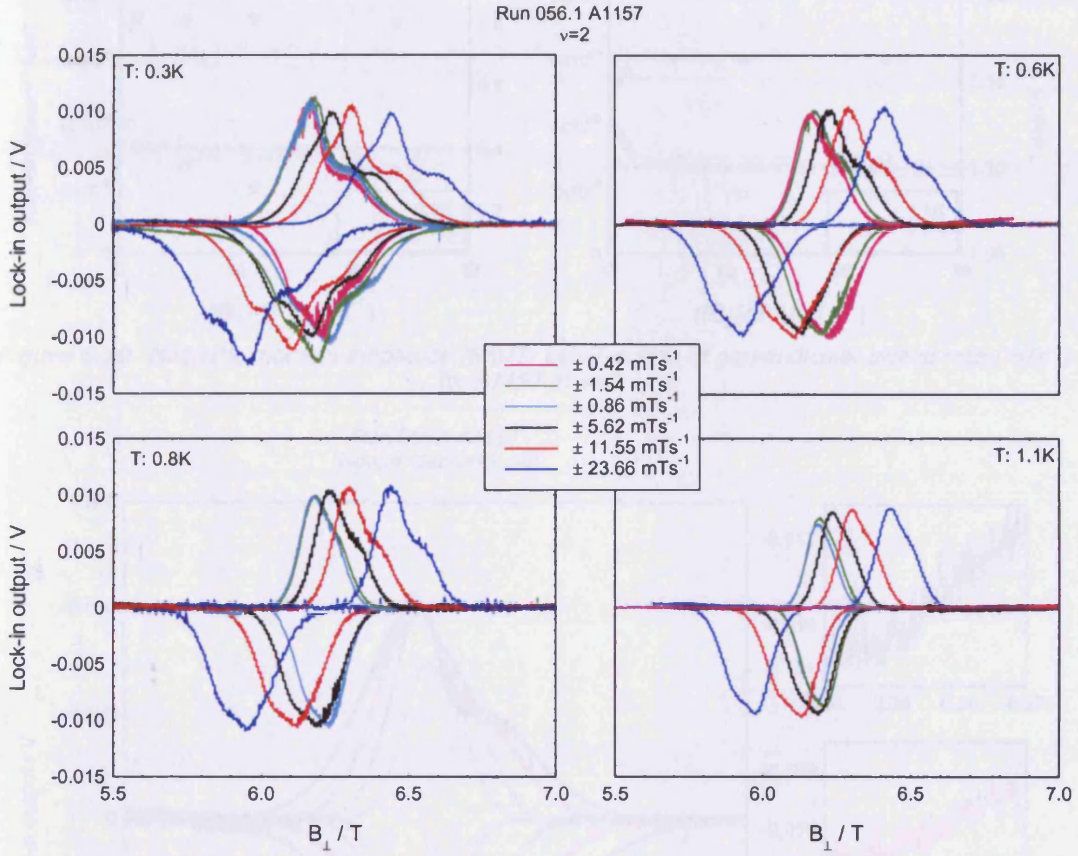

Figure 5.18: *Filling factor ν=2 for sample A1157 at varying temperature: lock-in signal (V) versus perpendicular component of magnetic field (T).*

It was not possible to convincingly fit a single Gaussian function to these peaks (it was found that these signals are compellingly fitted by three Gaussian functions; this is discussed in chapter 6). Consequently, the peak height plotted here was measured manually and converted into magnetic moment to enable the construction of the saturation graphs as seen for T231. Such a graph is displayed in Figure 5.19. As before, scatter in the points implies non-constant temperature, and this has been corrected for in the graphs above.

Another very interesting effect seen at $\nu = 2$ is that of the fine structure noise seen on the peak. Although this will be discussed in detail in following chapters it is interesting to highlight at this stage how the noise develops with temperature, as shown on figure 5.20.

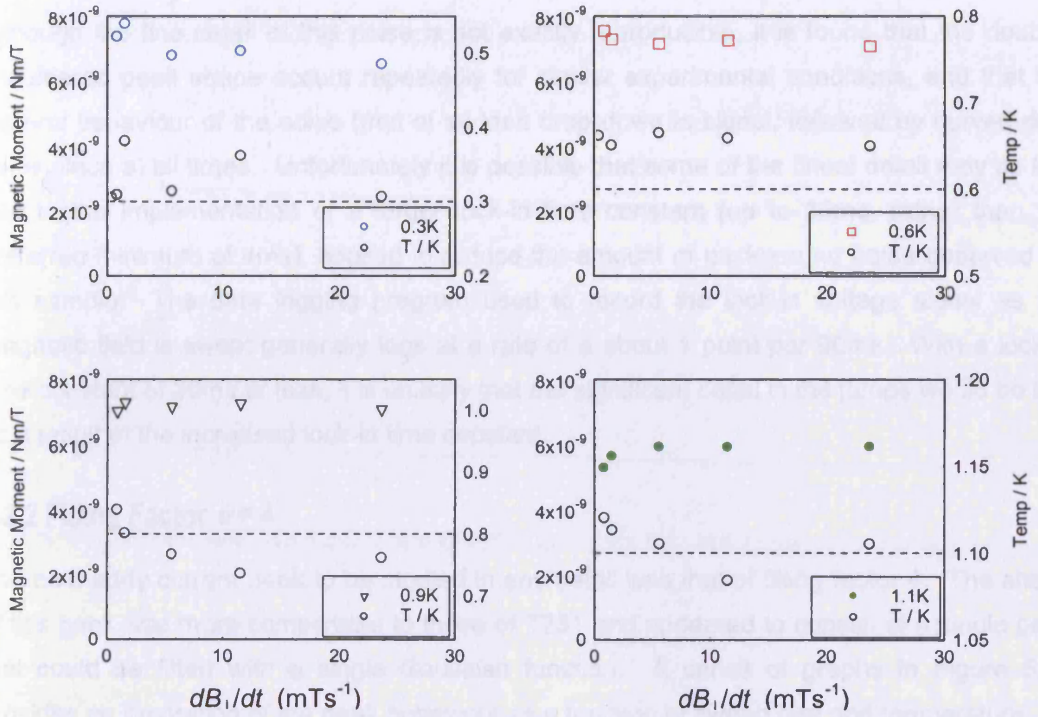

***Figure 5.19**: Magnetic moment amplitude (Nm/T) as a function of perpendicular sweep rate (mTs^{-1}) for A1157 at ν=2.*

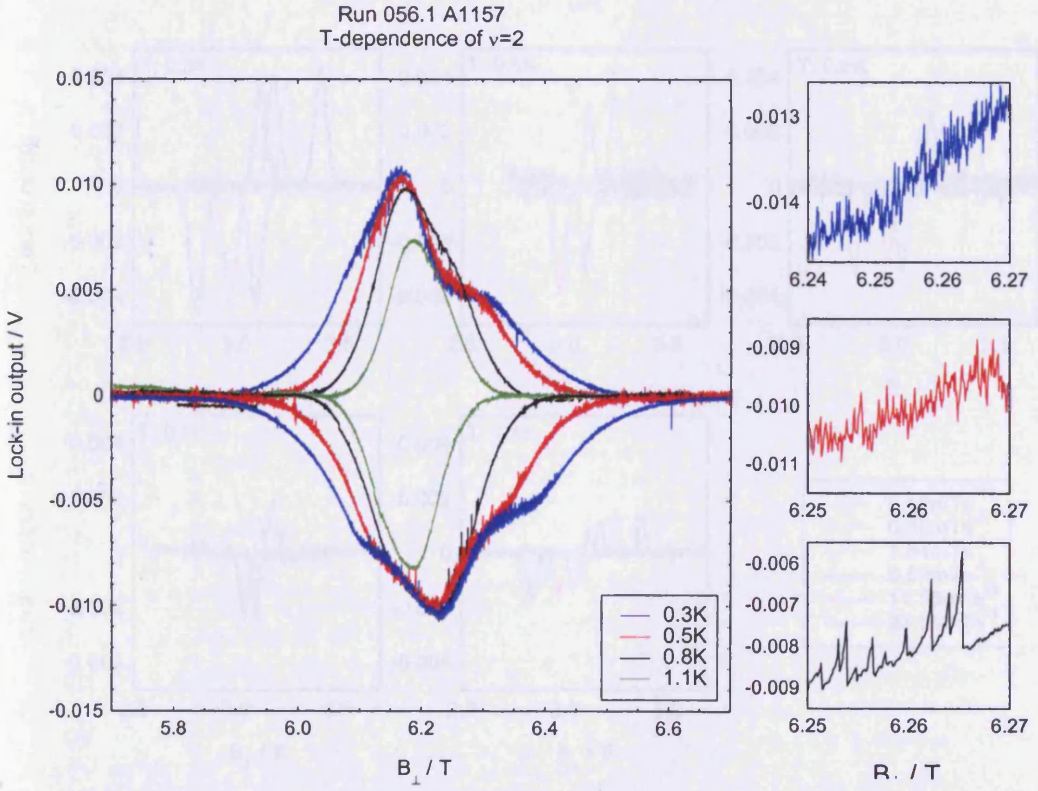

***Figure 5.20:** Temperature-dependence of ν=2 for A1157 at constant sweep rate. As temperature decreases the fine structure noise begins to appear on the peak as it grows in height accompanied by the development of the shoulders. The inset graphs show portions of the down-sweep curves (colour-matched) in finer detail; at higher temperature the noise consists of sudden large jumps in signal that then grow back towards the original amplitude, the jumps become less pronounced at lower temperature.*

Although the fine detail of this noise is not exactly reproducible, it is found that the double-shouldered peak shape occurs repeatedly for similar experimental conditions, and that the general behaviour of the noise (that of sudden drop down in signal, followed by curved rise) takes place at all times. Unfortunately it is possible that some of the finest detail may be lost due to the implementation of a larger lock-in time constant (up to 30ms, rather than the preferred minimum of 1ms), applied to reduce the amount of background noise observed for this sample. The data logging program used to record the lock-in voltage signal as the magnetic field is swept generally logs at a rate of a about 1 point per 90ms. With a lock-in time constant of 30ms or less, it is unlikely that the significant detail in the jumps would be lost as a result of the increased lock-in time constant.

5.2.2 Filling Factor $\nu = 4$

The next eddy current peak to be studied in any detail was that of filling factor 4. The shape of this peak was more comparable to those of T231 and appeared to consist of a single peak that could be fitted with a single Gaussian function. A series of graphs in Figure 5.21 provides an illustration of the peak behaviour as a function of sweep rate and temperature.

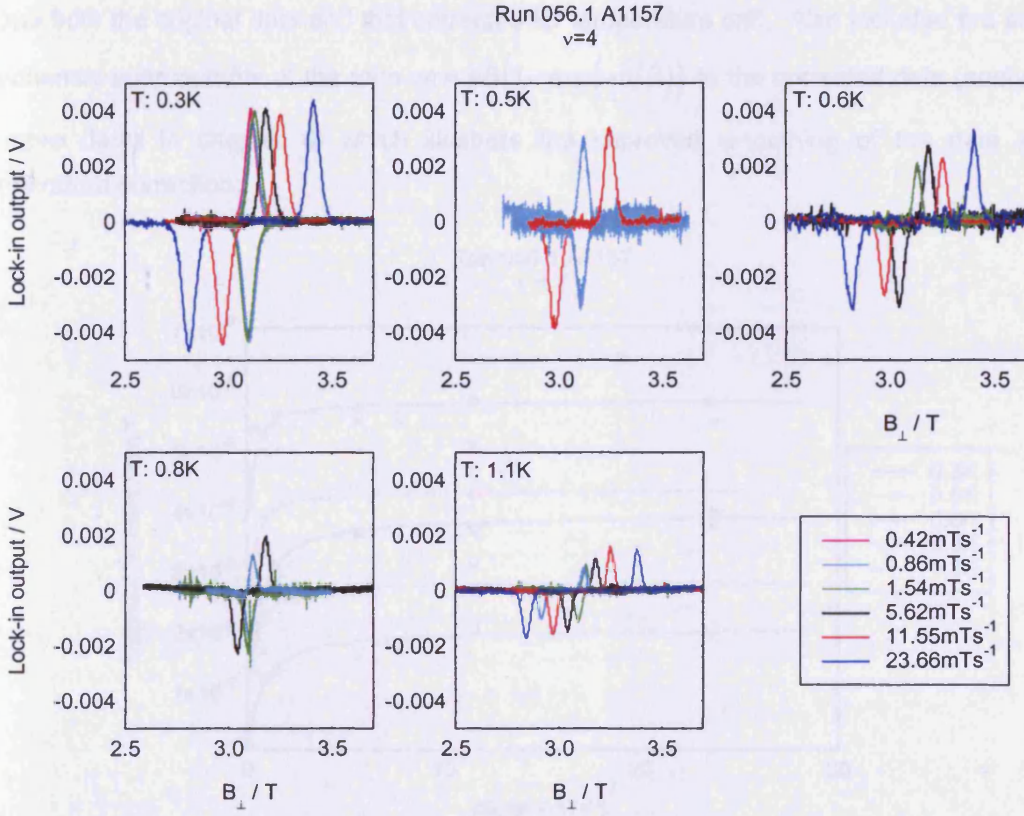

Figure 5.21: *Filling factor ν=4 for sample A1157 at varying temperature: lock-in signal (V) versus perpendicular component of magnetic field (T).*

Again, it can be seen that the signal height decreases with rising temperature, and rises towards saturation with increasing sweep rate.

Peak amplitudes were corrected for temperature as given in Figure 5.22.

Fitting function: $y=ax^2+bx+c$

Sweep Rate / mTs^{-1}	Fitting Parameters		
	a	b	c
0.86	3.57×10^{-9}	-1.00×10^{-8}	7.91×10^{-9}
1.54	5.67×10^{-9}	-1.33×10^{-8}	9.05×10^{-9}
5.62	3.05×10^{-9}	-9.30×10^{-9}	8.17×10^{-9}
11.55	4.57×10^{-9}	-1.11×10^{-8}	8.67×10^{-9}
23.66	2.80×10^{-9}	-8.59×10^{-9}	8.06×10^{-9}

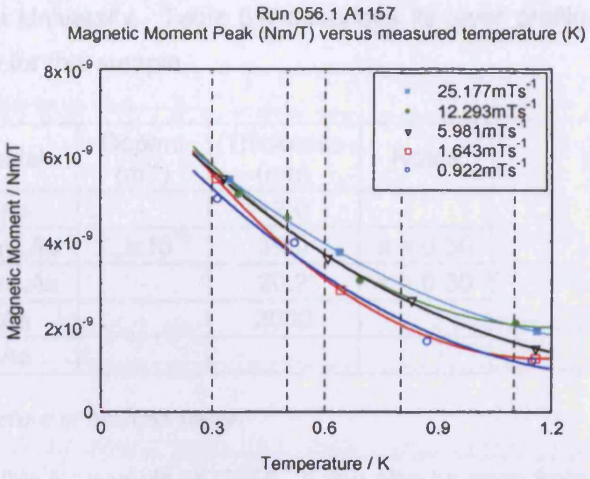

Figure 5.22: *Temperature correction data for ν=4 on sample A1157. Magnetic moment amplitude is plotted against measured temperature and fitted with quadratic functions, the parameters for which are presented in the table.*

Converting the peak amplitude into magnetic moment and plotting against sweep rate produces the following saturation curves for each temperature in Figure 5.23. The figure shows both the original data and that corrected for temperature drift. Also included are some exponential approach fits of the form $m = a\dot{B}\left(1-\exp\left(-b/\dot{B}\right)\right)$ to the corrected data (analysed in more detail in chapter 6) which illustrate the improved smoothing of the data after temperature correction.

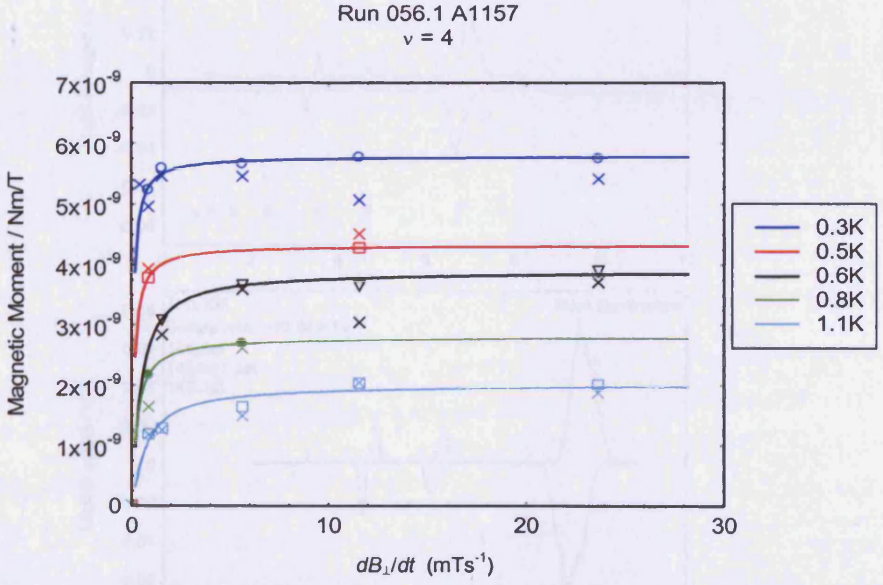

Figure 5.23: *Corrected-for-temperature magnetic moment amplitude (Nm/T) as a function of sweep rate (mTs^{-1}) for A1157 at varying temperature. Original data is marked as crosses for each temperature, and the corresponding temperature-corrected data is shown in the same colour, with differing markers. Correcting for temperature smoothes the scatter of the points somewhat. Exponential fits to the data are displayed and will be explained in more detail in subsequent chapters.*

5.3 Sample NU2055

NU2055 was grown by MBE at Nottingham University. Table 5.4 describes its layer profile and Figure 5.24 shows a typical signal trace for this sample.

Layer description	Material	Dopant (m^{-2})	Thickness (nm)	Notes
Cap	GaAs	-	17.0	
Active	$Al_xGa_{1-x}As$	$1.3x10^{18}$	39.0	x = 0.30
Spacer	$Al_xGa_{1-x}As$	-	20.2	x = 0.30
Spacer	GaAs	-	2000	
Semi-insulating substrate	GaAs			

Table 5.4: *Structure of NU2055 wafer.*

Filling factors $\nu = 2, 3, 4, 6, 8$ are clearly visible for sample NU2055. It can also be seen from the raw data of Figure 5.24 that the background signal is greatly improved compared to that for sample T231 and A1157. Data for NU2055 was taken with the Mark IIIc probe and the reduction of background is thought to be attributed to the symmetrical shape of the rotor. The calibration constant for this experimental run was found to be 2.27×10^{-7} Nm/V (or 4.40×10^{-9} mV/Nm).

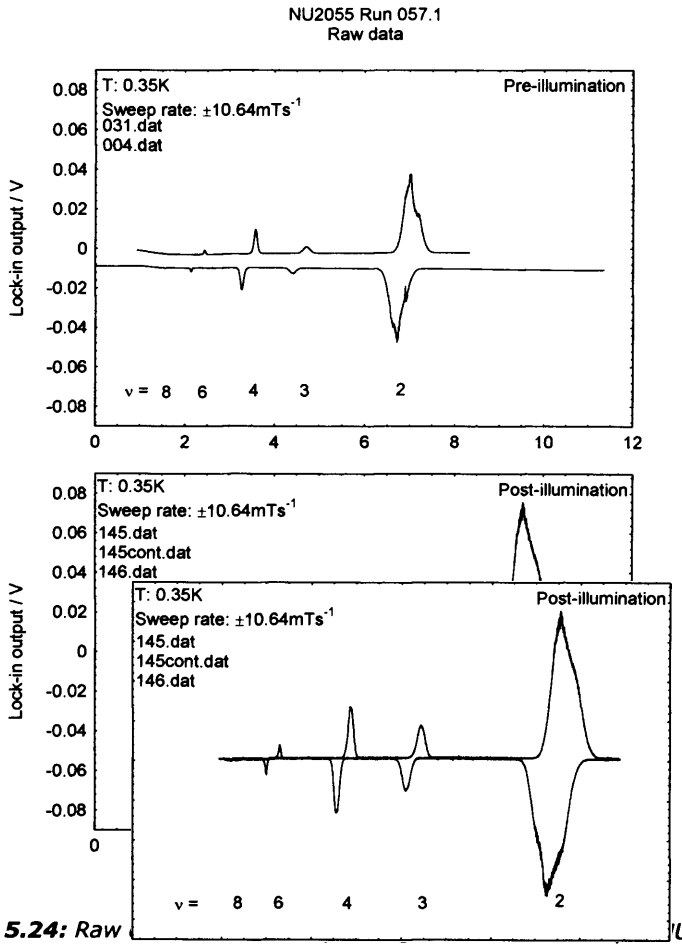

Figure 5.24: *Raw* *NU2055.*

The sample was illuminated with a low temperature tested LED. A current of around 13mA was passed through the LED and a 4.6kΩ resistor connected in series for around 1 second. The effects of such illumination are displayed in the lower graph of Figure 5.24.

In addition to the much reduced background signal there did not appear to be the capacitive coupling effect as observed for sample T231. As such it was not necessary to treat the data specially in order to eliminate this signal. Instead the data was transformed as described in section 4.3.3; it was then also unnecessary to remove any linear background signal since the improved performance attained with the Mark IIIc probe eliminated this extra signal from the results. Furthermore, the lock-in amplifier phase angle was altered during the experimental run in order to direct the entire signal from the magnetometer through only one lock-in channel. All the data files recorded from this point in the run did not require the transformation procedure explained in section 4.3.3, since channel 1 carried the whole signal while channel 2 consisted basically of zero values. Figure 5.25 shows the filling factor profiles for sample NU2055 both before and after illumination, and the electron densities in each case are summarised in Table 5.5 below.

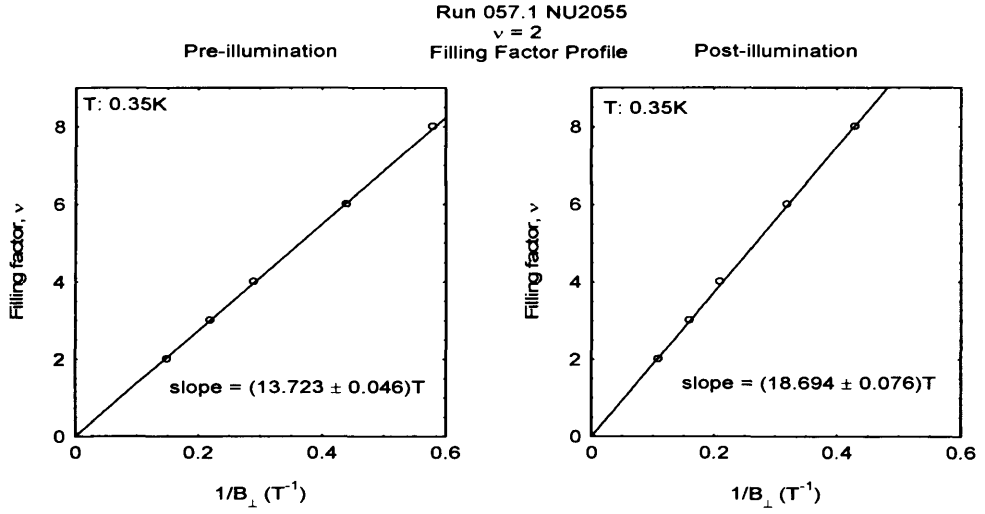

Figure 5.25: *Graph showing estimated filling factor ν against the inverted observed peak position in field, $1/B_{\perp}$.*

	gradient / T	n_s / m^{-2}
Pre-illumination	(13.723 ± 0.046)	$(3.318 \pm 0.011)\times10^{15}$
Post-illumination	(18.694 ± 0.076)	$(4.520 \pm 0.018)\times10^{15}$

Table 5.5: *Comparison of electron number density for NU2055 before and after illumination.*

As for sample T231 it can be seen that the electron density for NU2055 has increased upon illumination. A considerable amount of data was taken for sample NU2055 both before and after illumination. The following subsections discuss each filling factor in full, dealing first with pre-illumination data, then post-illumination data, before moving on to the following filling factor.

5.3.1 Filling Factor $\nu = 2$

- **Pre-illumination data**

The highest observed peak for sample NU2055 was that of $\nu = 2$. Interestingly, this peak included two shoulder-like structures on each side, akin to the peak of A1157 for the same index. Figure 5.26 shows a series of $\nu = 2$ peaks over a range of sweep rates and four temperatures.

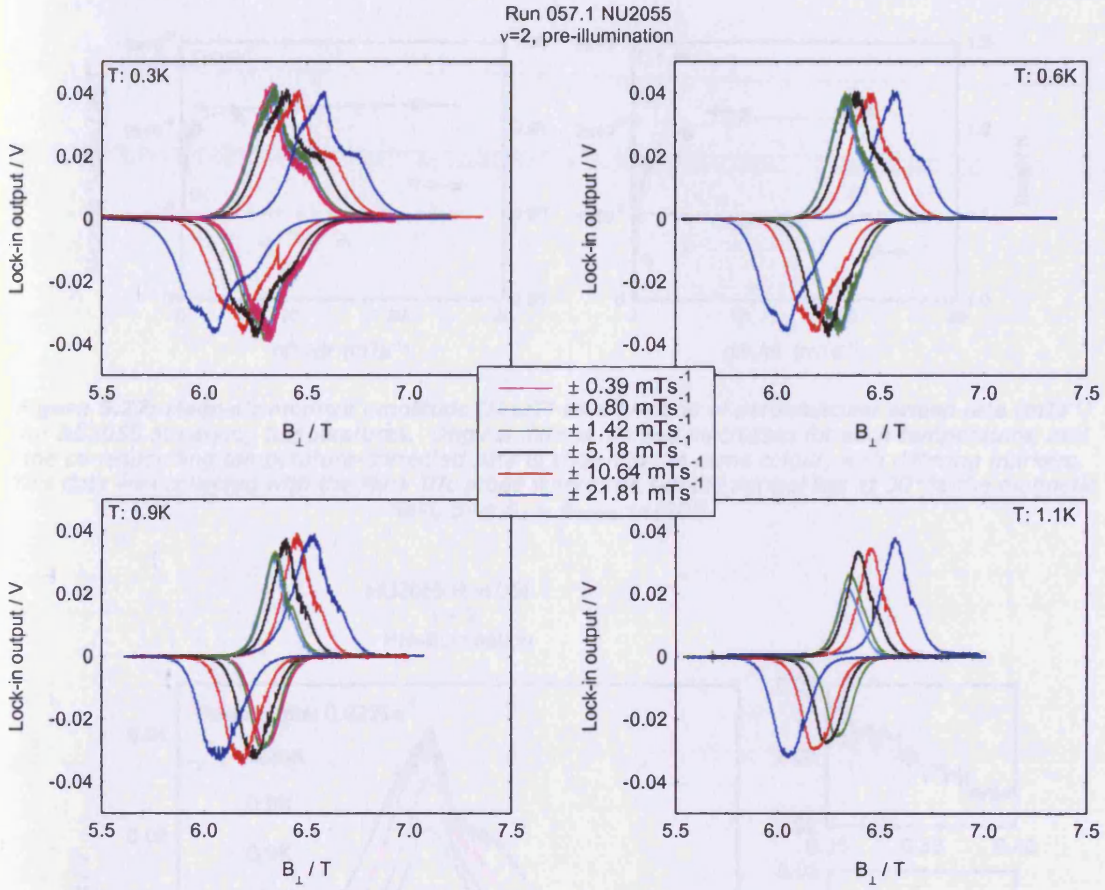

Figure 5.26: *Filling factor ν=2 for sample NU2055 at varying temperature: lock-in signal (V) versus perpendicular component of magnetic field (T).*

As anticipated, the peak grows with increasing sweep rate and decreasing temperature. Again, the peak height was measured manually and converted into magnetic moment to enable the construction of the saturation graphs also displayed in Figure 5.27.

The data points in Figure 5.27 have been corrected for temperature drift; for comparison both the original data sets and that of the corrected data are displayed, together with the relevant fits (discussed later) to each data set.

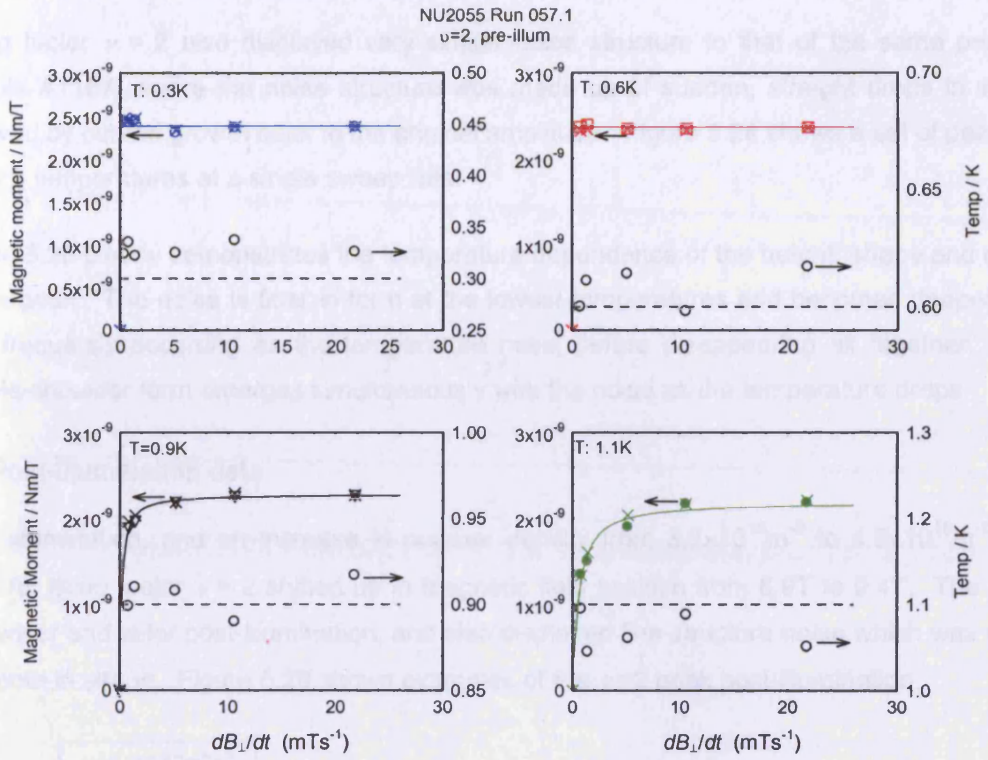

Figure 5.27: *Magnetic moment amplitude (Nm/T) as a function of perpendicular sweep rate (mTs^{-1}) for NU2055 at varying temperatures. Original data is marked as crosses for each temperature, and the corresponding temperature-corrected data is shown in the same colour, with differing markers. This data was collected with the Mark IIIc probe where the sample normal lies at 30° to the magnetic field, thus $B_\perp = B_{TOTAL}\cos(30°)$.*

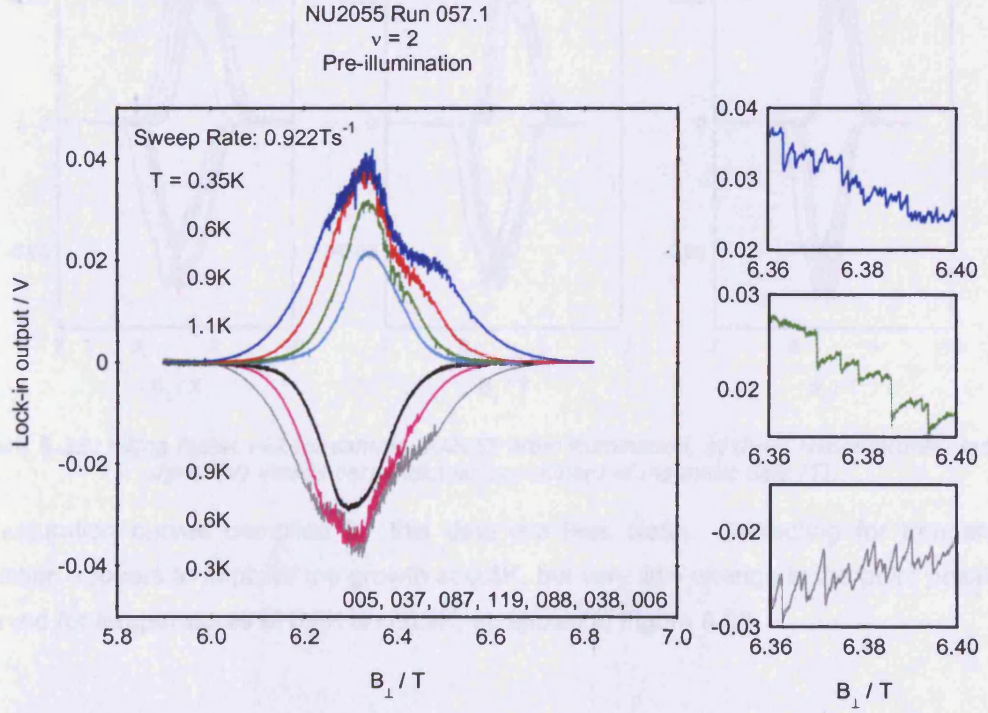

Figure 5.28: *Temperature-dependence of ν=2 for NU2055 at constant sweep rate ($0.80mTs^{-1}$). The inset graphs show portions of the down-sweep curves (colour-matched) in finer detail; at higher temperature the noise consists of sudden large jumps in signal that then grow back towards the original amplitude, the jumps become less pronounced at lower temperature.*

Filling factor $\nu = 2$ also displayed very similar noise structure to that of the same peak in sample A1157, where the noise structure was made up of sudden, straight drops in signal followed by curved growth back to the original amplitude. Figure 5.28 shows a set of peaks at for four temperatures at a single sweep rate.

Figure 5.28 clearly demonstrates the temperature dependence of the height, shape and noise of the peak. The noise is finer in form at the lowest temperatures and becomes deeper and less frequently occurring as the temperature rises, before disappearing all together. The double-shoulder form emerges simultaneously with the noise as the temperature drops.

- **Post-illumination data**

After illumination, and an increase in number density from $3.3\times10^{15}m^{-2}$ to $4.5\times10^{15}m^{-2}$, the peak for filling factor $\nu = 2$ shifted up in magnetic field position from 6.9T to 9.4T. The peak was wider and taller post-illumination, and also displayed fine structure noise which was more sawtooth in shape. Figure 5.29 shows examples of the $\nu = 2$ peak post-illumination.

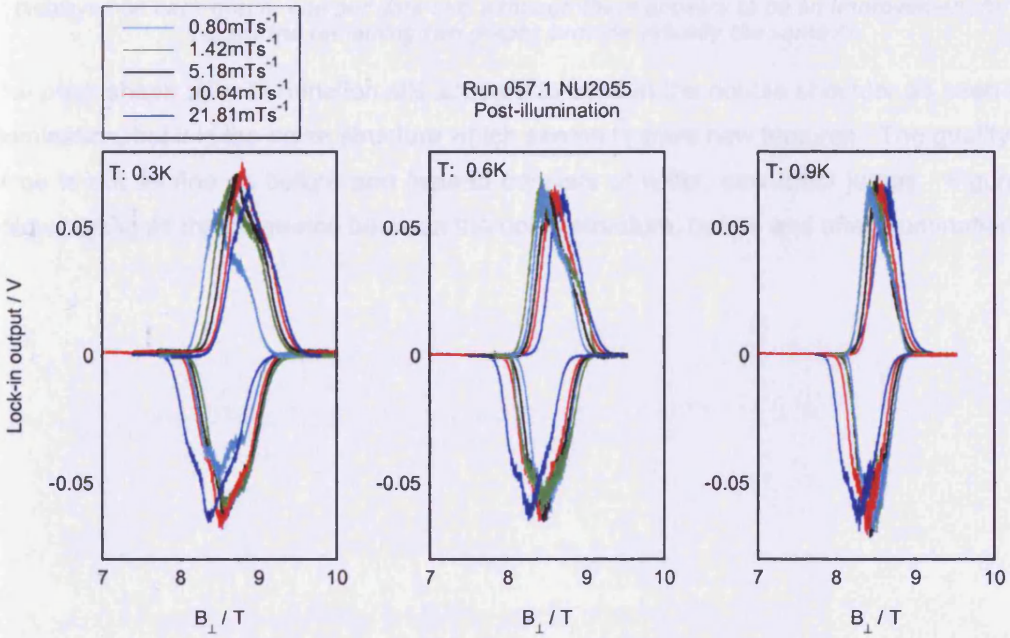

Figure 5.29: *Filling factor ν=2 for sample NU2055 after illumination, at three temperatures: lock-in signal (V) versus perpendicular component of magnetic field (T).*

The saturation curves compiled for this data are less clear. Correcting for temperature fluctuation appears to improve the growth at 0.3K, but very little change in the point position is observed for temperatures at 0.6K and 0.9K, as shown in Figure 5.30.

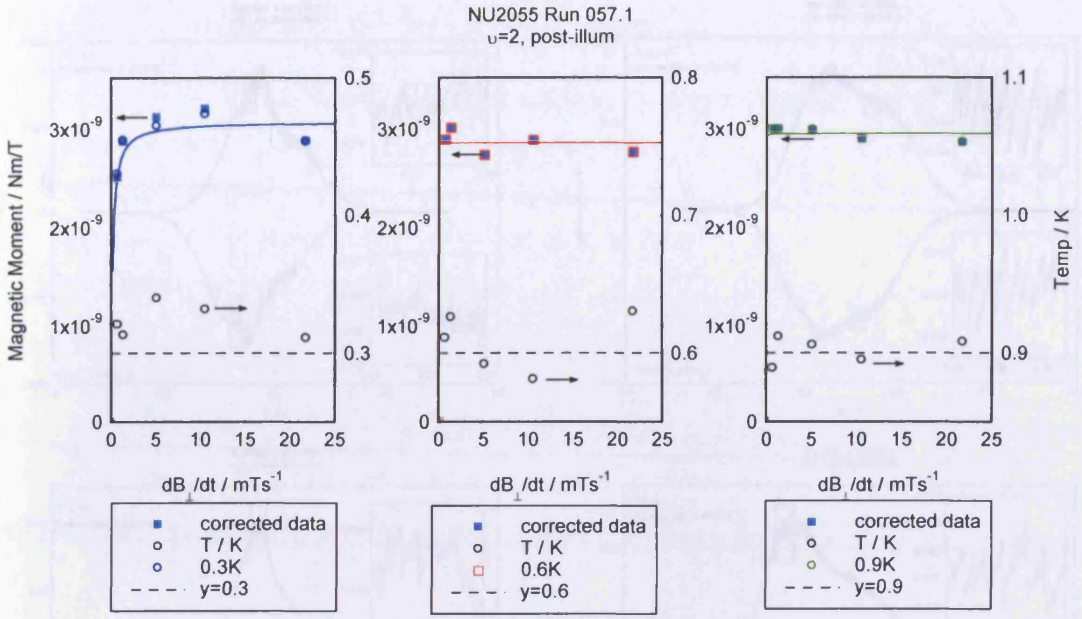

Figure 5.30: *Corrected-for-temperature magnetic moment amplitude (Nm/T) as a function of parallel sweep rate (mTs^{-1}) for NU2055 at varying temperatures after illumination. Original data is marked as well as the corresponding temperature-corrected data is shown in light blue. Two fitting functions are displayed on each graph, one per data set; although there appears to be an improvement for T = 0.3K, the remaining two graphs provide virtually the same fit.*

The peak shape after illumination still appears to contain the double shoulder as seen before illumination, but it is the noise structure which seems to have new features. The quality of the noise is not as fine as before and instead consists of wider, saw-tooth jumps. Figure 5.31 below highlights the difference between the noise structure, before and after illumination.

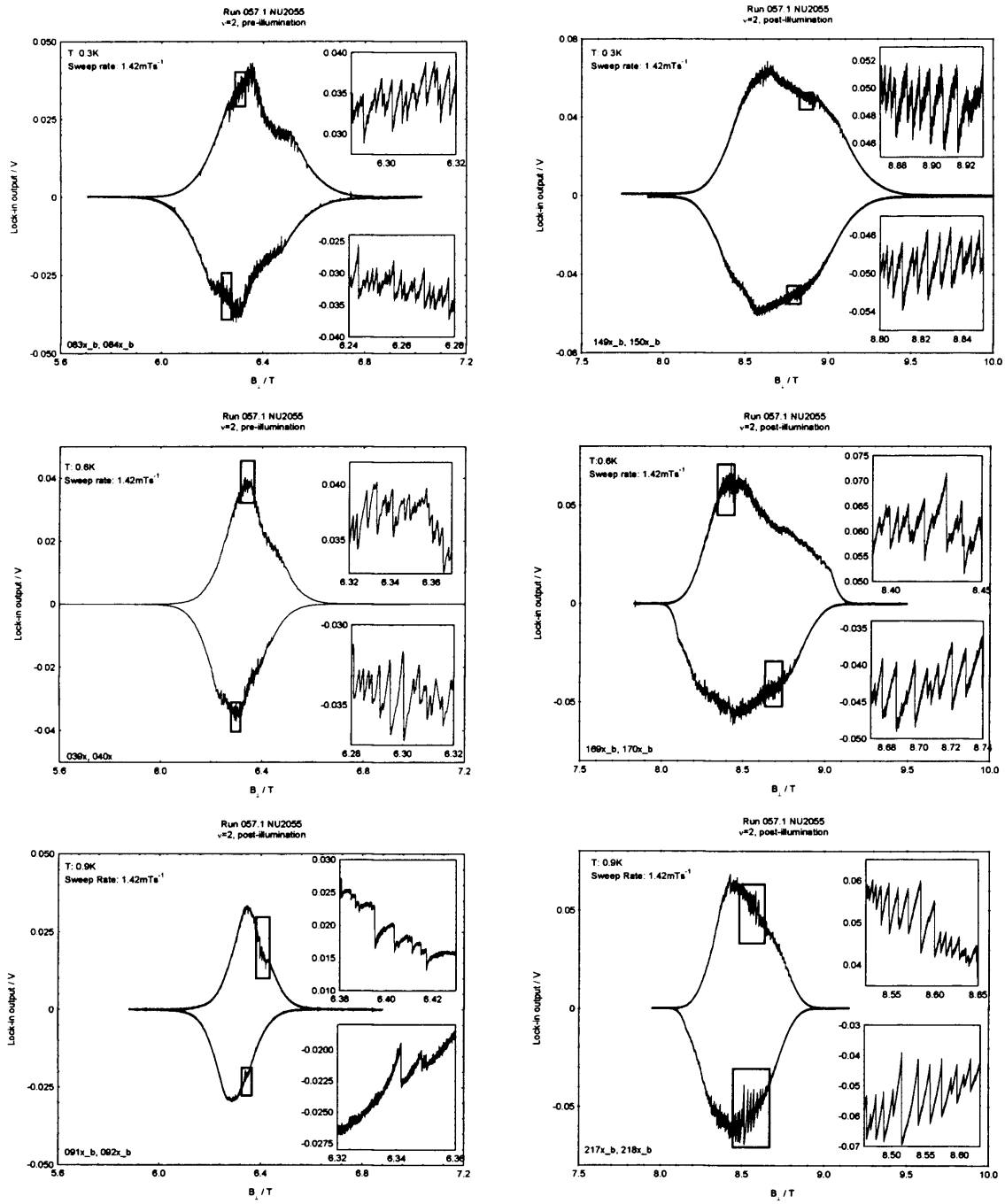

Figure 5.31: *Appearance of noise with temperature, including differing structures of noise: a fine structure pre-illumination (left-hand column) and a sawtooth structure post-illumination (right-hand column).*

The noise observed above is thought to be an example of self-organised criticality which is discussed in chapter 7.

5.3.2 Filling Factor $\nu = 4$

After filling factor $\nu = 2$, the next observable peak was $\nu = 3$ at a magnetic field of around 5.4T. This peak could be seen at a base temperature of 0.3K, but disappeared when the temperature was raised to 0.6K. It did not appear to exhibit any noisy structure across the peak. Consequently, filling factor $\nu = 4$, which was found to be more robust at elevated temperatures was studied in more detail.

- **Pre-illumination data**

Filling factor $\nu = 4$ occurred at a magnetic field of around 3.1T, and could be fitted relatively well by a single Gaussian function. Figure 5.32 below shows typical peaks over a range of sweep rates.

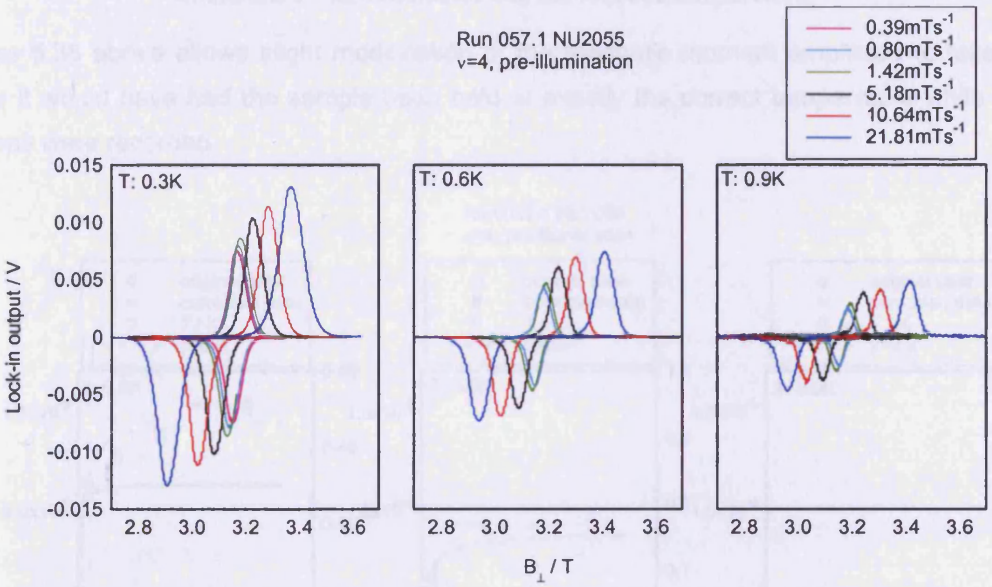

Figure 5.32: *Filling factor ν=4 for sample NU2055 before illumination at varying temperature: lock-in signal (V) versus perpendicular component of magnetic field (T).*

The data obtained for this filling factor clearly shows the growth of the eddy current with sweep rate, as well as the effect of increasing the sample temperature on this signal.

Having converted the raw voltage signal into magnetic moment and fitted Gaussian functions to each peak, the peak heights were corrected for any possible temperature fluctuations. Figures 5.33 and 5.34 below show the temperature correction method and then a comparison between the original and the corrected data.

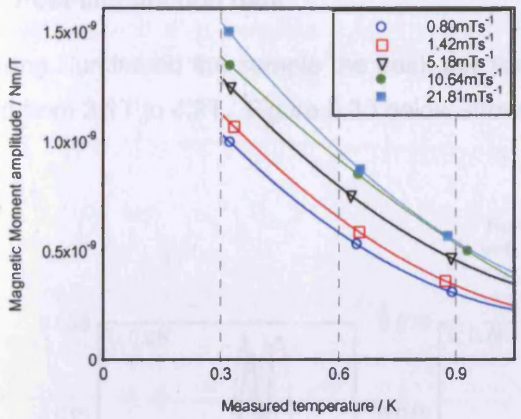

Fitting Function: $y=ax^2+bx+c$

Sweep Rate / mTs^{-1}	Fitting Parameters		
	a	b	c
0.90	9.68×10^{-10}	-2.38×10^{-9}	1.66×10^{-9}
1.42	9.25×10^{-10}	-2.42×10^{-9}	1.76×10^{-9}
5.18	8.87×10^{-10}	-2.46×10^{-9}	1.94×10^{-9}
10.64	4.76×10^{-10}	-1.99×10^{-9}	1.93×10^{-9}
21.81	9.45×10^{-10}	-2.80×10^{-9}	2.29×10^{-9}

Figure 5.33: *Temperature correction. The magnetic moment peak height (Nm/T) is plotted against the temperature measured (K) for the sample for that particular sweep rate. Quadratic functions are then fitted to the data sets for sweep rate. Interpolation is then possible between the measured temperature which fluctuates and the required temperature.*

Figure 5.33 above allows slight modification of the magnetic moment amplitude to take the value it would have had the sample been held at exactly the correct temperature while field sweeps were recorded.

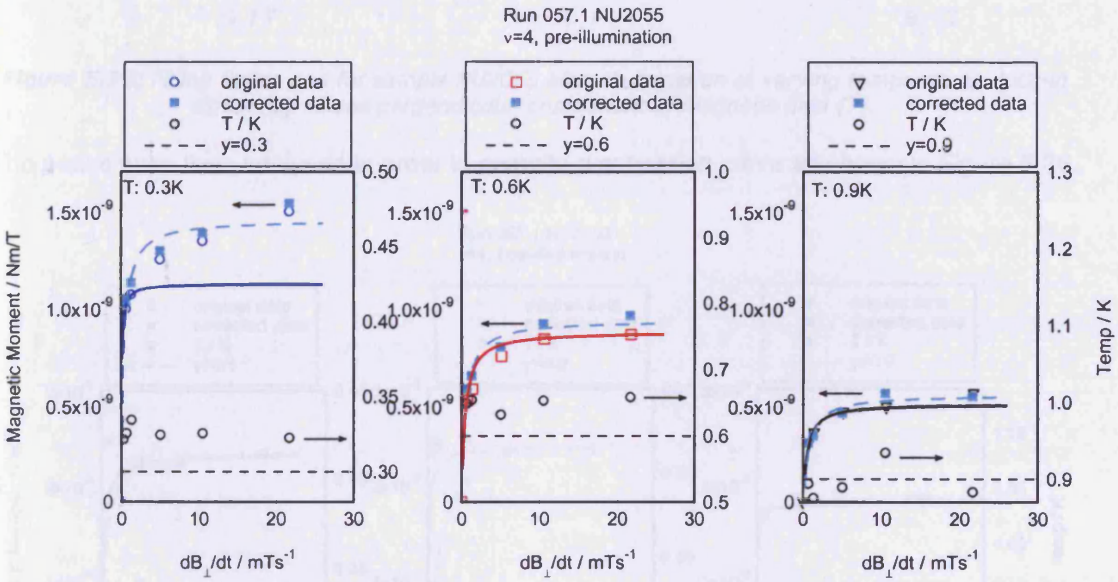

Figure 5.34: *Corrected-for-temperature magnetic moment amplitude (Nm/T) as a function of parallel sweep rate (mTs^{-1}) for NU2055 (ν=4) at v three temperatures before illumination. Original data is marked, as well as the corresponding temperature-corrected data which is shown in light blue. Two data fits are displayed on each graph, one is fitted to the original data set and the other to the corrected data set (colour-matched).*

The data points shown in Figure 5.34 above maintain the general behaviour observed for other samples.

- **Post-illumination data**

Having illuminated the sample the peak position for filling factor $\nu = 4$ shifted up in magnetic field from 3.1T to 4.2T. Figure 5.35 below shows the raw data traces of the peaks.

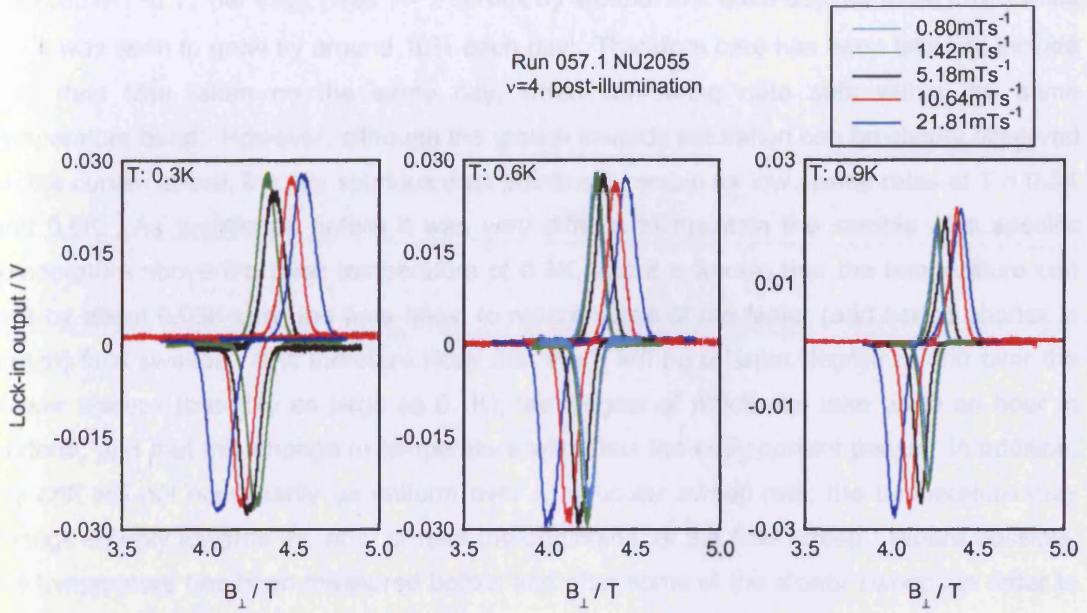

Figure 5.35: *Filling factor ν=4 for sample NU2055 after illumination at varying temperature: lock-in signal (V) versus perpendicular component of magnetic field (T).*

The peaks were then analysed in order to compile a saturation curve as shown in Figure 5.36.

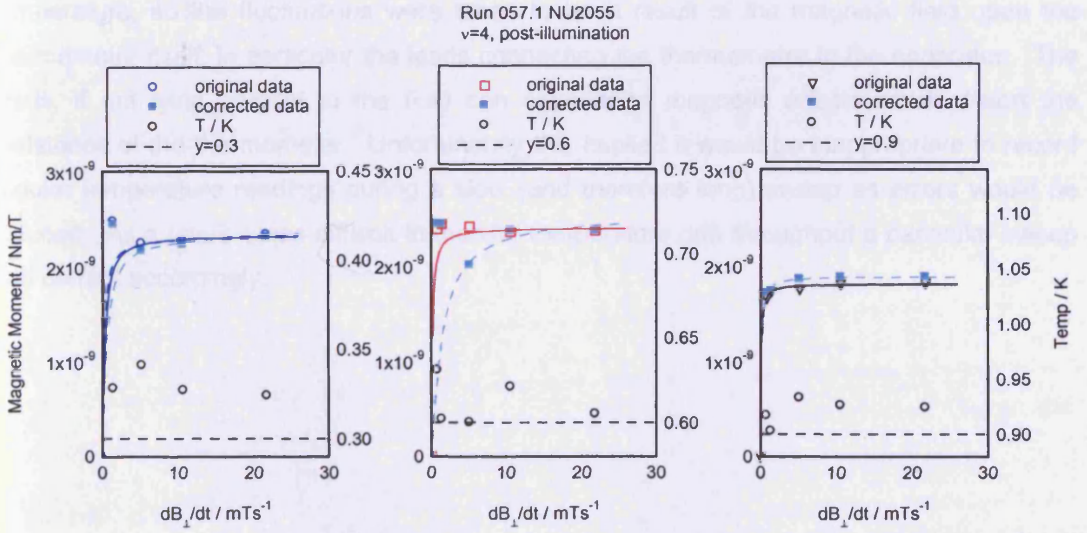

Figure 5.36: *Corrected-for-temperature magnetic moment amplitude (Nm/T) as a function of sweep rate (mTs^{-1}) for NU2055 (ν=4) at v three temperatures after illumination. Original data is marked as well as the corresponding temperature-corrected data which is shown in light blue. Two data fits are displayed on each graph for each data set.*

The peak growth with increasing sweep rate shown above in Figure 5.36 is as expected for higher values of sweep rate, but there are several spurious data points for lower sweep rate where the peak signal appears larger than anticipated. It was found that after illumination

there were slight changes in both peak height and field position from day to day. This was probably due to relaxation of the system as the sample warmed to around 10K overnight and the original illumination effects were not retained. Full field sweeps performed each day to ascertain any changes to the sample overnight showed a slight shift downwards in the peak field centre (~0.1T per day); peak $\nu = 2$ shrank by around 10% each day (for three days) while $\nu = 4$ was seen to grow by around 10% each day! Therefore care has been taken to include only data files taken on the same day, when comparing data sets within the same temperature band. However, although the growth towards saturation can be clearly observed on the curves above, the few spurious data points still remain for low sweep rates at T = 0.3K and 0.6K. As mentioned before it was very difficult to maintain the sample at a specific temperature above the base temperature of 0.3K, and it is known that the temperature can drift by about 0.05K over the time taken to record some of the faster (and hence shorter in length) field sweeps. It is therefore likely that there will be a larger degree of drift over the slower sweeps (possibly as large as 0.1K), the longest of which can take up to an hour to perform, and that this change in temperature will affect the eddy current peaks. In addition, the drift will not necessarily be uniform over a particular sweep rate; the temperature may change sharply towards the end, or near the beginning, of the field sweep. Where possible, the temperature has been measured before and after some of the slower sweeps in order to calculate an average value. Furthermore, it was noticed that the thermometers exhibited fluctuations in temperature (evident in the resistance value displayed) when the magnetic field was sweeping, and that when the sweep was paused several seconds elapsed before the value settled. The fluctuations were too substantial to indicate such a change in real temperature, so the fluctuations were taken to be a result of the magnetic field upon the thermometer itself, in particular the leads connecting the thermometer to the apparatus. The leads, if not lying parallel to the field can experience magnetic effects which distort the resistance of the thermometer. Unfortunately this implied it would be inappropriate to record regular temperature readings during a slow (and therefore long) sweep as errors would be induced. As a result it was difficult to monitor temperature drift throughout a particular sweep and correct accordingly.

5.4 References

[1]. P. R. Morris, PhD Thesis: *Torque magnetometry studies of the integer quantum Hall effect*, Cardiff University (1998).

Chapter 6: Breakdown of the Quantum Hall Effect

When the longitudinal current, I_x, in a 2DEG Hall bar increases to a critical value the longitudinal resistivity, ρ_{xx}, of the QHE changes abruptly by several orders of magnitude. The QHE is destroyed and this is known as breakdown. This result was first discovered by Ebert *et al*, [1] and published data is given in Figure 6.1. The inset shown within Figure 6.1 illustrates the Hall bar sample geometry employed to acquire such data which allows direct measurements of the longitudinal resistivity ρ_{xx}. In Hall bar measurements the current density is the variable parameter while the magnetic field is set at values close to a fully occupied Landau level. Ebert *et al* found that the high conductivity state associated to the quantum Hall effect is suddenly destroyed when the current density reaches a 'critical' value of around $0.56Am^{-1}$, with a corresponding electric field of around $100Vcm^{-1}$.

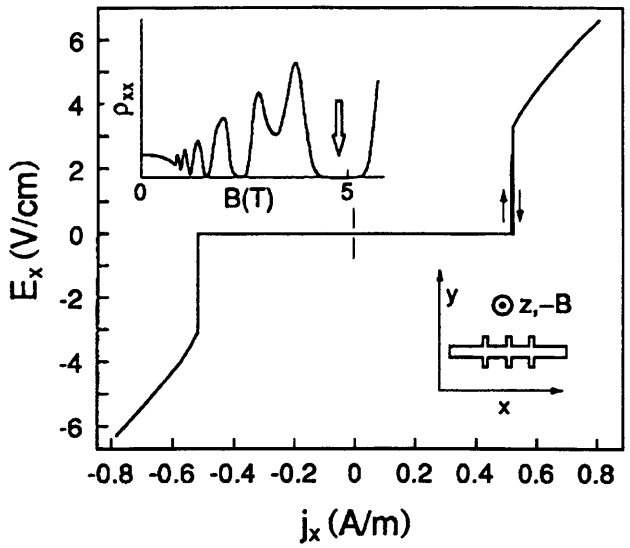

Figure 6.1: *Breakdown of the quantum Hall effect as studied by Ebert et al [1]. The graph shows experimental data from a AlGaAs/GaAs heterojunction sample where T=1.4K. The main graph plots the longitudinal electric field as a function of current density at the minimum in longitudinal resistivity at $\nu = 1$ (as shown in the inset). The IQHE is observed to breakdown at a critical current density of $0.56Am^{-1}$.*

In Cardiff, the technique of high sensitivity torque magnetometry is employed to record the deflection of a sample resulting from the eddy currents induced in the sample within a sweeping magnetic field, and this has the advantage that no contacts to the sample are necessary. In our measurements the magnetic field is the controlled parameter, rather than the driving electric current. As explained in Chapter 4, eddy currents are induced in the sample as the magnetic field sweeps through integer Landau level filling factors causing the sample to rotate on its suspension fibre. We observe two interesting effects in our experiments that are thought to be a form of breakdown. The first is the saturation of the magnetic moment peak size as the magnetic field sweep rate increases; the second is an unstable breakdown, demonstrated by a noisy signal output from the magnetometer. A

recently developed model for the magnetic moment saturation follows in this chapter and the noisy breakdown, found on the filling factor ν=2 peaks of samples A1157 and NU2055 (see sections 5.2 and 5.3), is discussed in chapter 7. First, a review of published models and data regarding breakdown is presented in section 6.1.

6.1 Models for breakdown

The correct model for the breakdown of the Quantum Hall Effect is difficult to assess due to varied debates concerning exact current distribution, effect of contacts and the precise shape of the Landau level structure. Three published models are outlined below.

6.1.1 Electron-heating instability

This theory of IQHE breakdown was first suggested by Ebert *et al* [1] in 1983 and occurs when the longitudinal electric field heats the electrons in the 2DEG. Instability in the electron temperature occurs at a critical electric field, and the temperature increases suddenly, due to the inability of the sample to fully remove the energy supplied to it. This leads to dramatic increase in ρ_{xx} and σ_{xx}, which depend on the electron temperature and not on that of the lattice. The critical current density was found to be ~0.56Am^{-1}, with an electric field of ~10^4 Vm^{-1}.

Ebert *et al* first proposed that the rate of energy gain of the electrons in the 2DEG exceeds the rate of energy loss, resulting in a sharp rise in temperature. By plotting the rate of energy loss and longitudinal conductivity as functions of electron temperature, it was possible to discern critical values of electron temperature at which breakdown occurred. These electron temperatures were generally seen to take values that were about 1.4K higher than the lattice temperatures. The rate of energy gain was approximately equal to the rate of energy loss at these critical temperatures.

Komiyama *et al* [2] extended this with work of their own, and while using an electron heating mechanism, also suggested that by plotting a derived energy balance equation the electric field and the electron temperature as a function of lattice temperature would be revealed. The results of these calculations showed that there was indeed an acute rise in electron temperature as the longitudinal electric field neared its critical value. It was shown that for a range of longitudinal electric field values centred about the critical value there were actually three permitted values for electron temperature for a given lattice temperature. This led to an S-shaped relation between the longitudinal conductivity and electric field. The central temperature was found to be very unstable, thus it was suggested that the S-shaped characteristic is not actually observed experimentally because the 2DEG decomposes into regions that are characterised by either the higher or lower electron temperature. The data acquired theoretically was excellently matched with that gained experimentally, giving

estimated values of critical electric field of the order of 5000 Vm^{-1}, corresponding to a critical current density of 1 Am^{-1}.

6.1.2 Intra-Landau Level Transitions

The Cerenkov effect describes the way in which charged particles will emit photons if they move through a medium at a speed greater than the speed of light in that medium. Strêda and von Klitzing [3] proposed that, equivalently, if electrons move through crossed electric and magnetic fields at a drift velocity close to the speed of sound in gallium arsenide, they will emit acoustical phonons. Their edge-state model maintains that the phonon system accepts energy from the electrons in the 2DEG. As a consequence the phonon system experiences an energetic excitation equal to that lost by the electron system. This triggers a transfer of electrons from one edge of the sample to the other opposite side, which emit acoustic phonons as they traverse. For such an energy transfer to occur, it was calculated that the drift velocity of the electrons would be required to exceed that of the acoustic phonons in the same medium. This experimental data tallied with this proposal, showing that a drift velocity of 1500ms^{-1} for electrons at the critical current density was comparable with the lowest speed of sound in GaAs (2470ms^{-1}). Although this theory claimed to qualitatively explain all available data, no predictions for critical current densities were stated.

6.1.3 Inter-Landau Level Transitions

Tsui *et al* [4] proposed that Zener tunnelling of electrons might be responsible for the breakdown of the IQHE. This process involves the tunnelling of electrons from the Fermi level across the energy gap to the lowest empty Landau level. Tsui *et al* implied that when the longitudinal electric field is large enough an electron can gain an energy equal to the energy gap by travelling a distance equal to the cyclotron radii of the two Landau levels adjacent to the Fermi level. When the electron gains this amount of energy it can tunnel across the energy gap. A critical current density of the order of 60Am^{-1} was predicted in GaAs at 10 Tesla.

Heinonen *et al* [5] proposed a theory involving inter-Landau level transitions and phonon emission. In their simple model phonon-assisted transitions between the lowest two Landau levels were responsible for the breakdown of the IQHE. Transition rate equations estimate the power dissipated in the sample. The resulting form of longitudinal voltage as a function of current density was found to be in excellent qualitative agreement with experimental data, in that the onset of dissipation was seen to start dramatically, growing exponentially as $\exp\left(-B/(v_d - v_s)^2\right)$ where B is the magnetic field, v_d the electron drift velocity and v_s the velocity of sound. A critical current density of the order of 5Am^{-1} was predicted for a field of 5.5 Tesla (filling factor ν=1).

Eaves and Sheard [6] have since derived a quasi-elastic inter-Landau level scattering (QUILLS) model. This model was developed to describe the experimental observations of Bliek *et al* [7], where a Hall bar geometry sample with constrictions of width of the order 1μm was investigated. Critical current densities were found to be of the order of $30Am^{-1}$, considerably larger than those of Ebert *et al* [1] and Cage *et al* [8]. Eaves and Sheard claimed that the solution of the one-electron Schrödinger equation in crossed electric and magnetic fields provides understanding of these results. With this solution, and assuming that the onset of QUILLS is responsible for breakdown, it was concluded that the critical electric fields and current densities could be given by,

$$E_c = \frac{\hbar\omega_c}{el_B\left((2n+1)^{\frac{1}{2}} + (2n+3)^{\frac{1}{2}}\right)}, \tag{6.1}$$

and

$$j_c = \frac{\nu e^2 E_c}{h} \tag{6.2}$$

where $\omega_c = \frac{eB}{m^*}$ is the cyclotron frequency, $l_B = \left(\frac{\hbar}{eB}\right)^{\frac{1}{2}}$ is the magnetic length, n is the Landau level index (which takes account of spin states) and υ is the Landau level filling factor. A requirement of these equations is that of the spatial overlap between a wavefunction of the highest filled Landau level and an empty state of the next level. In this way Eaves and Sheard calculated critical current density values of $29Am^{-1}$ and $14Am^{-1}$ for ν=2 and ν=4 respectively. These were within 10% of the values measured by Bliek *et al* [7].

More recently, Guven *et al* [9] combined a hot electron model with the QUILLS model in order to explain the breakdown of the IQHE.

6.2 Sweep-rate dependence of magnetic moment peak saturation

It was shown in Chapter 5 that the eddy current peak grows in height (and width) as the magnetic field sweep rate increases. The behaviour of the peak with respect to sweep rate has been investigated previously at Cardiff [10], and the simple model subsequently used to describe experimental data is outlined below. Breakdown was not investigated until more recently, so this model does not explain such effects. As such it will be seen that the model, although useful at the time, is limited when compared with later data, in which it is believed breakdown plays an important role.

6.2.1 Classical Model

Here we discuss a classical model [10] which describes the change in magnetic moment peak size of an induced eddy current in a sweeping magnetic field. A bulk model is assumed regarding the current distribution within the sample.

Consider a 2DEG sample of annular form, with inner radius r_1 and outer radius r_2. We assume the longitudinal resistivity of the 2DEG in the quantum Hall regime tends to zero and that the resistivity is constant for a set temperature for filling factor ν. A sweeping magnetic field is applied in the direction perpendicular to the plane of the annulus.

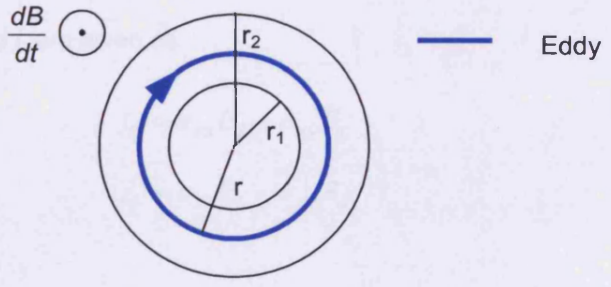

Figure 6.2: *2 DEG annulus*

The sweeping magnetic field induces an emf, ε, in the 2DEG, which can be expressed as

$$\varepsilon = -\frac{d\Phi}{dt} \tag{6.3}$$

where $\frac{d\Phi}{dt}$ is the rate of change of magnetic flux.

When a magnetic field, B, pierces the plane of a circuit of area A, the magnetic flux penetrating that circuit is given by

$$\Phi = BA = B\pi r^2 . \tag{6.4}$$

By substituting Equation 6.4 into Equation 6.3, we can rewrite the induced emf, ε_ϕ, around the closed path, *l*, of the annulus as

$$\varepsilon_\phi = -\frac{d\Phi}{dt} = -\pi r^2 \frac{dB}{dt}. \tag{6.5}$$

By integrating the internal electric field E_ϕ at *r* around the same closed path we can form another relationship for ε_ϕ written as

$$\begin{aligned} \varepsilon_\phi &= \oint_l \underline{E}_\phi \cdot d\underline{l} \\ &= \int_0^{2\pi} E_\phi r d\theta \\ &= 2\pi E_\phi r. \end{aligned} \tag{6.6}$$

By combining Equations 6.5 and 6.6, an equation for E_ϕ emerges:

$$E_\phi = -\frac{r}{2}\frac{dB}{dt}. \tag{6.7}$$

The current densities j_ϕ and j_r are given as

$$\begin{aligned} j_r &= \sigma_{xx} E_\phi + \sigma_{xy} E_r \\ j_\phi &= \sigma_{xx} E_r - \sigma_{xy} E_\phi \end{aligned}. \tag{6.8}$$

Now

$$\begin{aligned} \rho_{xy} &= \frac{\sigma_{xy}}{\sigma_{xx}^2 + \sigma_{xy}^2} \simeq \frac{1}{\sigma_{xy}} \\ \rho_{xx} &= \frac{\sigma_{xx}}{\sigma_{xx}^2 + \sigma_{xy}^2} \simeq \frac{\sigma_{xx}}{\sigma_{xy}^2} \end{aligned} \tag{6.9}$$

where $\sigma_{xy} >> \sigma_{xx}$ in the quantum Hall effect regime. In the steady state, $j_r = 0$, so

$$E_r = \frac{\sigma_{xx}}{\sigma_{xy}} E_\phi, \tag{6.10}$$

so, when $\sigma_{xx} < \sigma_{xy}$, the azimuthal current density is given by

$$j_\phi \simeq \frac{\sigma_{xy}^{\ 2}}{\sigma_{xx}} E_\phi = \frac{E\phi}{\rho_{xx}}. \tag{6.11}$$

On substitution of Equation 6.7, Equation 6.11 becomes

$$j_\phi = -\frac{1}{2\rho_{xx}} \frac{dB}{dt} r. \tag{6.12}$$

We can convert current density into a current element dI_ϕ, using $dI_\phi = j_\phi dr$ which gives

$$dI_\phi = -\frac{1}{2\rho_{xx}} \frac{dB}{dt} r dr. \tag{6.13}$$

The magnetic moment, m, in a current-carrying loop is given by $m = AI$. Therefore, an element of magnetic moment dm can be written as

$$dm = \pi r^2 dI_\phi. \tag{6.14}$$

On substitution of Equation 6.13, Equation 6.14 becomes

$$dm = -\frac{\pi}{2\rho_{xx}} \frac{dB}{dt} r^3 dr. \tag{6.15}$$

This expression can be integrated between r_1 and r_2, as given in Figure 6.2, to calculate the total magnetic moment:

$$m = \int_{r_1}^{r_2} -\frac{\pi}{2\rho_{xx}} \frac{dB}{dt} r^3 dr = -\frac{\pi}{8\rho_{xx}} \frac{dB}{dt} \left(r_2^{\ 4} - r_1^{\ 4} \right). \tag{6.16}$$

It can be seen in this model that the total magnetic moment has a linear dependence on $\frac{dB}{dt}$, the magnetic field sweep rate. Experimental data was found to generally agree with this model, and was especially true for lower magnetic field sweep rates. However it can be seen that this early data exhibits a deviation from the linear fit at higher sweep rates [10], in both positive and negative sweep directions.

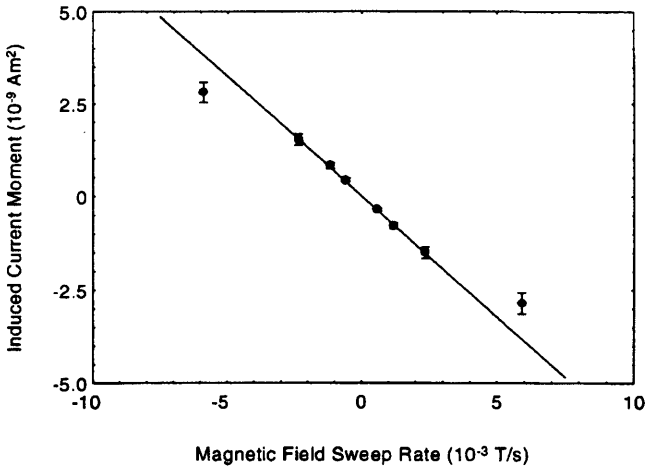

Figure 6.3: *Magnetic moment peak height as a function of sweep rate [10]. It can be seen that for low sweep rates, the magnetic moment follows a linear dependence on sweep rate, but at the higher sweep rates the peak signal deviates from this dependence. This deviation was attributed to breakdown.*

More recent experiments performed in Cardiff over a wider range of sweep rates do not now justify this dependence, revealing far clearer evidence of the deviation at higher sweep rates. Also, previous work performed in conjunction with Exeter on a separate system offering higher sweep rates [11] has also found that the magnetic moment peak size grows with increasing sweep rate but reaches an upper limit and saturates (for an example of such behaviour refer to Figure 5.10). It is believed that this saturation is a manifestation of breakdown. In some way, a breakdown mechanism limits the development of the peak, inhibiting the growth expected as sweep rate increases.

6.2.2 Current Distribution in a 2DEG

When a magnetic field is applied to the moving electrons of a 2DEG system, charge accumulates at the edges of the sample, producing the Hall field E_y. This field will not be uniform in the 2DEG due to the presence of these edge charges.

Consider a very long Hall bar. When a current I_{xx} is passed down the length of the bar, the charges gather in a narrow edge region, within a width of the order of a magnetic length of the sample edge. The magnetic length is given by $l_B \equiv \left(\frac{\hbar}{eB}\right)^{\frac{1}{2}}$. Assuming that the Hall bar is very long, the accumulated charges are considered to be linearly distributed at the opposite edges. The relationship between the Hall field E_y and the distance along the sample width y is given by [12, 13]

$$E_y = \frac{\lambda}{2\pi\varepsilon}\left(\frac{1}{y}+\frac{1}{d-y}\right) \tag{6.17}$$

where λ is the linear charge density, ε is the permittivity and d is the width of the Hall bar. This relationship is a classical derivation of field based on two lines of parallel charge. The

electric field at the edge is clearly much greater than that at the centre of the Hall bar. If, at some point in the 2DEG, the electric (E_y) and magnetic (B_z) forces equal each other then,

$$eE_y = ev_d B_z \tag{6.18}$$

here v_d is the electron drift velocity, which can also be expressed as

$$v_d = \frac{j_x(y)}{en_{2D}} \tag{6.19}$$

where $j_x(y)$ is the current density in the Hall bar and n_{2D} is the electron density. By substituting Equations 6.17 and 6.18 into Equation 6.19, we obtain the current density as

$$j_x(y) = \frac{en_{2D}E_y}{B_z} = \frac{en_{2D}\lambda}{2\pi\varepsilon_0 B_z}\left(\frac{1}{y} + \frac{1}{d-y}\right). \tag{6.20}$$

A schematic of the function given in Equation 6.20 is plotted below in Figure 6.4. It can be seen that that the edge current is much larger than that in the bulk of a 2DEG system.

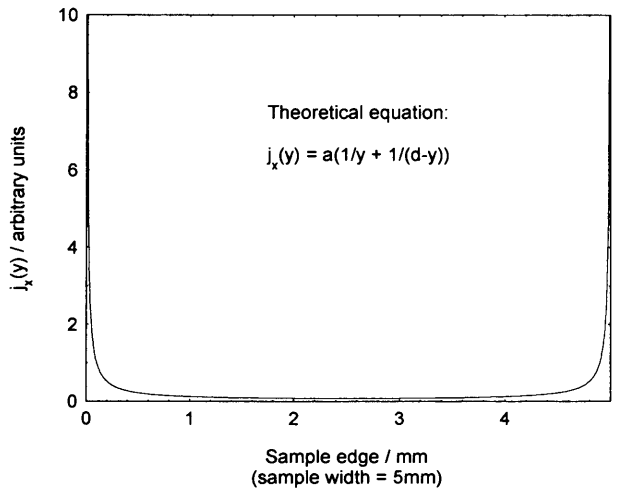

Figure 6.4: *Graph showing magnitude of induced eddy current flow across a 2DEG sample (a=0.1) [12].*

McDonald *et al* [13] derived equations which described the charge, current and Hall voltage distributions in a 2DEG, and showed that these distributions were distinctly edge-weighted.

6.3 The current charge and discharge at sample edge model

This semi-classical model has been developed [14] to explain the eddy current peak saturation behaviour observed on increasing the magnetic field sweep rate. Consider a 2DEG sample in which the induced eddy current flow j_x parallel to the edge is concentrated near to the edge, and supported by a Hall field E_y, as displayed in Figure 6.5 below.

The charge/discharge current density can be written as

$$j_y = -Cw\dot{E}_y \tag{6.21}$$

where C is the capacitance per unit length of the edge. The effective width w of the capacitance is the distance over which the Hall field is mostly dropped.

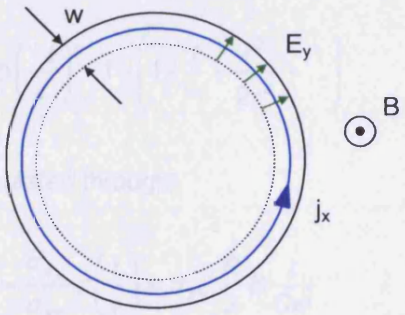

Figure 6.5: *Schematic showing induced eddy currents circulating near the edge of the sample within a width w, and supported by a perpendicular electric field E_y. The applied magnetic has a direction coming out of the page.*

6.3.1 Charge-up

We begin with Ohm's law:

$$\begin{pmatrix} j_x \\ j_y \end{pmatrix} = \begin{pmatrix} \sigma_{xx} & \sigma_{xy} \\ -\sigma_{xy} & \sigma_{yy} \end{pmatrix} \begin{pmatrix} E_x \\ E_y \end{pmatrix} \tag{6.22}$$

and, starting with zero edge charge, sweep the magnetic field to an eddy current peak. At this point $E_x = \varepsilon$ say, where ε, the emf induced by the sweeping magnetic field, is related to the sample radius R and the sweep rate $\dot{B}$ approximately as

$$\varepsilon \approx -\frac{R}{2}\dot{B}. \tag{6.23}$$

Typical values of ε lie in the range 1 - 80μVm^{-1} for our samples and sweep rates. Substituting Equations 6.21 and 6.23 and $E_x = \varepsilon$ into Ohm's law gives

$$j_x = \sigma_{xx}\varepsilon + \sigma_{xy}E_y$$
$$j_y = -Cw\dot{E}_y = -\sigma_{xy}\varepsilon + \sigma_{xx}E_y \tag{6.24}$$

The equation for E_y has a solution of the form

$$E_y = \frac{\sigma_{xy}}{\sigma_{xx}}\varepsilon\left(1-\exp\left(-t/\tau\right)\right), \tag{6.25}$$

where the decay time constant is

$$\tau = \frac{Cw}{\sigma_{xx}}. \tag{6.26}$$

Expanding the exponential function in Equation 6.25 as

$$1-\exp\left(\frac{-t}{\tau}\right) = 1-\left(1-\frac{t}{\tau}+\frac{t^2}{2\tau^2}-\ldots\right) \tag{6.27}$$

allows an estimate of E_y to be calculated through

$$E_y = \frac{\sigma_{xy}}{\sigma_{xx}}\varepsilon\left(\frac{t}{\tau}\right) = \sigma_{xy}\frac{R}{2}\dot{B}\frac{t}{Cw} \tag{6.28}$$

when the time constant τ is large, and if the product Cw were known. From Equation 6.24

$$j_x \approx \frac{\sigma_{xy}^{\ 2}}{\sigma_{xx}}\varepsilon\left(1-\exp\left(-t/\tau\right)\right). \tag{6.29}$$

It can be seen that if σ_{xx} is sufficiently small, or ε sufficiently large, j_x will increase and could reach breakdown. The main approximation in this charge-up model is neglecting the time dependence of σ_{xx} during the field sweep in integrating Equation 6.24.

Takaoka *et al* [15] measured the capacitance of a GaAs/AlGaAs heterostructure in the quantum Hall regime as a function of magnetic field, and estimated the widths of the current channels. Typical values presented which could be considered appropriate for our measurements gave a capacitance and channel width of ~2pF and ~1μm respectively. Consequently, a huge electric field E_y of around $10^7 Vm^{-1}$ is estimated from the charge-up model (Equation 6.28), corresponding to a critical current density of ~$10^3 Am^{-1}$ (Equation 6.29). The value of E_y calculated via the charge-up model is discussed further with respect to the experimentally obtained eddy current peak size in section 6.5.7.

Assuming σ_{xx} is small and constant over a field width ΔB, it is possible to estimate the maximum peak height as a function of sweep rate. The time Δt taken to sweep to the centre of the eddy current peak is $\Delta B/2\dot{B}$; substituting this into Equation 6.24 gives

$$j_x^{peak} \approx \frac{\sigma_{xy}^2}{\sigma_{xx}} \varepsilon\left(1-\exp\left(-\Delta B/2\dot{B}\tau\right)\right)$$
$$j_x^{peak} \approx \frac{\sigma_{xy}^2}{\sigma_{xx}} \frac{R}{2} \frac{\Delta B}{\tau} X\left(1-\exp\left(-1/X\right)\right) \tag{6.30}$$

where $X = 2\dot{B}\tau/\Delta B$, a dimensionless variable. Figure 6.6 is a normalised plot of the eddy current peak height versus X, and has the form observed experimentally.

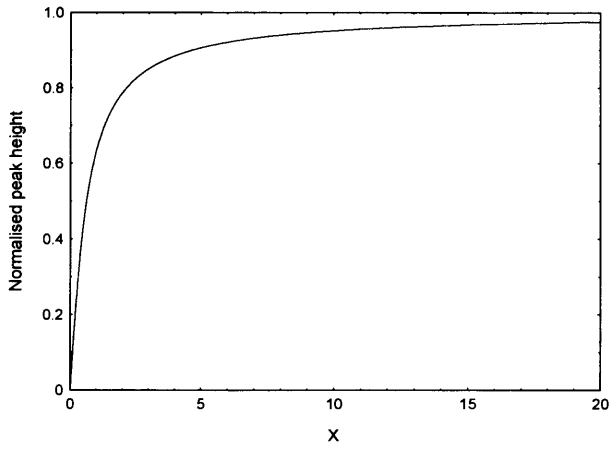

Figure 6.6: *The function X(1 - exp(-1/X))*

If the current is flowing in a width w near to the sample edge, then the associated magnetic moment peak m is expressed as $m^{peak} \approx j_x^{peak} w\pi R^2$, or

$$m^{peak} \approx \frac{\sigma_{xy}^2}{\sigma_{xx}} \frac{\pi}{2} wR^3\dot{B}\left(1-\exp\left(-\Delta B/2\dot{B}\tau\right)\right) \tag{6.31}$$

Experimental data can be fitted with an exponential function of the form

$$m^{peak} \approx a\dot{B}\left(1-\exp\left(-b/\dot{B}\right)\right) \tag{6.32}$$

where

$$a = \frac{\sigma_{xy}^2}{\sigma_{xx}} \frac{\pi}{2} wR^3 \text{ and } b = \frac{\Delta B}{2\tau} = \frac{\Delta B}{2Cw} \sigma_{xx}. \tag{6.33}$$

From the fitting parameters *a* and *b* it is possible to extract the time constant τ, and longitudinal conductivity σ_{xx}, which also leads to an estimate of the resistivity $\rho_{xx} \approx \sigma_{xx}/\sigma_{xy}^2$. If ρ_{xx} were known independently (from Hall bar measurements), a measure of the effective width *w* would be known.

The product *ab* gives the value of magnetic moment at which the peak saturates, m^{sat}, at higher sweep rates. In order to acquire an accurate estimate of the error in *ab* it is useful to alter the fitting function given in Equation 6.32 to

$$m^{peak} \approx \frac{m^{sat}}{b}\dot{B}\left(1-\exp\left(-b/\dot{B}\right)\right) \tag{6.34}$$

where $m^{sat} = ab$. In this way an error for the saturation value m^{sat} can be calculated independently, rather than combining the separate errors of *a* and *b* themselves.

It is thought that the conductivity σ_{xx} is strongly dependent on temperature [2], whereas the peak width ΔB has a much weaker temperature dependence [16]. It is therefore expected that *a* and *b* should demonstrate opposite temperature dependences.

6.3.2 Decay

Now consider the case where the magnetic field has been swept to an eddy current peak and then paused. Now $E_x = 0$ and the edge has an initial charge. Ohm's law now becomes

$$\begin{aligned} j_x &= \sigma_{xy}E_y \\ j_y &= -Cw\dot{E}_y = \sigma_{xx}E_y \end{aligned} \tag{6.35}$$

The equation for E_y has a solution

$$E_y = E_y(0)\exp(-t/\tau), \tag{6.36}$$

where the decay time constant is the same as previously $\tau = \frac{Cw}{\sigma_{xx}}$, and from Equation 6.35

$$j_x = j_x(0)\exp(-t/\tau). \tag{6.37}$$

Therefore, when the magnetic field is swept to an eddy current peak and paused, the eddy current signal can be expected to die off exponentially with a decay time constant τ.

6.4 Saturation of magnetic moment peak data

Having developed a model to describe the charge built up at the sample edge as the magnetic field is swept, it is now necessary to compare this model with experimental data. The charge up model is considered first. A raw data signal (in volts) is converted to magnetic moment (Nm/T) as outlined in section 5.1.1, and the amplitude of the peak is extracted and plotted with respect to sweep rate. These plots have already been displayed through Chapter 5 but will now be revisited and treated with respect to the above model. Again each sample will be dealt with in turn.

6.4.1 Sample T231

Measurements taken for sample T231 provide data for two filling factors ν = 1, 2 at several sample temperatures. The peak amplitude for magnetic moment (for filling factor 1) is corrected for temperature drift and then plotted against sweep rate as displayed below in Figure 6.7.

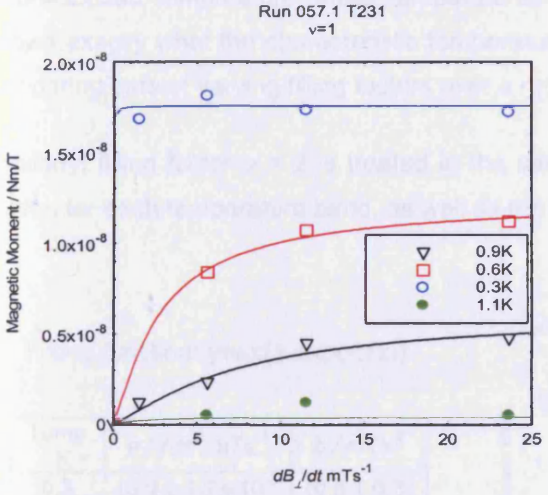

Fitting function: y=ax(1-exp(-b/x))

Temp / K	a / Am^2/mTs^{-1}	b / mTs^{-1}
0.3	$(1.5 \pm 1.5)\times10^{-7}$	(0.1 ± 0.1)
0.6	$(2.7 \pm 0.4)\times10^{-9}$	(4.7 ± 0.8)
0.9	$(5.8 \pm 1.3)\times10^{-10}$	(11 ± 3.5)
1.1	$(2.9 \pm 230)\times10^{-10}$	(1.3 ± 11)

Figure 6.7: *Saturation curves at filling factor ν = 1; the table displays the fitting parameters of the solid curves seen in the graph. Parameter a has units Am^2 for magnetic moment, whereas the graph shows magnetic moment units as Nm/T; this is to clarify how the magnetic moment value is obtained from raw data, in that the lock-in voltage is first converted to torque (Nm) and then divided by field (T) to arrive at magnetic moment (Nm/T). The two sets of units are then equivalent, and Am^2, in fundamental units, is chosen over Nm/T.*

At the lowest temperature the peak height appears to have saturated for all sweep rates, whereas more growth is observed as the sweep rate increases for higher temperatures. The data is then fitted according to the charge-up model above, as given by Equation 6.32 and parameter a is calculated through $m^{sat} = ab$. The fitting parameters a and b are presented in the table of Figure 6.7; the value for m^{sat} and its error will be used in analysis in section 6.5.2. Having extracted these fitting parameters, they are plotted against temperature as presented in Figure 6.8.

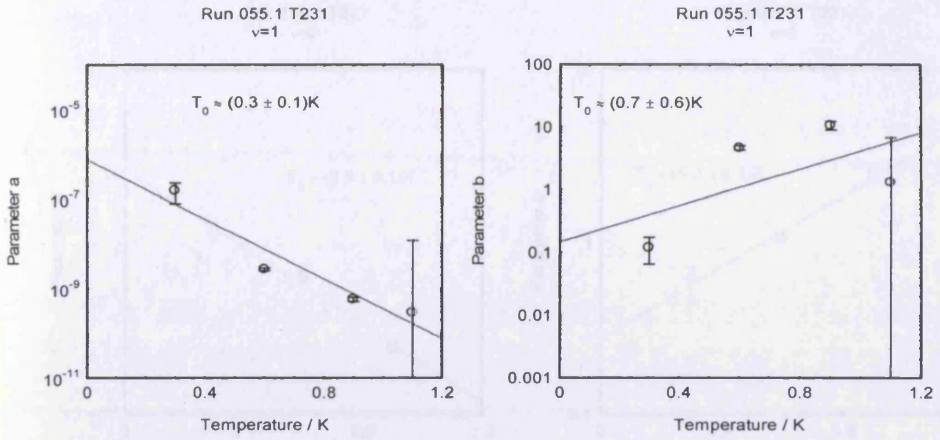

Figure 6.8: *The parameters a and b plotted against temperature (K). The values of a and b are shown on a logarithmic scale. Some of the error bars are seen to be rather large; this is due to the size of the error crossing the y=0 point. When plotted on a log scale the full range of error cannot be displayed since the y-axis approaches zero without actually reaching it, hence the error is seen to extend to infinity on this scale.*

It can be seen that parameters *a* and *b* have opposite temperature dependence. By plotting them on a logarithmic scale it is possible to fit straight lines to the data points and extract a 'characteristic' temperature; these temperatures are also shown within Figure 6.8. It is not known exactly what the characteristic temperature value represents, but it is a useful way of comparing data of varying filling factors over a range of samples.

Similarly, filling factor ν = 2 is treated in the same way. Figure 6.9 displays the saturation curves for each temperature band, as well as the fitted functions and associated parameters.

Fitting function: y=ax(1-exp(-b/x))

Temp / K	*a* / Am^2/mTs^{-1}	*b* / mTs^{-1}
0.3	$(3.9 \pm 1.7)\times10^{-8}$	(0.6 ± 0.3)
0.6	$(1.6 \pm \ldots)\times10^{-8}$	$(1.0 \pm \ldots)$
0.9	$(3.8 \pm 0.7)\times10^{-9}$	(2.5 ± 0.5)

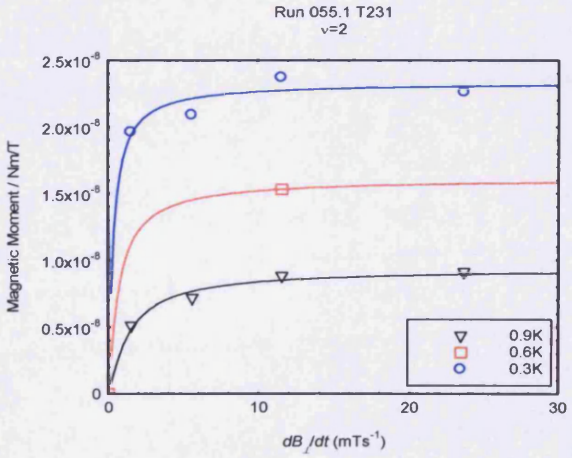

Figure 6.9: *Saturation curves at filling factor ν = 2; the table displays the fitting parameters of the solid curves seen in the graph.*

The fitted values of *a* and *b* for 0.6K were found to have meaningless zero error values; this is due to the use of a two-parameter fitting function performed on only two data points (the visible point in red, and the origin). Figure 6.10 shows the parameters *a* and *b* plotted against temperature.

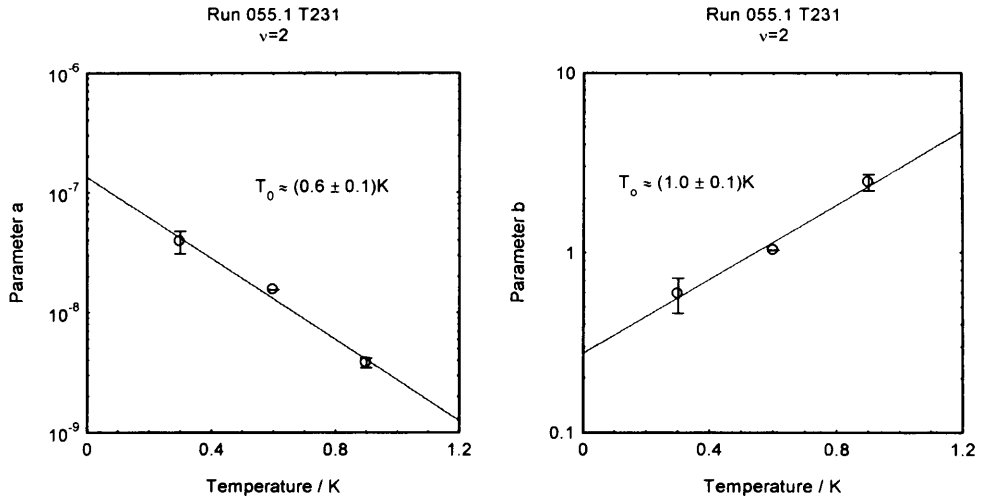

Figure 6.10: *The parameters a (Am^2/mTs^{-1}) and b (mTs^{-1}) plotted against temperature (K) for T231, ν=2. The values of a and b are shown on a logarithmic scale.*

The fits shown in Figure 6.10 appear to correlate far better than those shown for ν=1 in Figure 6.8, with the straight line fits falling well within the error bars for parameters *a* and *b*. Again, the fitting parameters are shown to have opposite temperature dependence, with parameter *a* falling as temperature increases, while parameter *b* grows.

6.4.2 Sample A1157

Measurements taken for sample A1157 in run 056.1 provide data for two filling factors ν = 2, 4 at several sample temperatures. The peak amplitude for magnetic moment for filling factor 2 is corrected for temperature drift and then plotted against sweep rate as displayed below in Figure 6.11.

Fitting function: y=ax(1-exp(-b/x))

Temp / K	a / Am^2/mTs^{-1}	b / mTs^{-1}
0.3	$(1.3 \pm 380)\times10^{-5}$	$(5.6 \pm 1700)\times10^{-4}$
0.6	$(3.7 \pm 120)\times10^{-7}$	(0.02 ± 0.6)
0.9	$(9.5 \pm 60)\times10^{-8}$	(0.08 ± 0.5)
1.1	$(2.8 \pm 0.3)\times10^{-8}$	(0.2 ± 0.02)

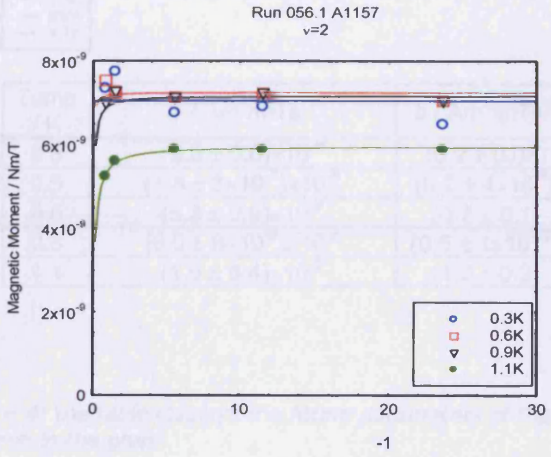

Figure 6.11: *Saturation curves at filling factor ν = 2; the table displays the fitting parameters of the solid curves seen in the graph.*

The eddy current peaks seem to have reached saturation at all temperatures below around 1K. Growth of the peak amplitude towards saturation is only really visible for data taken at 1.1K. The large errors in parameters *a* and *b* can be attributed to the increased number of possible fitting solutions at lower temperatures where saturation has been reached; for T=1.1K the growth of peak height with sweep rate restricts the fitting procedure and reduces the errors induced. The large errors suggest the data is not meaningful and it is not considered useful to analyse the parameters *a* and *b* further.

Eddy current peak data was also collected for filling factor ν=4 with sample A1157. The saturation curves at differing temperatures are displayed in figure 6.12.

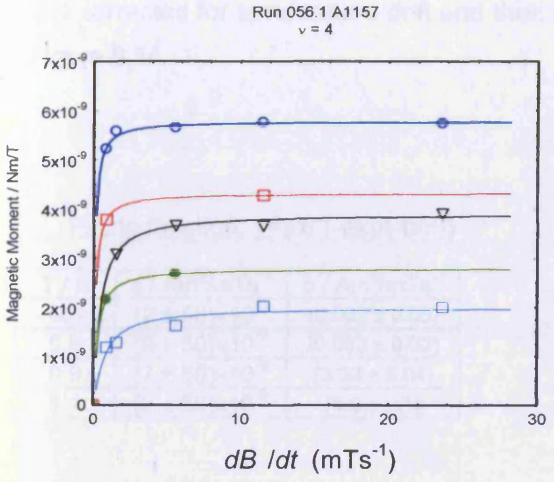

Fitting function: $y=ax(1-\exp(-b/x))$

Temp / K	a / Am^2/mTs^{-1}	b / Am^2/mTs^{-1}
0.3	$(3.5 \pm 0.6)\times10^{-8}$	(0.2 ± 0.03)
0.5	$(1.8 \pm 3\times10^{-7})\times10^{-8}$	$(0.2 \pm 4\times10^{-8})$
0.6	$(5.3 \pm 0.9)\times10^{-8}$	(0.7 ± 0.1)
0.8	$(6.0 \pm 8\times10^{-9})\times10^{-8}$	$(0.5 \pm 1\times10^{-10})$
1.1	$(1.6 \pm 0.4)\times10^{-8}$	(1.2 ± 0.3)

Figure 6.12: *Saturation curves at filling factor ν = 4; the table displays the fitting parameters of the solid curves seen in the graph.*

The use of the exponential fitting function correlates well to the data which exhibits clear growth towards saturation as the sweep rate increases. Values of *a* and *b* found by fitting to data at 0.5K and 0.8K are seen to have very small errors. This is due to their only being three points for each data set so when a two-parameter fitting function is used it is likely that a function will be found that closely fits the given data, with little error yielded. The extracted fitting parameters tabulated in figure 6.12 are plotted against temperature in the graphs of figure 6.13.

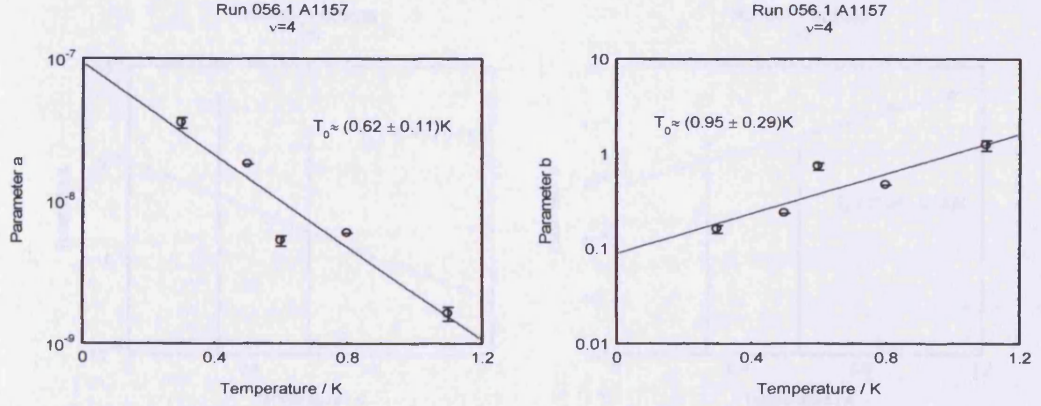

Figure 6.13: *The parameters a and b plotted against temperature (K) for A1157, ν=4. The values of a and b are shown on a logarithmic scale.*

6.4.3 Sample NU2055

Measurements taken for sample NU2055 in run 057.1 provide data for two filling factors $\nu = 2$, 4 at several sample temperatures. The peak amplitude for magnetic moment for filling factor 2 is corrected for temperature drift and then plotted against sweep rate as displayed below in Figure 6.14.

Fitting function: y=ax(1-exp(-b/x))

T / K	a / Am^2/mTs^{-1}	b / Am^2/mTs^{-1}
0.3	$(2 \pm 50)\times10^{-6}$	(0.002 ± 0.05)
0.6	$(9 \pm 50)\times10^{-7}$	(0.003 ± 0.02)
0.9	$(7 \pm 50)\times10^{-9}$	(0.33 ± 0.04)
1.1	$(2 \pm 50)\times10^{-9}$	(1.0 ± 0.1)

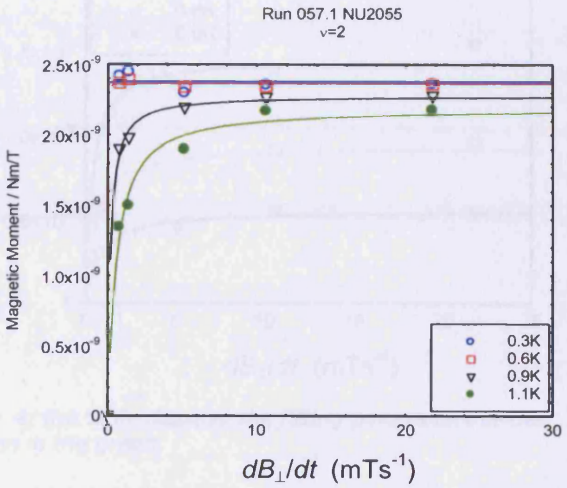

Figure 6.14: *Saturation curves at filling factor $\nu = 2$; the table displays the fitting parameters of the solid curves seen in the graph.*

Peak height growth as a function of sweep rate is visible for the two data sets at higher temperatures of 0.9K and 1.1K; at 0.3K and 0.6K the peak height appears to saturate early for lower sweep rates, hence large error values. The values for parameters *a* and *b* are then plotted as a function of temperature as shown in Figure 6.15; a weighted linear fit is plotted for the displayed data.

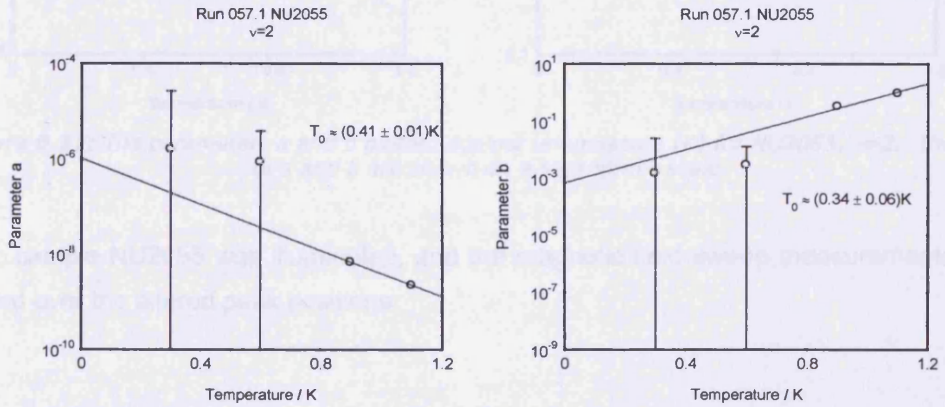

Figure 6.15: *The parameters a and b plotted against temperature (K) for NU2055, ν=2. The values of a and b are shown on a logarithmic scale.*

Similarly, the saturation curves attained from data for filling factor $\nu = 4$ are shown in figure 6.16 below. Then, the parameters *a* and *b* are extracted and plotted against temperature in Figure 6.17.

Fitting function: y=ax(1-exp(-b/x))

	a / Am^2/mTs^{-1}	b / mTs^{-1}
0.3	$(2.2 \pm 0.4)\times10^{-9}$	(0.7 ± 0.1)
0.6	$(9.6 \pm 1.4)\times10^{-10}$	(1.0 ± 0.2)
0.9	$(4.2 \pm 0.7\times10^{-10}$	(1.4 ± 0.2)

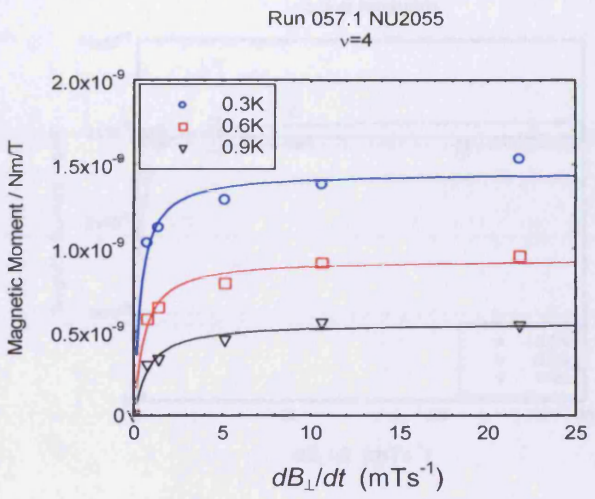

Figure 6.16: *Saturation curves at filling factor $\nu = 4$; the table displays the fitting parameters of the solid curves seen in the graph.*

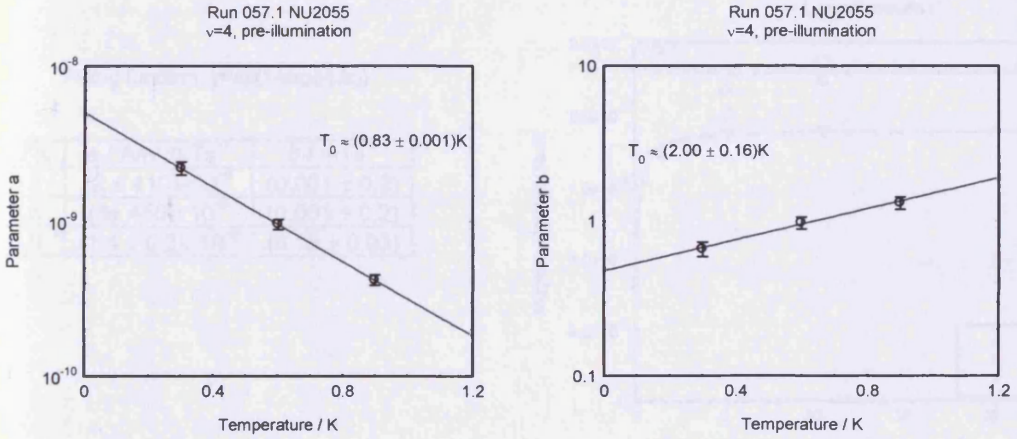

Figure 6.17: *The parameters a and b plotted against temperature (K) for NU2055, ν=2. The values of a and b are shown on a logarithmic scale.*

Finally, sample NU2055 was illuminated, and the magnetic field sweep measurements were repeated over the altered peak positions.

Figures 6.18 and 6.19 display saturation data for filling factor $\nu = 2$ and $\nu = 4$, respectively, post-illumination.

Fitting function: y=ax(1-exp(-b/x))

T / K	a / Am^2/mTs^{-1}	b / mTs^{-1}
0.3	$(9 \pm 3)\times10^{-9}$	(0.3 ± 0.1)
0.6	$(3 \pm 180)\times10^{-6}$	(0.001 ± 0.078)
0.9	$(6 \pm 58)\times10^{-7}$	(0.005 ± 0.044)

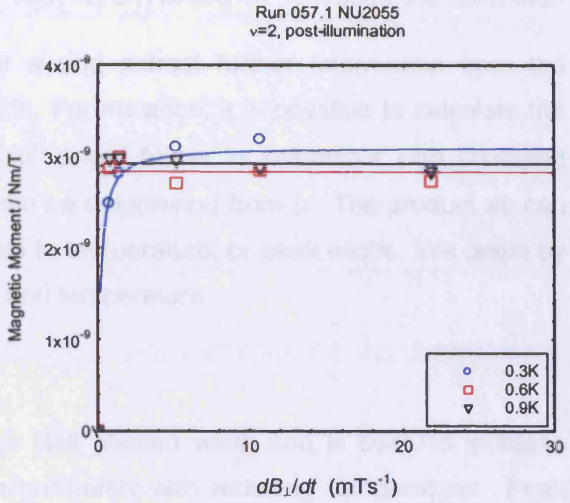

Figure 6.18: *Saturation curves at filling factor $\nu = 2$; the table displays the fitting parameters of the solid curves seen in the graph.*

Fitting function: y=ax(1-exp(-b/x))

T / K	a / Am^2/mTs^{-1}	b / mTs^{-1}
0.3	$(2 \pm 410)\times10^{-6}$	(0.001 ± 0.2)
0.6	$(3\pm 450)\times10^{-6}$	(0.001 ± 0.2)
0.9	$(1.4 \pm 0.2)\times10^{-8}$	(0.18 ± 0.03)

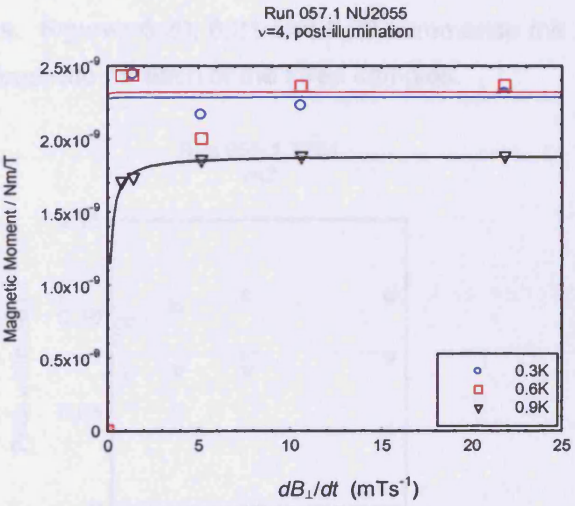

Figure 6.19: *Saturation curves at filling factor $\nu = 4$; the table displays the fitting parameters of the solid curves seen in the graph.*

The errors in parameters a and b are very large; as such the post-illumination data is not meaningful and will not be analysed further.

6.5 Further development of model

Having fitted the function $m^{peak} = \frac{m^{sat}}{b}\dot{B}\left(1-\exp\left(-b/\dot{B}\right)\right)$ where $m^{sat} = ab$ to the saturation curves, it is possible to calculate parameter a and extract further information from the equations for a and b, Equations 6.28 and 6.29. For instance, it is possible to calculate the longitudinal conductivity, σ_{xx}, from the value for a and follow its behaviour with changing temperature. The charge-up time constant τ can be determined from b. The product ab can also be examined with respect to its relationship to temperature, or peak width. We begin by examining the connection between peak width and temperature.

6.5.1 Peak width, ΔB

The peak width, ΔB, is a manifestation of the Hall plateau width and is seen to increase slightly with magnetic field sweep rate, and significantly with reducing temperature. Peak widths are obtained through the fitting of Gaussian functions to the eddy current peak signal previously shown in Figures 5.9, 5.18, 5.20, 5.26, 5.28 and 5.32. The Gaussian function provides a value for the half width at 1/e of the signal height. This value is doubled to attain the full width ΔB shown in the following figures. Figures 6.20, 6.21 and 6.22 summarise the behaviour of the peak width with respect to sweep rate for each of the three samples.

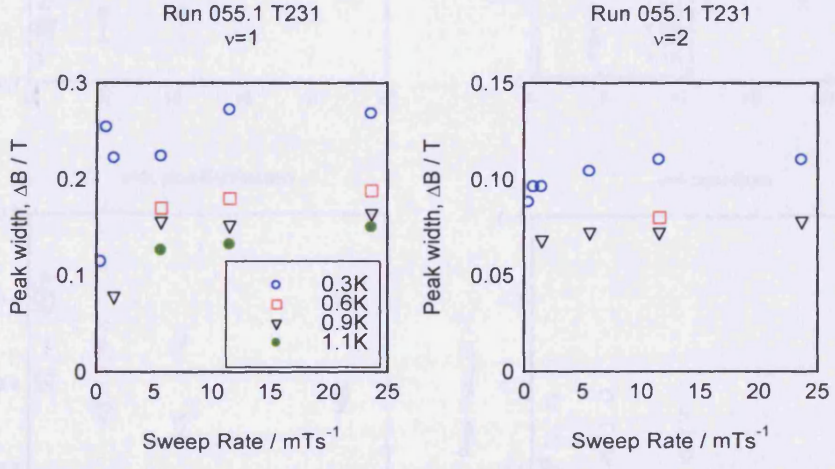

Figure 6.20: *Peak width (T) against sweep rate (mTs^{-1}) for sample T231 at filling factors ν = 1, 2, and temperatures as given in the key.*

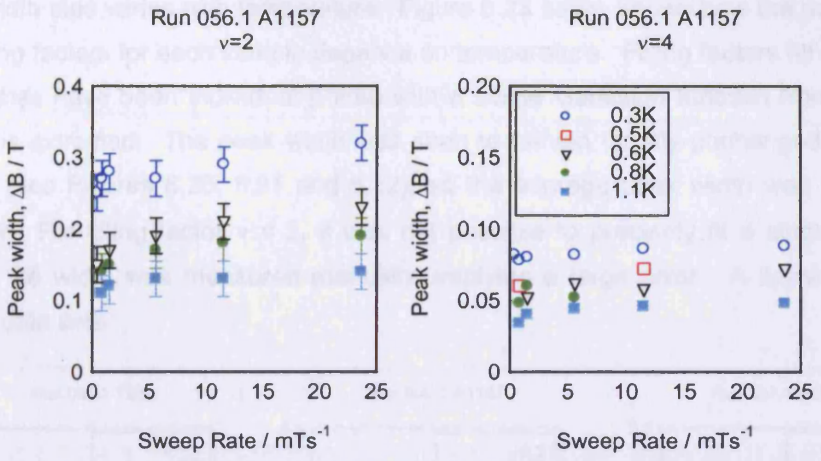

Figure 6.21: *Peak width (T) against sweep rate (mTs^{-1}) for sample A1157 at filling factors ν = 2, 4.*

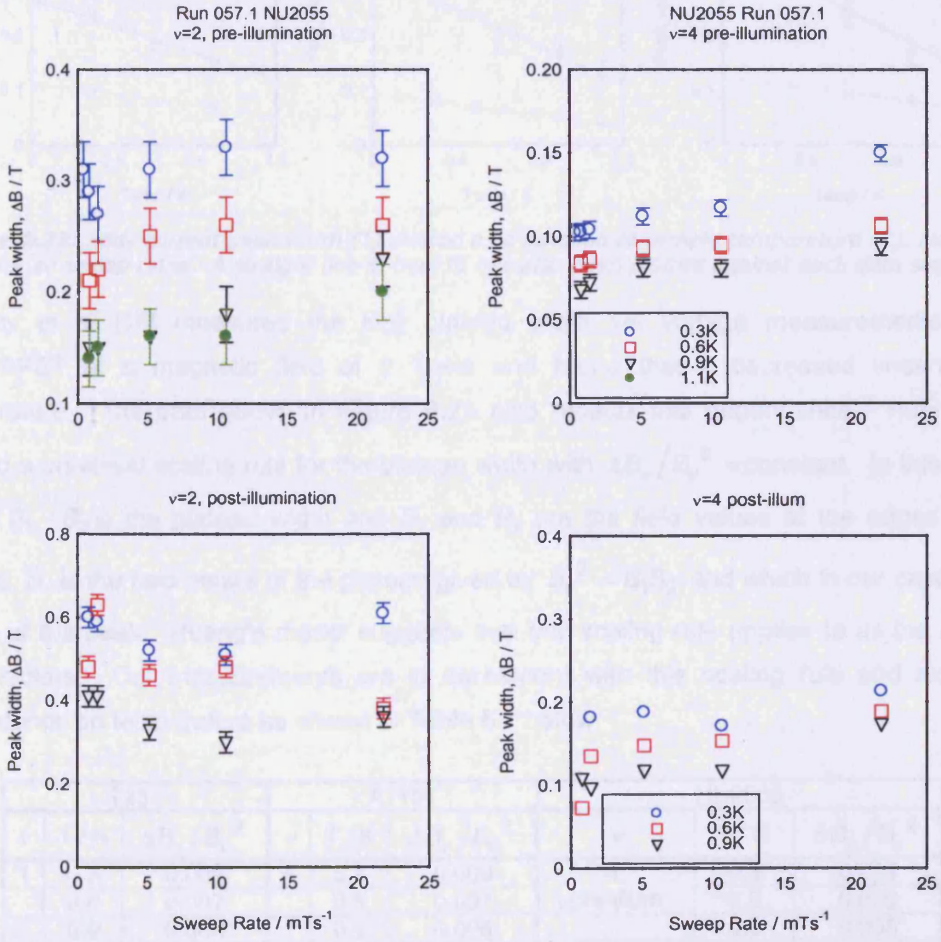

Figure 6.22: *Peak width (T) against sweep rate (mTs^{-1}) for sample NU2055 at filling factors ν = 2, 4, and before (upper graphs) and after (lower graphs) illumination.*

It can be seen that the peak widths remain largely the same size for varying sweep rate, although there is some evidence that the width reduces slightly for lower sweep rates.

The peak width also varies with temperature. Figure 6.23 below shows how the peak width of different filling factors for each sample depends on temperature. Filling factors other than 2 at all sweep rates have been individually fitted with a single Gaussian function from which the peak width is extracted. The peak width was seen to remain largely unchanged for varying sweep rate (see Figures 6.20, 6.21 and 6.22), so the average peak width was used in the figure below. For filling factor $\nu = 2$, it was not possible to precisely fit a single Gaussian function so the width was measured manually, implying a large error. A linear function is fitted to the data sets.

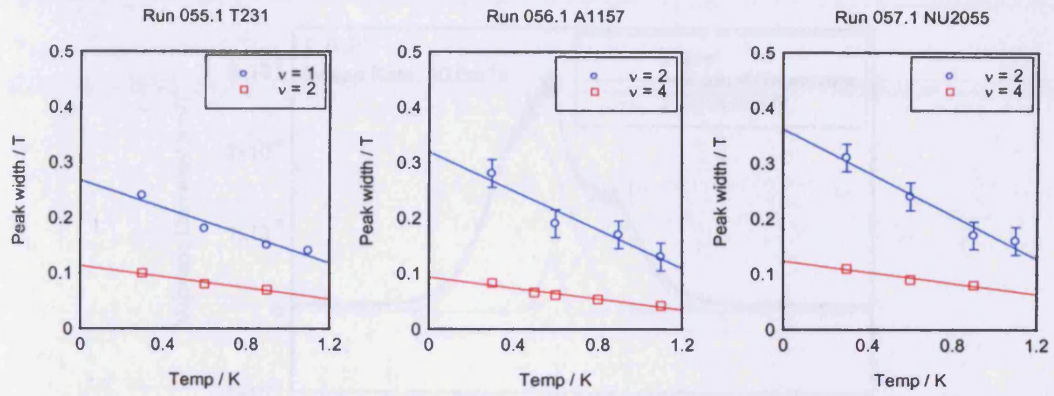

Figure 6.23: *Eddy current peak width (T) plotted as a function of sample temperature (K), averaged for all sweep rates. A straight line of best fit has also been plotted against each data set.*

Pudalov *et al* [16] measured the Hall plateau width via voltage measurements on a Si-MOSFET at a magnetic field of 8 Tesla and found that it decreased linearly with temperature. The data above in Figure 6.23 also reflects this dependence. Huang [17] derived a universal scaling rule for the plateau width with $\Delta B_\nu / B_\nu^2 = \text{constant}$. In this model $\Delta B_\nu = B_1 - B_2$ is the plateau width and B_1 and B_2 are the field values at the edges of the plateau; B_ν is the field centre of the plateau given by $B_\nu^2 = B_1 B_2$ and which in our case is the centre of the peak. Huang's model suggests that this scaling rule applies to all the integer filling factors. Our measurements are in agreement with this scaling rule and exhibit a dependence on temperature as shown in Table 6.1 below.

T231			A1157			NU2055		
ν	T / K	$\Delta B_\nu / B_\nu^2$	ν	T / K	$\Delta B_\nu / B_\nu^2$	ν	T / K	$\Delta B_\nu / B_\nu^2$
1	0.3	0.009	4	0.3	0.009	4, pre-illum	0.3	0.011
	0.6	0.007		0.5	0.007		0.6	0.009
	0.9	0.006		0.6	0.006		0.9	0.008
	1.1	0.005		0.8	0.005			
				1.1	0.004			
2	0.3	0.016				4, post-illum	0.3	0.010
	0.6	0.011					0.6	0.008
	0.9	0.011					0.9	0.007

Table 6.1: *Temperature dependence of $\Delta B_\nu / B_\nu^2$ (T^{-1}) as given by the scaling law of Huang [17], as averaged over all sweep rates.*

As mentioned above, it was not possible to fit single Gaussian functions to data for samples A1157 and NU2055 at filling factor $\nu = 2$, due to the extra shoulder-like structure observed on each side of the peak. As such Table 6.1 does not contain values at $\nu = 2$ for either sample A1157 or NU2055 since peak width values were measured manually and peak centre positions could not be estimated. Instead, it was found that a sum-of-three-Gaussians function could be fitted to the peak shape convincingly. An example of such a fit is given below in Figure 6.24.

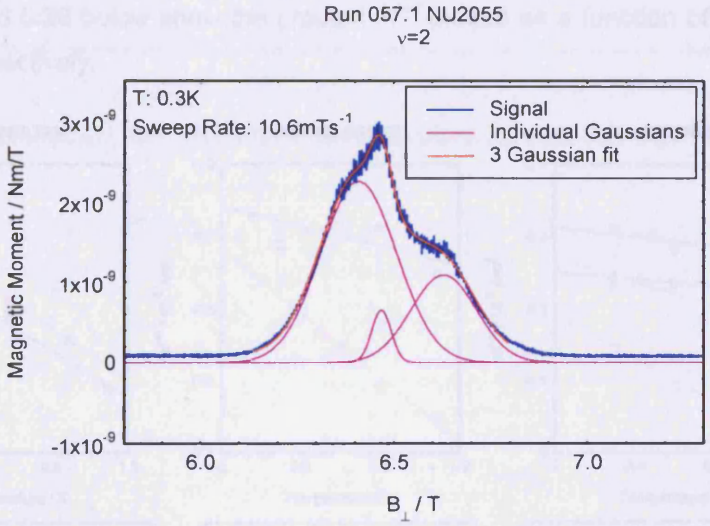

Figure 6.24: *Example of a sum of three Gaussians fit to $\nu = 2$ data of sample NU2055.*

The three individual Gaussians are plotted as pink lines and sum to give the total fit (red line) that correlates persuasively with the experimental trace (in blue). Analysis of the fitting parameters involved is presented more thoroughly in section 6.5.8.

6.5.2 Magnetic moment saturation value, m^{sat}

By calculating the product of *a* and *b* one simply arrives at the value of magnetic moment, m^{sat}, to which the eddy current peak height saturates at high sweep rates. It can be seen from the saturation curves of section 6.4 that m^{sat} shrinks as the temperature is increased from the base temperature of 0.3K. Section 6.4.1 described how equation 6.29 could be modified to yield a better fit to the saturation curves where m^{sat} and its error could be extracted directly. This procedure is followed to obtain the data presented in this section. Figures 6.25 and 6.26 below show the product m^{sat} plotted as a function of temperature and peak width, respectively.

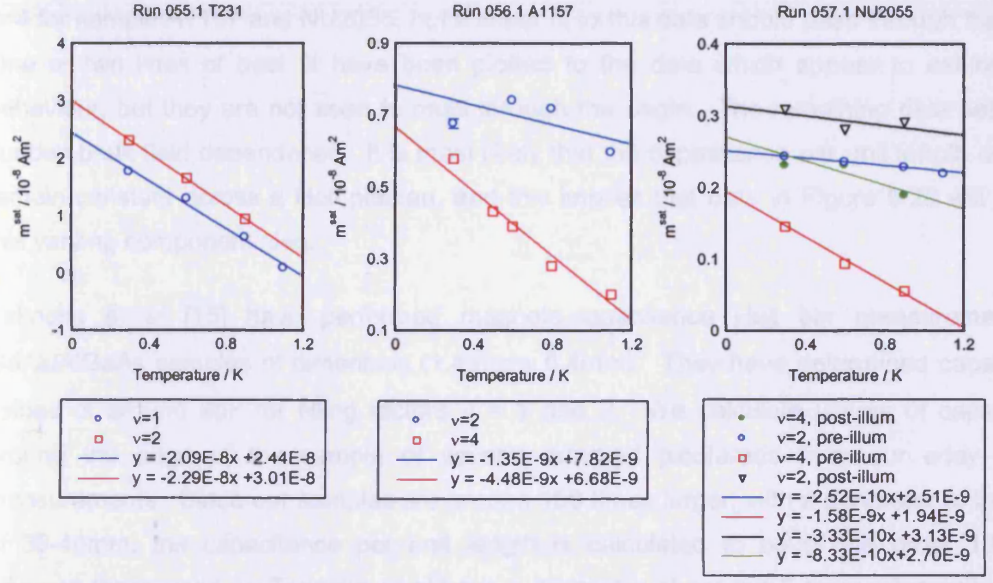

Figure 6.25: *m^{sat} (Am^2) as a function of temperature (K). The boxes below each graph display the linear fitting functions used.*

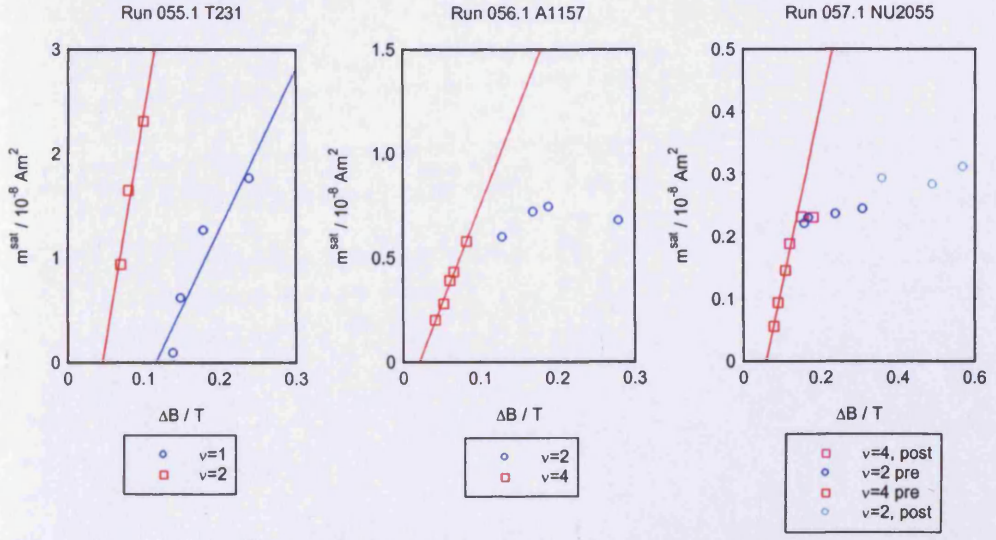

Figure 6.26: *m^{sat} (Am^2) against peak width, ΔB (T). The third graph, for sample NU2055 shows pre-illumination (pre) and post-illumination (post) data for each filling factor. Linear fits are applied where appropriate. Error bars are included, but are too small to be visible.*

It can be seen that the product *ab* is inversely proportional to temperature, in a similar way to the peak width, ΔB. A linear dependence on peak width might be expected from the charge-up model, since m^{sat} is expressed as the product of parameters *a* and *b*, which using Equations 6.30 and 6.31, gives:

$$m^{sat} \approx \sigma_{xy}{}^2 \frac{\pi}{2} R^3 \frac{\Delta B}{2C}. \tag{6.38}$$

where *C* is the capacitance per unit length. Provided all remaining values are constant, one would expect m^{sat} to exhibit a linear dependence on peak width ΔB. There is evidence in Figure 6.26 that m^{sat} grows linearly with peak width, especially at ν=2 for sample T231 and ν=4 for sample A1157 and NU2055, but a linear fit to this data should pass through the origin. One or two lines of best fit have been plotted to the data which appear to exhibit linear behaviour, but they are not seen to pass through the origin. The remaining data sets show curious peak field dependence. It is most likely that the capacitance per unit length does not remain constant across a Hall plateau, and this implies that data in Figure 6.26 will include this varying component also.

Takaoka *et al* [15] have performed magneto-capacitance Hall bar measurements on GaAs/AlGaAs samples of dimension (1.4mm × 0.4mm). They have determined capacitance values of around 2pF for filling factors ν = 1 and 2. We calculate values of capacitance around the edge of the sample of several hundred picofarads from our eddy current measurements. Since our samples are around 150 times larger, with a perimeter of the order of 30-40mm, the capacitance per unit length is calculated to be of the order 10pF/mm whereas those used by Takaoka *et al* have a perimeter of around 3-4mm, corresponding to around 1pF/mm. Hence these values of capacitance per unit length would appear to be in approximate agreement.

6.5.3 Temperature dependence of conductivity, σ_{xx}

The temperature dependence of the longitudinal conductivity is now examined. Polyakov and Shklovskii [18] presented a temperature dependence model for σ_{xx} of the form

$$\sigma_{xx} \sim \sigma_0 \exp\left[-\left(\frac{T_0}{T}\right)^{\frac{1}{2}}\right] \tag{6.39}$$

where T_0 is a characteristic temperature identified as

$$T_0 = C\frac{e^2}{k_B \varepsilon \xi(\nu)}; \tag{6.40}$$

here ξ is a localisation length and $\varepsilon = \varepsilon_0\varepsilon_r$ is the dielectric constant (ε_r~14 for our GaAs/AlGaAs samples).

From our model the parameter a is given by

$$a = \frac{\sigma_{xy}^{\,2}}{\sigma_{xx}}\frac{\pi}{2}wR^3, \tag{6.41}$$

so it follows that

$$a = \exp\left(\left(\frac{T_0}{T}\right)^{1/2}\right)\frac{\sigma_{xy}^{\,2}}{\sigma_0}\frac{\pi}{2}wR^3 \tag{6.42}$$

and

$$\ln(a) = \left(\frac{T_0}{T}\right)^{1/2} + \ln\left(\frac{\sigma_{xy}^{\,2}}{\sigma_0}\frac{\pi}{2}wR^3\right). \tag{6.43}$$

Therefore, by plotting $\ln(a)$ as a function of $\left(1/T\right)^{\frac{1}{2}}$ it is possible to assess this model with respect to the experimental data collected for our samples. Figure 6.27 below displays plots of this form for each of the three samples tested.

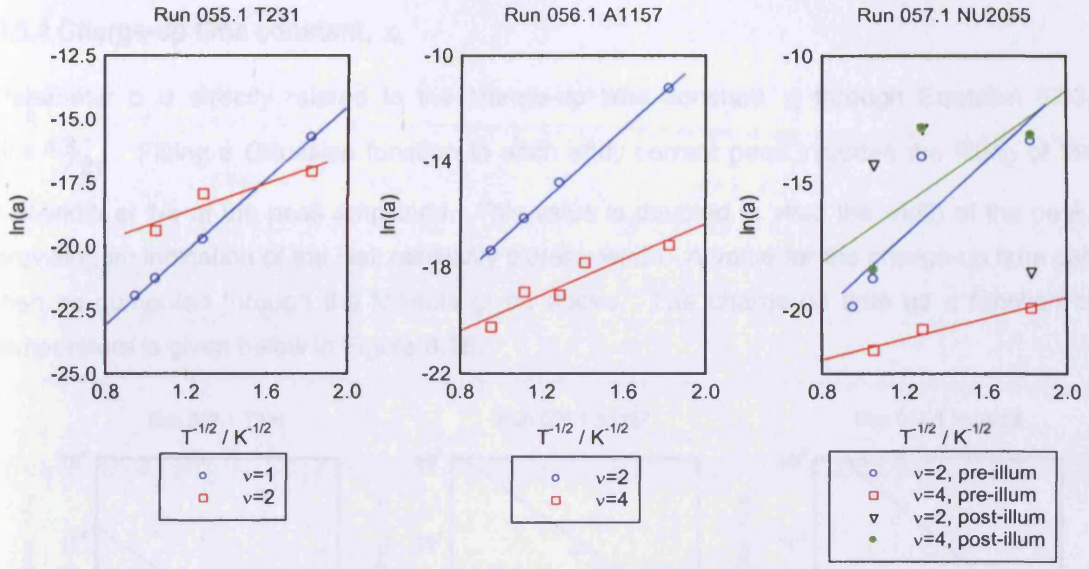

Figure 6.27: *Ln(a) as a function of $T^{-1/2}$ fitted with the model of Polyakov and Shklovskii [18].*

The data points appear to agree well with the straight lines fitted to them. Although there are only three points in some cases the data generally correlates closely to the linear fit. Table 6.2 below summarises the characteristic values extracted from Polyakov and Shklovskii's model.

T231			A1157			NU2055		
filling factor	T_o / K	σ_0 / Ω^{-1}	filling factor	T_o / K	σ_0 / Ω^{-1}	filling factor	T_o / K	σ_0 / Ω^{-1}
1	52	1.7×10^{-5}	2	49	1.0×10^{-7}	2 (pre-illum)	55	1.5×10^{-7}
2	8	7.1×10^{-8}	4	12	1.7×10^{-7}	2 (pre-illum)	31	5.4×10^{-8}
						4 (pre-illum)	4	$5.0\times^{-8}$
						4 pre-illum)	n/a	n/a

Table 6.2: *Summary of characteristic temperatures (T_0) and conductivities (ρ_o) obtained through fitting function published by Polyakov and Shklovskii.*

The values for σ_0 are calculated through Equation 6.43 using the slope and y-intercept values obtained through the fits displayed in Figure 6.27. Since the width, *w*, is an unknown quantity it is necessary to set $w = R$ in order to obtain an estimate for ρ_0 (an R^4 dependence was determined in an earlier work [10]). A more accurate approximation of the value of *w* would provide a better indication of σ_0.

6.5.4 Charge-up time constant, τ_c

Parameter b is directly related to the charge-up time constant τ_c through Equation 6.33, $b = \Delta B / 2\tau$. Fitting a Gaussian function to each eddy current peak includes the fitting of the half-width at 1/e of the peak amplitude. This value is doubled to yield the width of the peak, providing an indication of the Hall resistivity plateau width. A value for the charge-up time can then be computed through the formula given above. The charge-up time as a function of temperature is given below in Figure 6.28.

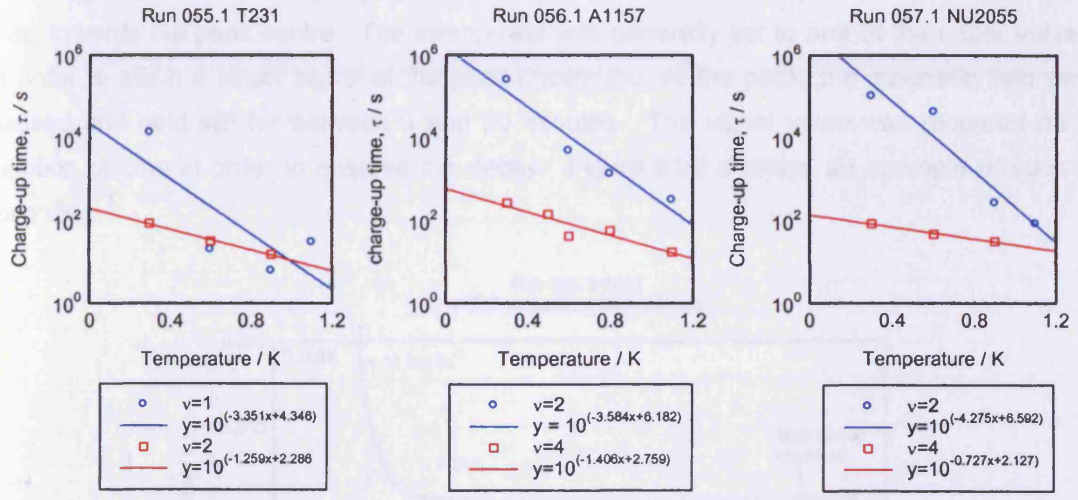

Figure 6.28: *Charge-up time (in seconds, plotted on a log scale) against temperature (K).*

It can be seen that when plotted on a log scale, the charge-up time can be fitted with a straight line against temperature; the sample takes much longer to charge-up at lower temperatures. This would seem sensible, however, as it is known that the eddy current peaks reduce in height as temperature increases even if the sweep rate remains constant. This could imply that the sample charges up less at elevated temperature which will obviously take less time when the sweep rate is unchanged.

6.5.5 Decay time constant τ_d

In order to study the decay of the eddy currents a separate set of time-decay experiments were performed in which the magnetic field was swept to the point of maximum peak size and then the field was halted. It is expected from the classical model that the magnetic moment has a linear dependence on sweep rate (Equation 6.13), and that if the magnetic field sweep were paused the signal would immediately fall to zero. This was not found to be the case experimentally so the signal decay was investigated with further "time-decay" measurements.

The magnetic field was swept through the eddy current peak to the point of maximum signal size, towards the peak centre. The sweep rate was generally set to one of the upper values in order to attain a larger signal at the peak maximum. At the peak, the magnetic field was paused and held still for between 8 and 20 minutes. The signal value was recorded as a function of time in order to observe the decay. Figure 6.29 displays an example of such a recording.

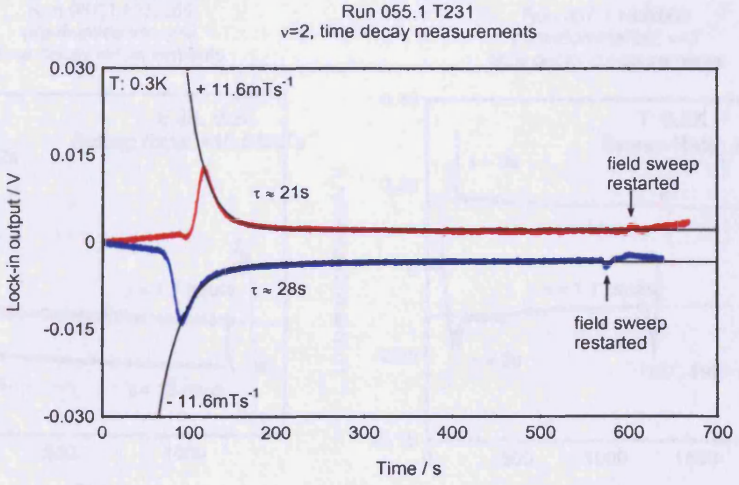

Figure 6.29: *Decay time measurements for sample T231. The magnetic filed was swept to the signal peak and then paused (at t~100s) for 8 minutes. The up-sweep is displayed as the red line, and the down-sweep as the blue line. The black lines indicate the fitted exponentially decaying functions.*

In this case, a single decay curve can be fitted to the signal implying a single time constant of decay of the order ~20 seconds. The same procedure was applied to the two remaining samples, A1157 and NU2055, and the results are presented below in Figures 6.30 and 6.31. In contrast to sample T231 it was found that the decay demonstrated two distinctive regimes in which signal decays at different rates. The first decay regime is a rapid decay in which the signal magnitude falls steeply corresponding to a small time constant of the order of several seconds, rather like the single fitted decay function for the T231 data in Figure 6.29. The signal then enters a second regime where the decay becomes much slower and the signal reduction is much shallower. Through fitting a second decay curve to this section of data much longer time constants were extracted, of the order of many minutes, and even hours.

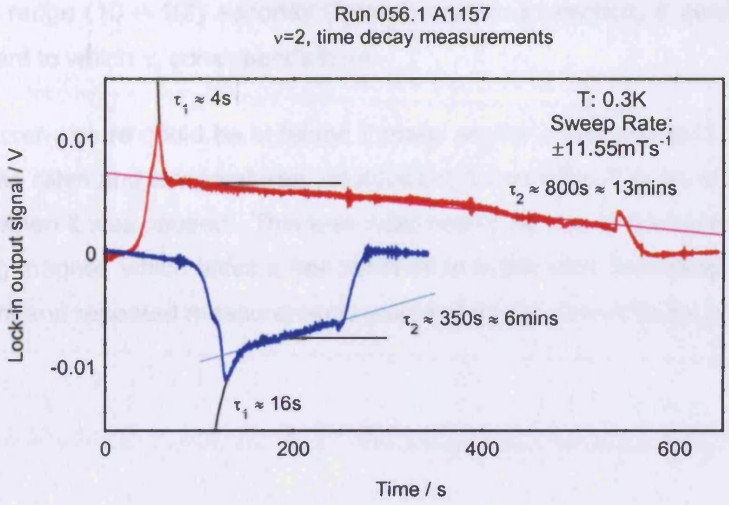

Figure 6.30: *Decay time measurements for sample A1157. The magnetic field was swept to the signal peak and then paused: the upsweep (red line) was paused for 8 minutes, and the down-sweep (blue line) for only 2 minutes. The black lines on each sweep show the short time constant fit, and the light blue and pink lines show the long time constant fits.*

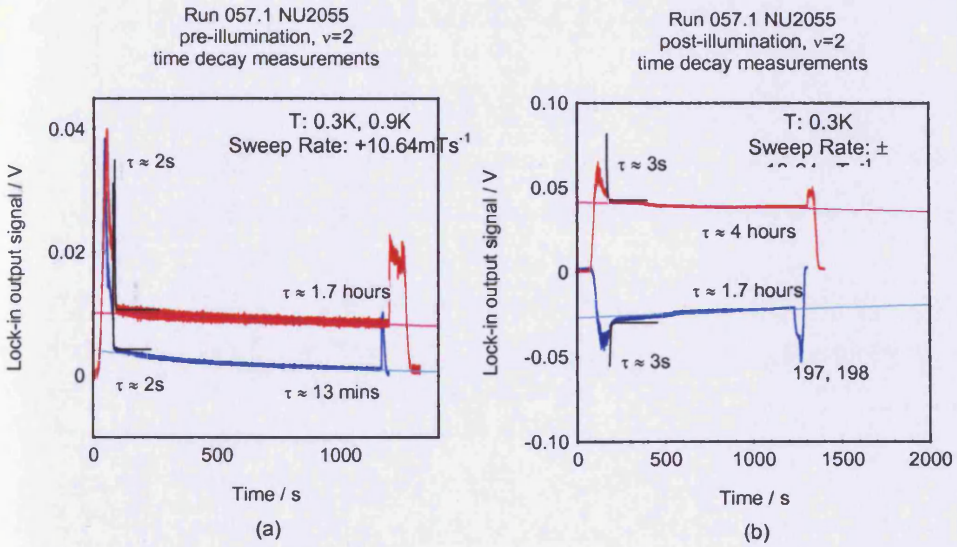

Figure 6.31: *Decay time measurements for sample NU2055 (a) pre-illumination and (b) post-illumination. The magnetic field was swept to the signal peak and then paused for 20 minutes. The black lines on each sweep show the short time constant fit, and the light blue and pink lines show the long time constant fits. In (a), the red trace was taken at T=0.3K, and the blue trace at T=0.9K; in (b) T=0.3K for both traces.*

The time constant given in the charge-up model is

$$\tau = \frac{Cw}{\sigma_{xx}} \tag{6.44}$$

and it governs how long it takes for the charge build-up at the sample edge to reach a maximum. By comparison with the charge-up times extracted from the relation

$$\tau = \frac{\Delta B}{2b} \tag{6.45}$$

which lie in the range (10 – 10^5) seconds (from the previous section) it seems that it is the long time constant to which τ_c corresponds here.

Obviously a clearer picture could be obtained if many similar measurements were performed at different sweep rates and temperatures. In addition, it was difficult to be exactly sure of the true field value when it was paused. This was assumed to be due to the switch heater on the superconducting magnet, which takes a few seconds to settle after sweeping. Improvements to this equipment and repeated measurements would allow for more reliable conclusions.

6.5.6 Characteristic temperature, T_0

In section 6.4 it was seen that the magnetic moment amplitude reached saturation when plotted as a function of sweep rate. Curves were fitted to these data sets for each sample, at varying filling factors and sample temperatures, and the parameters *a* and *b* were extracted. By plotting *a* and *b* as a function of temperature, it is possible to obtain characteristic temperature (T_0) values for some filling factors where the fits were sensible. Table 6.3 below summarises these values.

Sample	Filling Factor	$T_0(a)$ / K	$T_0(b)$ / K
T231	1	(0.20 ± 0.05)	(0.33 ± 0.20)
	2	(0.61 ± 0.03)	(1.00 ± 0.08)
A1157	4	(0.62 ± 0.11)	(0.95 ± 0.29)
NU2055	2, pre-illumination	(0.41 ± 0.01)	(0.34 ± 0.06)
	4, pre-illumination	(0.83 ± 0.001)	(2.00 ± 0.16)

Table 6.3: *Summary of characteristic temperatures as found through plotting parameters a and b on a logarithmic scale against temperature (linear) and fitting a straight line.*

It was expected that *a* and *b* would exhibit opposite temperature dependences since *b* is linearly proportional to the conductivity σ_{xx} while *a* is inversely proportional to it (Equation 6.33), and σ_{xx} itself is strongly dependent on temperature. This was found to be the case on plotting the parameters against temperature as seen in section 6.4. Generally, the characteristic temperature found through parameter *b* is slightly larger than that for parameter *a*. It is believed that since *b* is also proportional to the peak width ΔB, which is itself weakly dependent on temperature, that this extra factor results in a slightly larger characteristic temperature than that found through parameter *a*, which does not depend on any other temperature-dependent variables. Given that there is considerable scatter on the plots in section 6.4 from which the data in Table 6.3 was extracted, and that there are only a few points available for each plot, the errors stated for the temperatures above are not considered accurate. Further measurements at other temperatures would be useful in order to acquire additional data points on each plot; repeated measurements would limit any scatter. In this way more accurate fits could be performed.

6.5.7 Eddy current peak shape

It is seen that for filling factors other than $\nu = 2$, the shape of the eddy current peak induced upon sweeping the field over a Hall plateau takes the general form of a Gaussian function. The charge-up model is now examined to draw out the sort of peak shape that would be expected if the model is followed.

It is known that as the magnetic field sweeps over integer filling factor the longitudinal resistivity ρ_{xy} reaches a plateau while the longitudinal resistivity ρ_{xx} approaches zero [19]. These components are shown schematically in Figure 6.32.

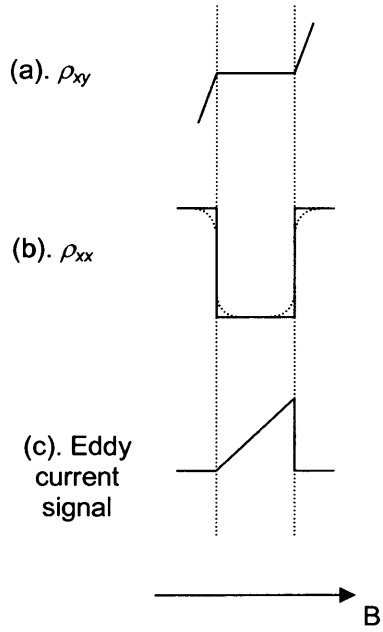

Figure 6.32: *Diagram to illustrate proposed resistivity and induced current form as a function of magnetic field.*

The charge-up model assumes that the longitudinal resistivity ρ_{xx} takes a rectangular form, dropping straight to zero with no additional structure, as illustrated by the solid lines in Figure 6.32(b). This change in ρ_{xx} would infer a linear growth of induced circulating current, so one would expect to observe a peak shape from the charge-up model as shown in Figure 6.32(c). This form is not detected experimentally; Figure 6.33 recaps some of the typical eddy current peak shapes observed at low temperature.

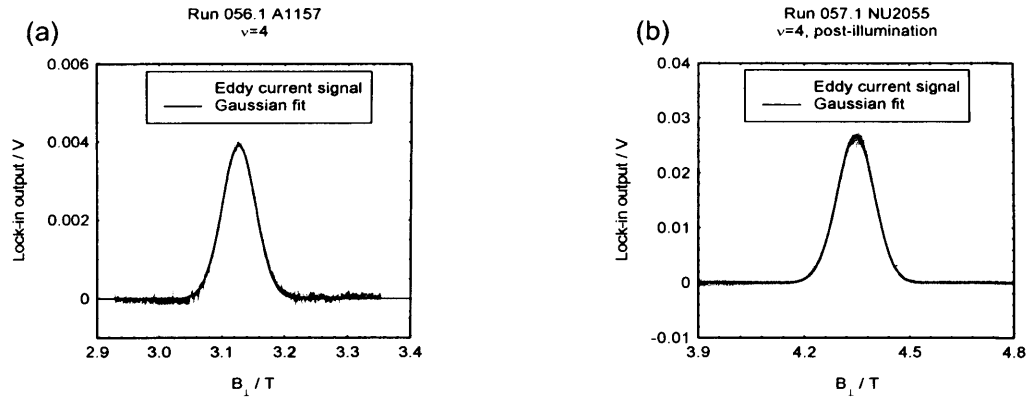

Figure 6.33: *Two examples of the Gaussian eddy current peak shape observed in two different samples, (a) A1157; (b) NU2055. Each graph shows the voltage signal from the lock-in (an indication of the deflection of the sample as a result of the torque induced via the circulating eddy currents in the sample) as well as the fitted Gaussian function.*

Instead of the asymmetric triangular form predicted, the peak takes on a symmetrical Gaussian form, indicating that there are modifications necessary to the model. For instance, the longitudinal resistivity is unlikely to drop from an arbitrary value to zero in the sudden manner illustrated by the solid lines in Figure 6.32; perhaps it has a more gradual profile as shown by the dotted lines. If the width w of the channel through which the current j_x flows is very small, then the electric field E_y across this channel will be large therefore limiting the induced eddy current signal observed. As breakdown is approached currents will begin to be dissipated into the bulk which will restrict the size of the currents circulating near the edge of the sample, therefore reducing the size of the magnetic moment signal from that expected by the charge-up model.

In section 6.3.1 the values of measured capacitance and channel width published by Takaoka *et al* [15] were presented as ~2pF and ~1μm respectively. These values produce a maximum electric field value, E_y^{crit}, of ~10^7Vm^{-1} when used in the charge-up model (Equation 6.25), which corresponds to a critical current density, j_x^{crit}, of ~10^3Am^{-1} (Equation 6.26). These values would seem very large compared to general published values in the range (10^3-10^4)Vm^{-1} for breakdown field and (0.5-50)Am^{-1} for breakdown current density (see literary review of breakdown models in section 6.1). If the channel width were increased to 70μm [20] then the critical electric field becomes ~10^5Vm^{-1} with a current density of ~30Am^{-1}, which seems in better agreement with published values.

One explanation for such enlarged critical values is that they would be the values reached by the electric field and current density, if they were not limited by a particular breakdown mechanism. We expect to see a linearly growing, asymmetric eddy current signal from the charge-up model but instead observe a Gaussian-like symmetrical signal. Figure 6.34 illustrates the comparison between the two.

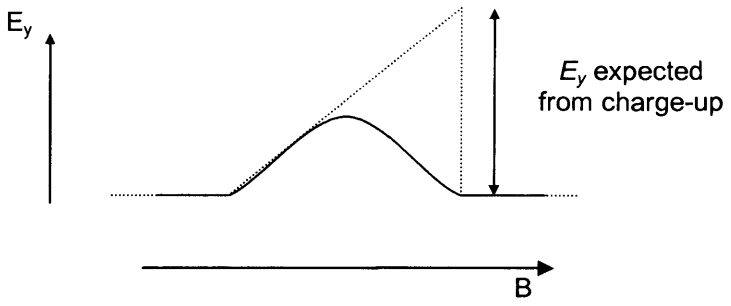

Figure 6.34: *Comparison between predicted and observed eddy current signals. The charge-up model is shown as the straight dotted line and the observed signal shape is shown as a solid line.*

The electric field signals displayed in Figure 6.34 are proportional to current density and therefore magnetic moment so the figure serves as a qualitative demonstration of the electric field perpendicular to the circulating currents. It is possible that as the magnetic field sweeps the system rapidly charges up and reaches a level of saturation that limits further signal growth. Takaoka *et al* [15] also quote values for the longitudinal conductivity σ_{xx} as ~10^{-14}S which allows the calculation of the charge-up time constant,

$$\tau = \frac{Cx}{\sigma_{xx}} \approx 0.1\text{sec}, \tag{6.46}$$

and if the larger channel width of Fontein *et al* [20] is used $\tau \approx 5$s. The time taken to sweep through a typical eddy current peak lies in the range 20-1000 seconds, much longer than the time constant. Therefore, the system will be fully charged up very soon into the peak which could explain the deviation in signal size from the predicted height.

This saturation does not explain the distinct signal shape however. The model assumes a constant value for the longitudinal conductivity σ_{xx} which is probably unreasonable. Hohls *et al* have measured σ_{xx} as a function of magnetic field and filling factor [21, 22] in GaAs/AlGaAs samples of Corbino geometry, of which data is presented below in Figure 6.35. The longitudinal conductivity σ_{xx} is clearly not a constant value across an integer filling factor plateau. Instead it exhibits a curved structure at the plateau edges. This has clear implications for the charge-up model in which the conductivity is assumed to be constant. If the form of σ_{xx} were known more fully it might be possible to visualise a more adequate description of the peak shape.

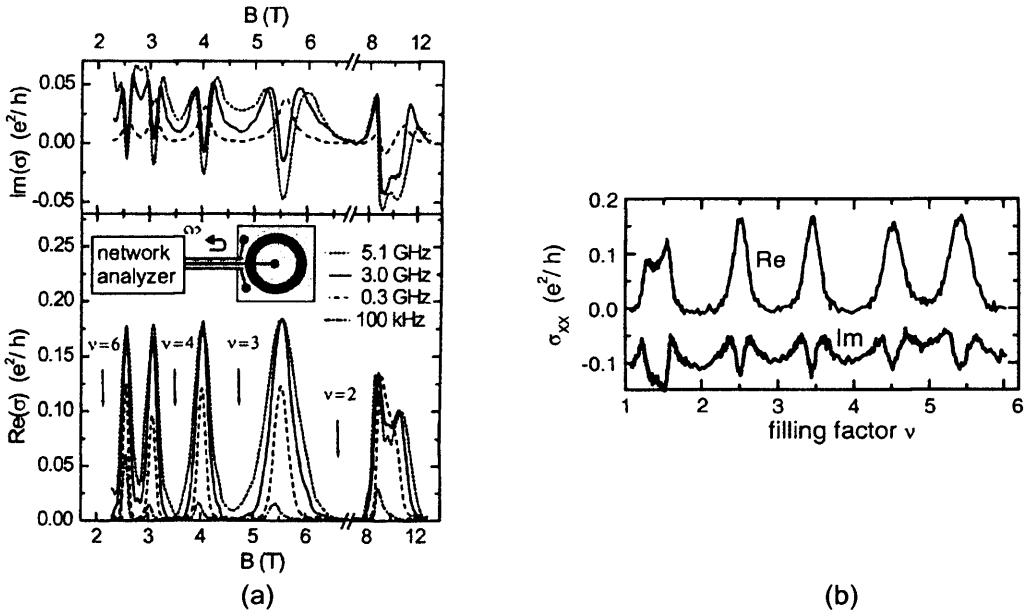

Figure 6.35: *Longitudinal conductivity σ_{xx} as a function of (a) magnetic field [21] and (b) filling factor [22], measured by Hohls et al.*

Ideally the conductivity would follow an inverse Gaussian function if it is to account for the Gaussian peak shape observed in our measurements. By inspection of the work of Hohls *et al* and comparison with the shape of an inverse Gaussian as displayed in Figure 6.36 below, this does not seem unreasonable. It is possible that σ_{xx} exhibits an inverse Gaussian form, but it would obviously be necessary to fit such functions to real experimental data to justify this.

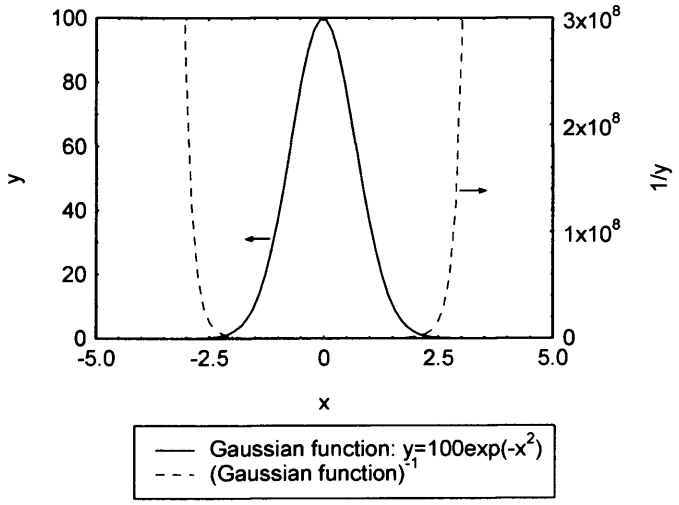

Figure 6.36: *The Gaussian (y) and inverse Gaussian (1/y) functions*

6.5.8 Peak shape at filling factor ν = 2

Another interesting outcome is the peak shape observed at filling factor ν = 2 for both samples A1157 and NU2055 where the peaks broaden out such that they appear to have a shoulder on each side. This effect has been seen on other samples measured in Cardiff (for instance, sample NU762 [11]). We revisit the data shown in Figure 5.28 to demonstrate the shoulder-like features exhibited at filling factor ν = 2 for sample NU2055 and re-present the figure below in Figure 6.37.

At temperatures greater than ~1K the signal appears to exhibit the familiar single-Gaussian shaped peak although the peak is not exactly symmetrical and additional structure can be seen. As the temperature decreases the peak begins to develop extra shoulder-like structures, one on each side. By T~0.6K the shoulders have become very pronounced.

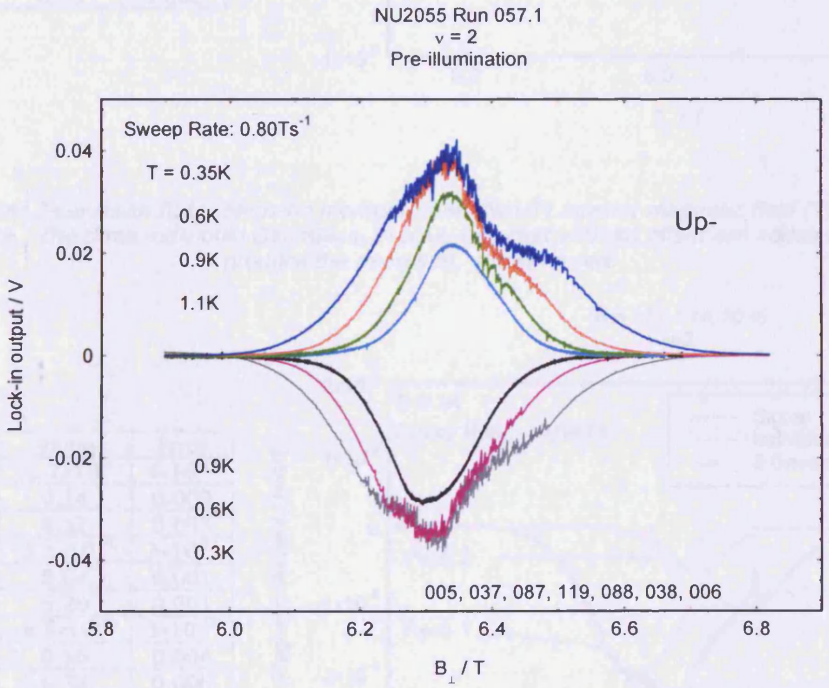

Figure 6.37: *Temperature-dependence of ν=2 for NU2055 at constant sweep rate (0.80mTs⁻¹).*

It appears that three Gaussian functions compose the peak, overlapping closely at high temperature, then spreading out and becoming more pronounced as the temperature decreases. The function employed to fit this data is given as

$$y = a_1 \exp\left(-\left(\frac{x-\mu_1}{\sigma_1}\right)^2\right) + a_2 \exp\left(-\left(\frac{x-\mu_2}{\sigma_2}\right)^2\right) + a_3 \exp\left(-\left(\frac{x-\mu_3}{\sigma_3}\right)^2\right) \qquad (6.47)$$

where the parameters denoted by a are the amplitudes of the individual Gaussian functions, μ are the peak centres in field and σ are the peak widths. Figures 6.38 and 6.39 show typical three-Gaussian curves fitted to the eddy current peak and demonstrate that the function is

compellingly appropriate for both positive and negative sweeps. The peaks are designated 1, 2 and 3, where peak 1 always refers to the peak at the lower field irrespective of sweep direction. Peak 2 is the central function, and usually considerably smaller when fitted, and peak 3 relates to the peak at the higher field.

Parameter	Value	Error
a_1	2.0×10^{-9}	1×10^{-11}
σ_1	0.14	0.001
μ_1	6.41	0.001
a_2	5.6×10^{-10}	1×10^{-11}
σ_2	0.04	0.008
μ_2	6.47	0.0004
a_3	9.4×10^{-10}	1×10^{-11}
σ_3	0.12	0.002
μ_3	6.63	0.002

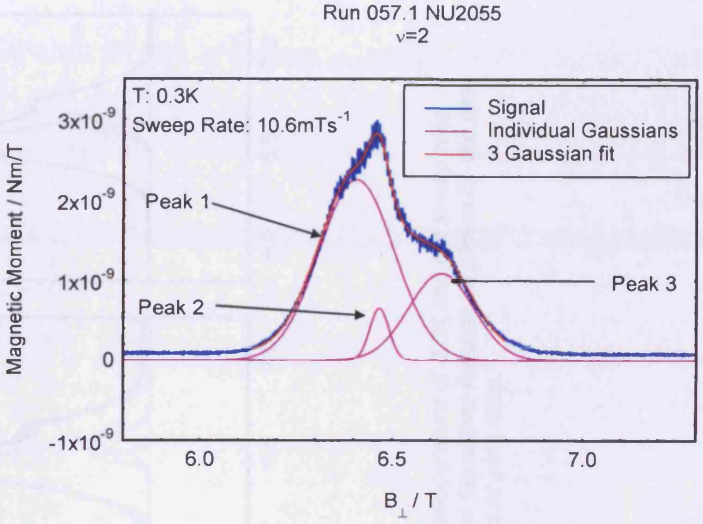

Figure 6.38: *3-Gaussian fit to magnetic moment peak (Nm/T) against magnetic field (T) for positive sweep rate. The three individual Gaussians, in pink, together with an offset are added together to produce the overall fit, shown in red.*

Parameter	Value	Error
a_1	-1.7×10^{-9}	4×10^{-11}
σ_1	0.14	0.002
μ_1	6.12	0.003
a_2	-5.1×10^{-10}	2×10^{-11}
σ_2	0.04	0.001
μ_2	6.20	0.001
a_3	-8.5×10^{-10}	3×10^{-10}
σ_3	0.16	0.004
μ_3	6.33	0.006

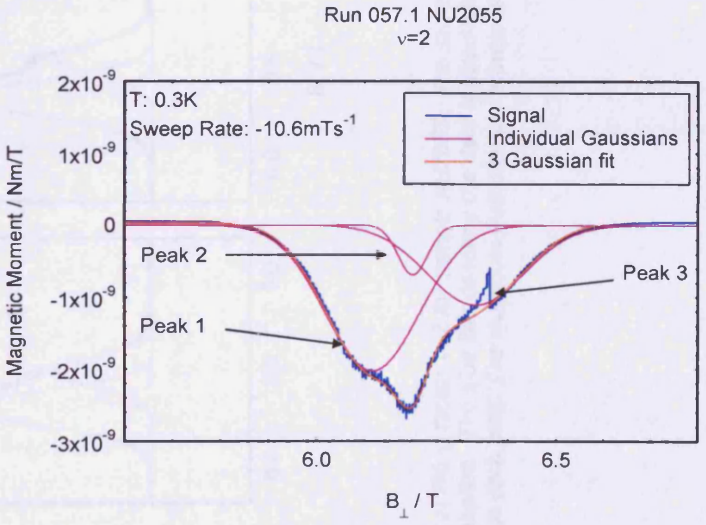

Figure 6.39: *3-Gaussian fit to magnetic moment peak (Nm/T) against magnetic field (T) for negative sweep rate. The three individual Gaussians, in pink, together with an offset are added together to produce the overall fit, shown in red.*

It appears that the individual peak widths and heights exhibit very similar magnitudes for both sweep directions. The three individual Gaussian functions can be analysed in the same way as the single functions fitted to entire eddy current peaks at other filling factors as seen previously. The height and width of each constituent peak can be examined to determine how it develops with respect to temperature and sweep rate, and to establish whether the

magnitude of a particular function's contribution alters as these conditions are varied. Figure 6.40 shows the triple Gaussian functions, and their constituent single Gaussian functions fitted to a series of peaks where the temperature is constant and the sweep rate is increasing.

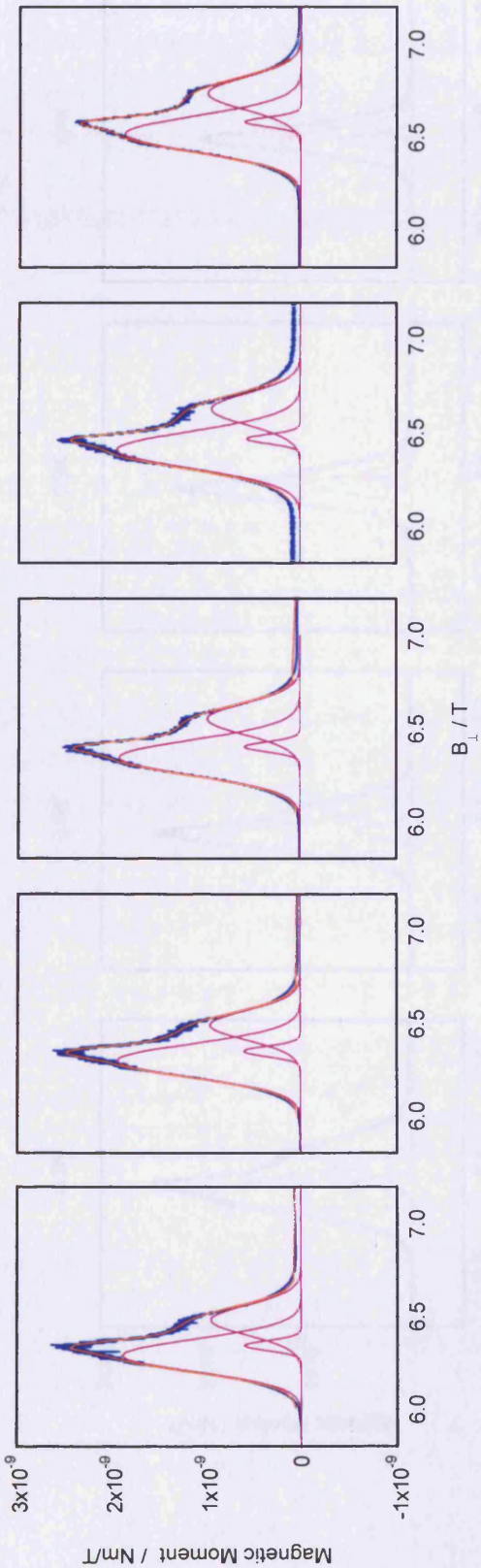

Figure 6.40: *Series of peaks at filling factor ν=2 for sample NU2055. The sample is at a base temperature of 0.3K and the sweep rate increases from left to right as labelled. The blue line denoting the data is fitted with a sum of three Gaussians function as shown by the red line in each plot. The individual Gaussian contributions are also plotted as pink lines.*

Figure 6.41 below shows a similar series of graphs, but for varying temperatures while the sweep rate remains constant at 5.18mTs^{-1}.

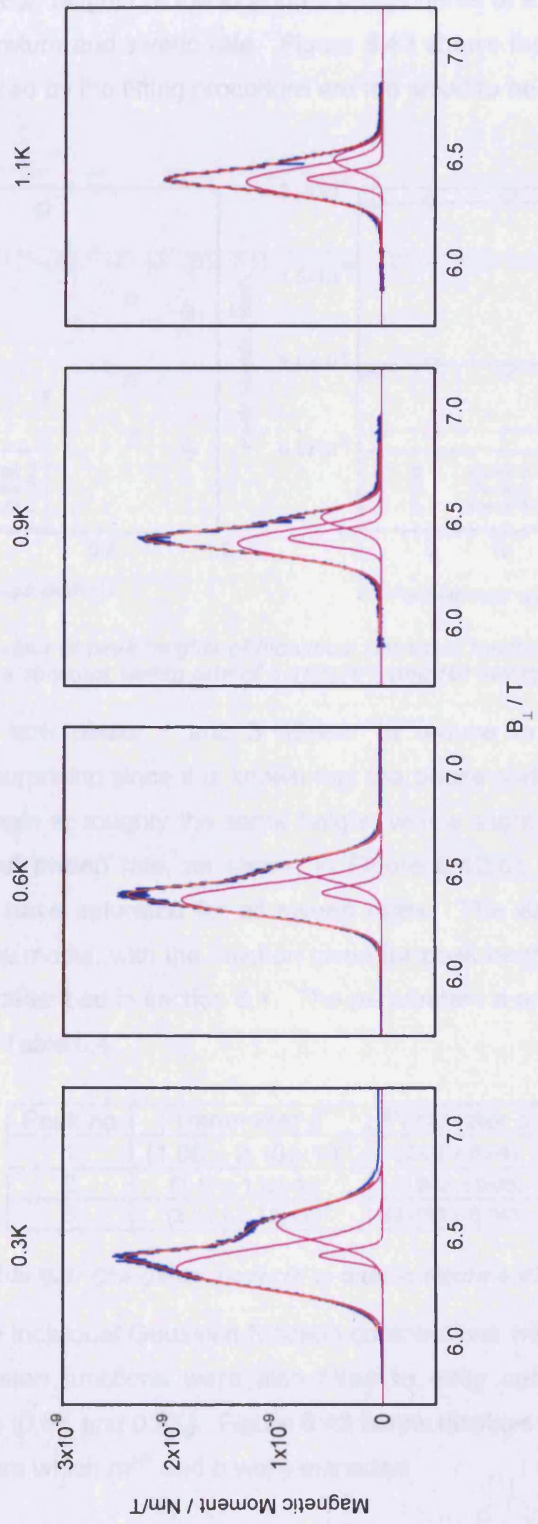

Figure 6.41: *Series of peaks at filling factor ν=2 for sample NU2055. The temperature increases from left to right as labelled while the sweep rate remains constant at 5.18mTs^{-1}. The blue line denoting the data is fitted with a sum of three Gaussians function as shown by the red line in each plot. The individual Gaussian contributions are also plotted as pink lines.*

Although it is clear in Figure 6.41 that the individual peaks vary considerably with changing temperature, it is difficult to tell purely from inspection how the individual peaks vary over sweep rate in Figure 6.40; it is therefore useful to study the fitting parameters themselves.

First we examine the peak heights of the individual components of a triple Gaussian function as a function of temperature and sweep rate. Figure 6.42 shows the results of the analysed data. Error bars produced by the fitting procedure are too small to be visible.

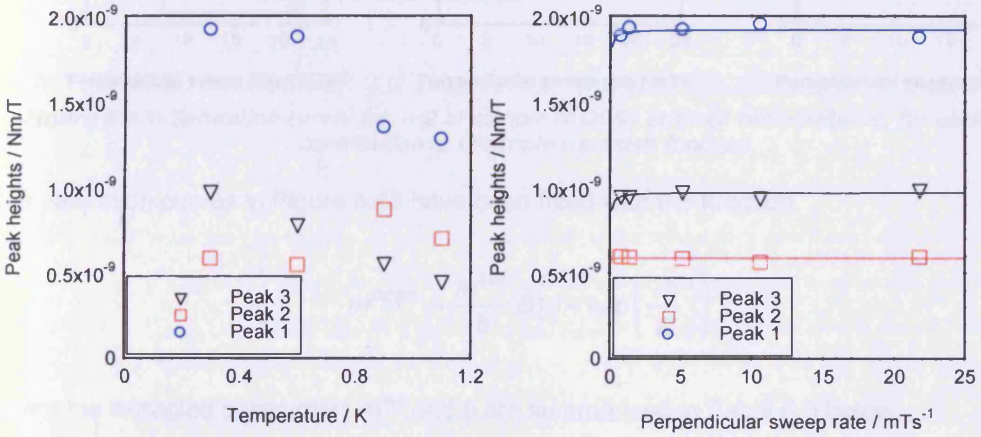

Figure 6.42: *Behaviour of peak heights of individual Gaussian functions with respect to (a) temperature at a constant sweep rate of 5.18mTs^{-1}, and (b) sweep rate at T=0.3K.*

Figure 6.42(a) shows how peaks 1 and 3 appear to reduce in height as temperature decreases. This is unsurprising since it is known that the peaks shrink as temperature rises. Peak 2 appears to remain at roughly the same height, with a slight rise at 0.9K. The peak heights as a function of sweep rate, as shown in Figure 6.42(b), seem to remain largely unchanged, as if they have saturated for all sweep rates. The data has been fitted with respect to the charge-up model, with the function given for peak height saturation in Equation 6.29, in the same way described in section 6.4. The parameters *a* and *b* extracted for the fits are presented below in Table 6.4.

Peak no	Parameter *a*	Parameter *b*
1	$(1.06 \pm 2.18)\times10^{-7}$	(0.02 ± 0.04)
2	$(3.43 \pm 100)\times10^{-7}$	(0.002 ± 0.05)
3	$(2.54 \pm 2.73)\times10^{-8}$	(0.038 ± 0.041)

Table 6.4: *Charge-up model fit to data in Figure 6.43(b).*

In order to examine the individual Gaussian function contributions with respect to the charge-up model, triple Gaussian functions were also fitted to eddy current peaks recorded at additional temperatures (0.6K and 0.9K). Figure 6.43 below displays the saturation curves for each individual peak from which m^{sat} and *b* were extracted.

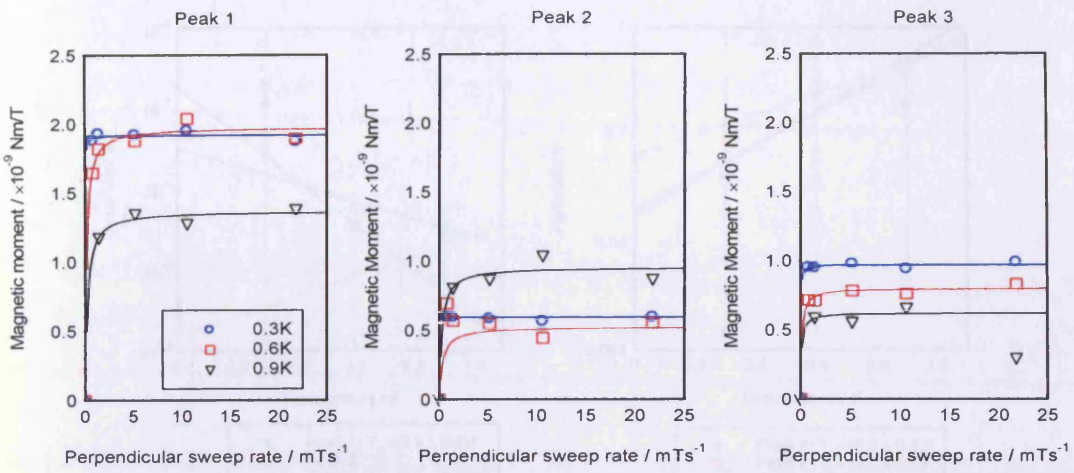

Figure 6.43: *Saturation curves for ν=2 of sample NU2055 at three temperatures, for each peak contribution to the triple Gaussian function.*

The saturation curves in Figure 6.43 have been fitted with the function

$$m^{peak} = \frac{m^{sat}}{b}\dot{B}\left(1-\exp\left(\frac{-b}{\dot{B}}\right)\right) \tag{6.48}$$

where the extracted parameters m^{sat} and b are summarised in Table 6.5 below.

	T / K	m^{sat}/Am^2	Parameter b / mTs^{-1}	Parameter a / Am^2/mTs^{-1} (from m^{sat} = ab)
Peak 1	0.3	$(1.92 \pm 0.02)\times10^{-9}$	(0.02 ± 0.03)	1.1×10^{-7}
	0.6	$(1.97 \pm 0.04)\times10^{-9}$	(0.28 ± 0.07)	7.0×10^{-9}
	0.9	$(1.37 \pm 0.04)\times10^{-9}$	(0.42 ± 1.81)	3.3×10^{-9}
Peak 2	0.3	$(5.92 \pm 11.34)\times10^{-10}$	(0.003 ± 4)	2.0×10^{-7}
	0.6	$(5.21 \pm 8.39)\times10^{-10}$	(0.62 ± 7)	8.4×10^{-10}
	0.9	$(9.51 \pm 5.77)\times10^{-10}$	(0.48 ± 0.38)	2.0×10^{-9}
Peak 3	0.3	$(9.69 \pm 0.11)\times10^{-10}$	(0.04 ± 0.04)	2.6×10^{-8}
	0.6	$(7.98 \pm 0.19)\times10^{-10}$	(0.23 ± 0.08)	3.5×10^{-9}
	0.9	$(6.22 \pm 0.46)\times10^{-10}$	(0.19 ± 0.37)	3.3×10^{-9}

Table 6.5: *Extracted parameters of saturation curve fits in Figure 6.43.*

The parameters a and b are then plotted against temperature in order to obtain characteristic temperatures for each peak, which can then be compared to those acquired in section 6.5.6. These plots are shown below in Figure 6.44.

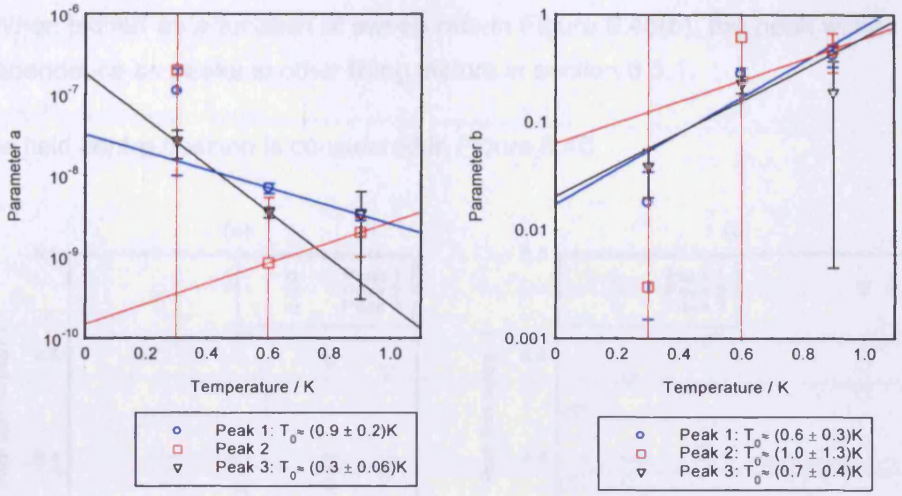

Figure 6.44: *The parameters a and b plotted against temperature (K) for NU2055, ν=2. The values of a and b are shown on a logarithmic scale.*

The characteristic temperature, T_0, of peak 2 for parameter *a* has not been quoted since the errors are so large and the slope of the fit is not correct. Since a number of fits are required to express the data as presented in Figure 6.44 (a triple Gaussian and a saturation curve) it is likely that accumulated errors on both parameters displayed in Figure 6.44 will be quite large. However, characteristic temperatures (T_0) seem reasonable for the individual peaks lying in the same range as those found for filling factor ν=4 for the same sample, as well as for different filling factors of sample A1157 and T231 (see Table 6.3 in section 6.5.6).

Figure 6.45 below displays similar data to Figure 6.44, but the peak width is now examined.

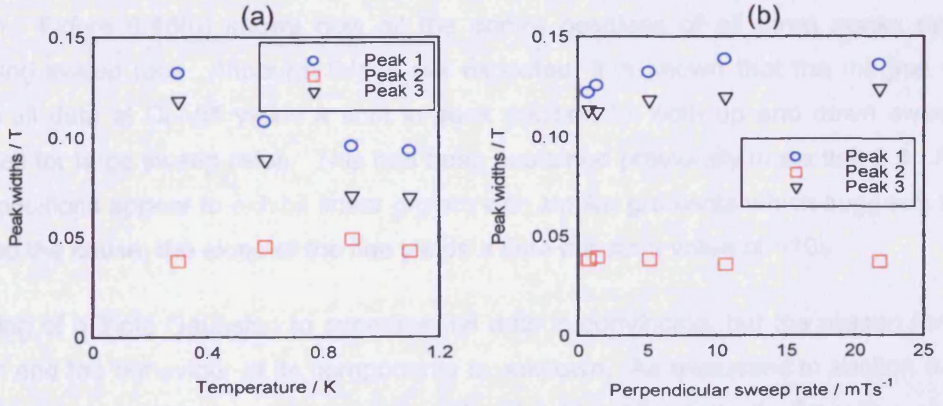

Figure 6.45: *Behaviour of peak widths of individual Gaussian functions with respect to (a) temperature at a sweep rate of 5.18mTs^{-1}, and (b) sweep rate at T=0.3K.*

The widths of the outer two peaks (1 and 3) reduce as the temperature increases. This is also expected since it can be seen in Figure 6.41, and in data for other filling factors, that the overall peak width reduces as temperature rises. Again, the width of peak 2 exhibits a similar magnitude, rising slightly with temperature. It is possible that peak 2 develops a more dominant contribution to the overall peak shape as temperature increases, since it can be seen to grow in the series of graphs in Figure 6.41 while the remaining two peaks seem to

shrink. When plotted as a function of sweep rate in Figure 6.45(b), the peak widths display a similar dependence as peaks at other filling factors in section 6.5.1.

Finally the field centre position is considered in Figure 6.46.

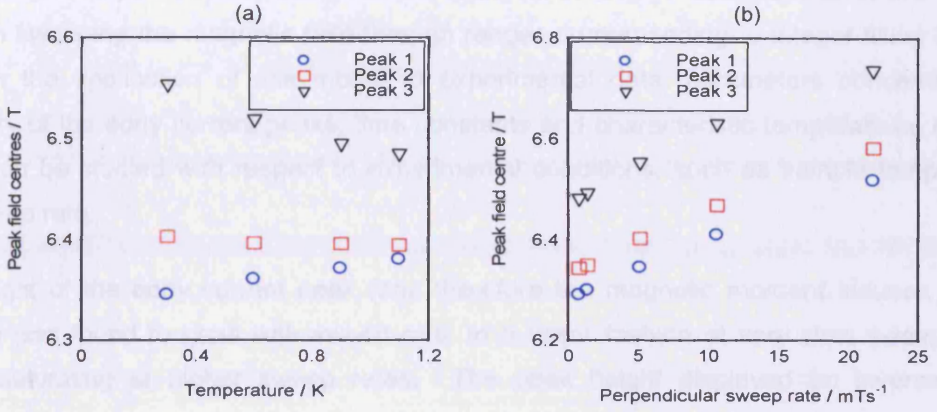

Figure 6.46: *Behaviour of peak field centre positions of individual Gaussian functions with respect to (a) temperature at a sweep rate of 5.18mTs^{-1}, and (b) sweep rate at T=0.3K.*

When first viewed the graph of Figure 6.46(a) appears rather odd, with all three centre positions following different behaviour as the temperature increases. However the displayed dependences are sensible given that it is known that the overall peak reduces in width with increasing temperature. As a result the outer peak centres (1 and 2) could be expected to approach the inner position (2), which should remain at the same value. This is seen experimentally: peaks 1 and 3 begin at outermost field centre positions at low temperatures and move inwards towards each other as the temperature rises, while peak 2 stays at the position. Figure 6.46(b) shows how all the centre positions of all three peaks rises with increasing sweep rate. Although this is not expected, it is known that the magnet used to acquire all data at Cardiff yields a shift in peak position for both up and down sweeps that increases for large sweep rates. This has been explained previously in section 5.1. All three centre positions appear to exhibit linear growth with similar gradients which suggests that this is indeed the cause; the slope of the line yields a time constant value of ~10s.

The fitting of a triple Gaussian to experimental data is convincing, but the reason for such a function and the behaviour of its components is unknown. As discussed in section 6.5.7 it is currently unknown why the eddy current peaks should exhibit a single Gaussian shape, let alone why three Gaussian functions should fit so well at filling factor 2! Van Zalinge *et al* [23] have also discovered a double peak structure at small integer filling factors in lateral photo-voltage measurements on GaAs/AlGaAs samples. It could be useful to study the contributions of the individual components further in order to gain more points on each graph, as well as testing other samples for this effect, but it is first necessary to understand the mechanism that governs the peak shape.

6.6 Summary and future work

Experiments conducted via high sensitivity torque magnetometry have been performed on GaAs/AlGaAs samples in order to investigate the onset of breakdown of 2DEG samples. A model has been constructed, based on the build up of charge accumulated at the sample edge on sweeping the magnetic field through ranges corresponding to integer filling factors. Through the application of this model to experimental data, parameters concerning the geometry of the eddy current peaks, time constants and characteristic temperatures emerge which can be studied with respect to experimental conditions, such as sample temperature and sweep rate.

The height of the eddy current peak (and therefore the magnetic moment induced on the sample) was found to grow with sweep rate, in a linear fashion at very slow sweep rates, before saturating at higher sweep rates. The peak height displayed an inverse linear dependence on the sample temperature. Similarly, the peak width ΔB was also found to grow and then approach saturation with increasing sweep rate, while exhibiting a 1/T temperature dependence.

The fitting parameter *a* was analysed with respect to a temperature dependence model [17]. Characteristic temperatures as high as 55K and conductivities of the order $(10^{-8} - 10^{-5})\Omega^{-1}$ were extracted from the model.

A number of time constants were obtained through different methods. The first could be found from the fitting parameter *b*. A second set of time constants was found through a series of measurements in which the sweeping magnetic field was paused at the peak height maximum and the signal as allowed to decay. Exponential decay curves were fitted to the signal. In some cases two separate decay regimes were observed. The first, occurring just after the magnetic field sweep was halted corresponded to a decay time constant of the order of seconds in which the most decay was seen. The decaying signal then moved into the second regime where the decay was very slow and the time constant was of the order of hours.

By plotting the fitting parameters *a* and *b* it was possible to extract characteristic temperatures. These temperatures generally fell in the range (0 – 1)K, and it was seen that those obtained through parameter *b* were usually slightly above those from parameter *a*.

The eddy current peak shapes and sizes were discussed with respect to a charge-up model. Limitations of this model have been highlighted, indicating where alterations must be incorporated to improve it.

The eddy current peak shape at filling factor 2 has been investigated. It is seen that a sum of three Gaussians function agrees convincingly to such peaks, and the contributions of each

individual peak, including height, width and centre position, have been examined with respect to varying temperature and sweep rate. Further measurements are suggested to provide additional information, as well as the importance of determining the mechanism behind such a peak shape.

The model as it stands seems to provide a reasonable explanation for the basic mechanisms induced in the quantum Hall regime. However some assumptions, for instance the form of the longitudinal conductivity, require refinement in order to bring about improvement. There are also several unknown values, for instance the channel width or critical current density for breakdown. At present these values must be estimated from other published work. Torque magnetometry has proved to be a very useful method in which to measure the macroscopic effects of induced eddy currents to a high sensitivity, with the additional advantage of requiring no contacts to the sample. However we obtain no information of the microscopic picture. It would therefore be very useful to have a more definitive picture of the current distribution around our particular samples including the channel width through which most of the current flows. Alternative experimental techniques which could be employed in order to achieve this could include linear-optic experiments [20] or scanning probe measurements [24, 25].

6.7 References

[1] G.E. Ebert, K. von Klitzing, K. Ploog and G. Weimann, *Journal of Physics C: Solid State Physics* Vol. 16, 5441 (1983).

[2] S. Komiyama, T. Takamasu, S. Hiyamizu, S. Sasa, *Solid State Communications* Vol. 54, 479 (1985).

[3] P. Streda and K. von Klitzing, *Journal of Physics C: Solid State Physics* Vol. 17, L483 (1984).

[4] D. C. Tsui, G. J. Dolan and A. C. Gossard, *Bulletin of American Physics* Vol. 28, 365 (1983).

[5] O. Heinonen, P. L. Taylor and S. M. Girvin, *Physical Review* Vol. B30, 3016 (1984).

[6] L. Eaves and F. W. Sheard, *Semiconductor Science and Technology* Vol. 1, 346 (1986).

[7] see references in [5]

[8] M. E. Cage, R. F. Dziuba, B. F. Field, E. R. Williams, S. M. Girvin, A. C. Gossard, D. C. Tsui and R. J. Wagner, *Physical Review Letters* Vol. 51, 1374 (1983).

[9] K. Guven and R. R. Gerhardts, I. I. Kaya, B. E. Sağol and G. Nachtwei, *Physical Review* Vol. B65, 155316 (2002).

[10] P. R. Morris et al, *Proceedings of the 24th International Conference on the physics of Semiconductors*, Aug 2-7 1998, Jerusalem, Israel.

[11] C. L. Jones, A. Usher, M. Elliott, W. G. Herrenden-Harker, A. Potts, R. Shepherd, T. S. Cheng and C. T. Foxon, *Solid State Communications* Vol. 97, 763 (1996).

[12] Y. Lu, *PhD Thesis*, 2002, see also B. I. Bleaney and B. Bleaney, *Electricity and Magnetism*, Third Edition, London, Oxford University Press, 1976.

[13] A. H. MacDonald, T. M. Rice and W. F. Brinkman, *Physical Review B* Vol. 28, 3648 (1983).

[14] Y. Lu, M. Elliott, K. L. Phillips, A. Usher, A. J. Matthews, J. D. Gething, M. Zhu, M. Henini and D. A. Ritchie, submitted to *Physical Review Letters*, April 2004.

[15] S. Takaoka, K. Oto, S. Uno, K. Murase, F. Nihey, and K. Nakamura, *Physical Review Letters* Vol. 81, 4700 (1998).

[16] V. M. Pudalov and S. G. Semenchinsky, *Solid State Communications* Vol. 51, 19 (1984).

[17] F. Y. Huang, *Physics Letters A* Vol. 294, 117 (2002).

[18] D. G. Polyakov and B. I. Shklovskii, *Physical Review B* Vol. 48, 11167 (1993).

[19] K. von Klitzing, *Surface Science* Vol. 113, 1 (1982).

[20] P. F. Fontein, P. Hendriks, F. A. P. Blom, J. H. Wolter, L. J. Giling and C. W. J. Beenakker, *Surface Science* Vol. 263, 91 (1992).

[21] F. Hohls, U. Zeitler, R. J. Haug and K. Pierz, *Physica B* Vol. 298, 88 (2001).

[22] F. Hohls, U. Zeitler and R. J. Haug, *Physica E* Vol. 12, 670 (2002).

[23] H. van Zalinge, B. Özyilmaz, A. Böhm, R. W. van der Heijden, J. H. Wolter and P. Wyder, *Physical Review B* Vol. 64, 235303-1 (2001).

[24] K. L. McCormick, M. T. Woodside, M. Huang, M. Wu, P. L. McEuen, C. Duruoz and J. S. Harris Jr, *Physical Review B* Vol. 59, 4654 (1999).

[25] S. Chakraborty, I.J. Maasilta, S. H. Tessmer and M. R. Melloch, *Physical Review B* Vol. 69, 073308 (2004).

Chapter 7: Noisy breakdown structure at filing factor $\nu = 2$

In the previous chapter saturation of the eddy current peaks was discussed and experimental data presented. Among the data were some interesting noise effects that are also thought to be a manifestation of breakdown, that is, the fine structure noise seen in samples NU2055 and A1157 at filling factor $\nu = 2$ only. Noise of this kind has been observed before in samples studied both in Cardiff and Exeter [1,2]; an example of which is given in Figure 7.1.

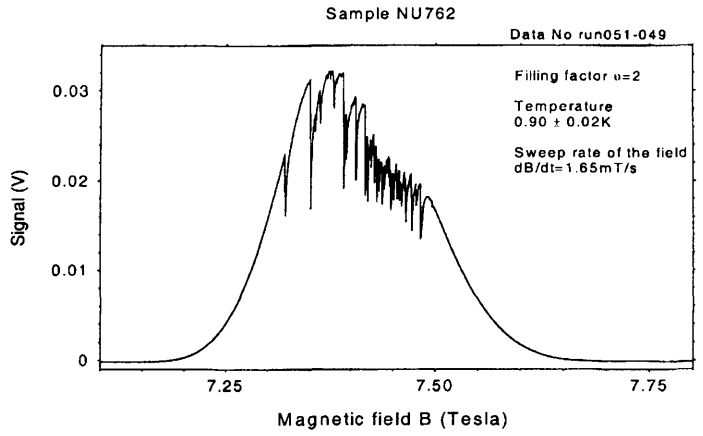

(a)

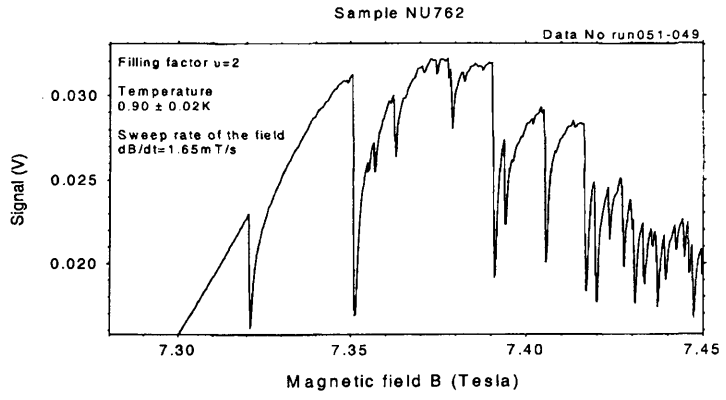

(b)

Figure 7.1: *An early example of the fine structure noise as seen by Y Lu [1, and see also 2] in a GaAs/AlGaAs sample labelled NU762: (a) the whole sweep; (b) an enlarged portion of the full sweep showing the noise in more detail. Calibration constant* $c \approx 7 \times 10^{-7}$ *Nm/V.*

The appearance of this noise could not be accounted for directly at the time and it was deemed necessary to investigate further. In order to acquire data of a higher quality (i.e. to record as many noise jumps as possible), it was necessary to improve the sensitivity of the torque magnetometer and the data logging equipment. As such the Mark IIIc probe was developed and built as described in Chapter 4, and the data logging programs were altered in order to improve the data acquisition rate. This would also allow the reproducibility of the noise to be verified.

In all cases it appears that a higher temperature noise-free regime exists and that noise develops upon lowering the temperature, accompanied by the development of the extra 'shoulders' seen each side of the peak as discussed in Chapter 6. This chapter discusses the appearance of the noise, and offers the concept of self-organised criticality as a possible description of macroscopic events.

7.1 Evidence of fine-structure noise

First we revisit some recent data as presented in Chapter 6 and display the noise observed at filling factor ν=2 for sample NU2055, shown in Figure 7.2.

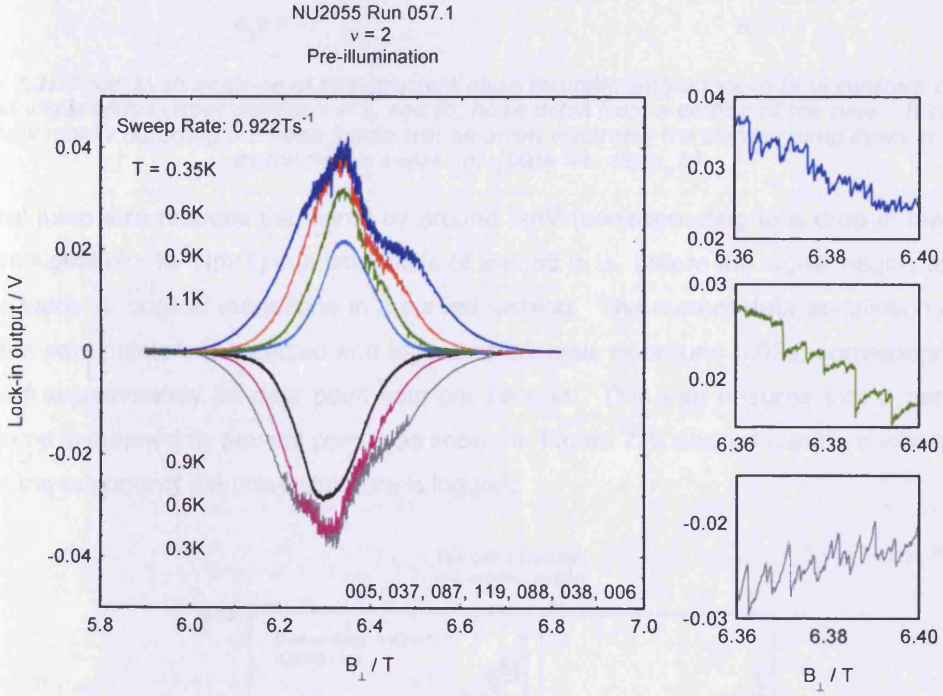

Figure 7.2: *Temperature dependence of ν = 2 for sample NU2055. As the temperature decreases from 1.1K it can be seen that the peak develops fine structure noise and simultaneously acquires one shoulder on each side. Calibration constant c ≈ 2.7×10⁻⁷ Nm/V.*

At higher temperatures (~1K), the eddy current signal takes the form of a simple, featureless, virtually single, peak. As the temperature is reduced a series of noisy jumps begins to occur, appearing first as only several quite large jumps down in signal across the peak, and building to a rapidly repeating succession of mainly smaller jumps. The signal then grows towards the original signal size. At base temperature (~0.3K), the noise occurs so frequently, and the build-up time is slow enough, that in some cases the signal never quite reaches its original size before another sudden reduction takes place. Figure 7.3 includes a close up of the noise to show its characteristics.

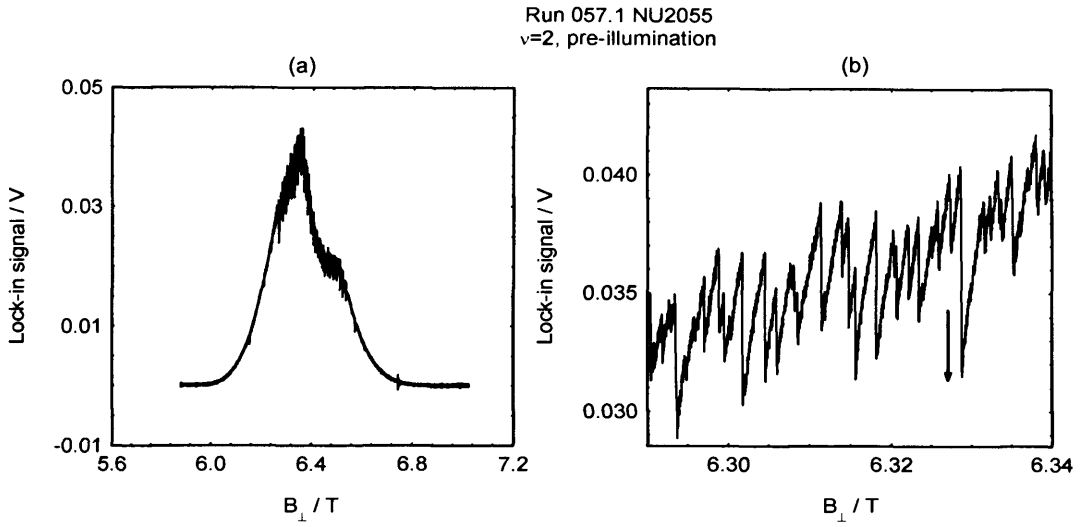

Figure 7.3: *Graph to show shape of fine-structure noise recorded with a lock-in time constant of 1ms, (a) the whole eddy current peak at ν = 2, and (b) noise detail from a portion of the peak. It can be seen how rapidly occurring the noise jumps are; an arrow illustrates the sudden jump down in signal as the field is swept up. [Data file: 083x_b]*

A typical jump size reduces the signal by around 5mV (corresponding to a drop in magnetic moment signal of ~10^{-9}Nm/T) in a time scale of around 0.1s, before the signal begins to grow back towards its original magnitude in a curved fashion. The current data acquisition rate is such that data points are collected and logged at intervals of around 0.02s, corresponding to a rate of approximately 50 data point sets per second. This rate ensures that a particular noise jump is mapped by several points, as shown in Figure 7.4, and we can be confident that at least the majority of the noisy structure is logged.

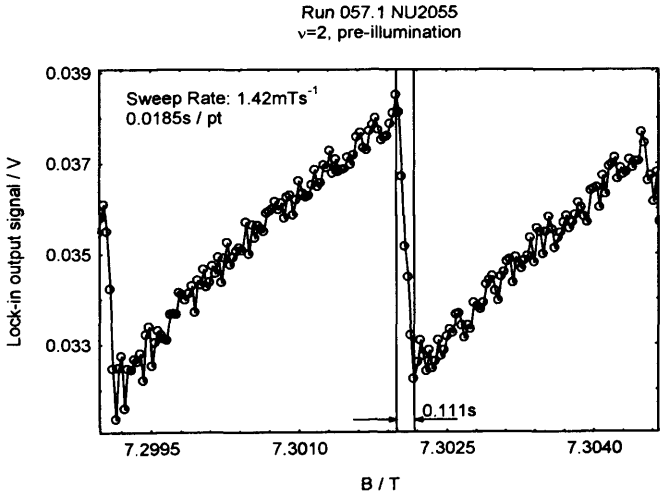

Figure 7.4: *Enlarged view of a single jump in signal with respect to total field B/T. The time between each data point, and that which elapses over a sudden jump (marked by a pair of vertical lines) can be calculated via the sweep rate when the change in field is known (lock-in time constant 1ms).*

Interestingly, as the noise begins to appear on the eddy current peak, the development of shoulders on either side of the peak also occurs at the same time, with the most well defined peak always occurring on the high field side, irrespective of the magnetic field sweep

direction. The peak, together with its shoulders, can be convincingly fitted with a function comprising three Gaussians and was presented previously in section 6.5.7.

The structure of the noise observed at filling factor $\nu = 2$ suggests a sudden charge redistribution from local areas of high charge density into the bulk. When the local charge density has been reduced below a critical level the discharge stops. Sweeping the magnetic field causes the charge to begin building up again until the critical point is exceeded, and the process starts again. It also appears that the sudden discharge followed by the gradual charge-up is not often accomplished in a single event. Rather, a single charge redistribution will often cause further sudden breakdowns, resulting in the noisy structure observed in the signal. These characteristics are the expected features observed in self-organised criticality, a model which will be introduced in the next section.

7.2 The concept of self-organised criticality

Self-organised criticality (SOC) is a fascinating concept originally introduced by Bak *et al.* [3,4] to explain the ubiquity of $1/f$ noise and has since been used to describe a variety of physical phenomena that advance to a critical state by means of a self-organised process. Bak argues that "*complex behaviour in nature reflects the tendency of large systems with many components to evolve into a poised, 'critical' state, way out of balance, where minor disturbances may lead to events, called avalanches, of all sizes.*" He argues that most of the changes in a system which can be described by SOC will occur via large catastrophic events rather than following a smooth and slow path. The system is termed self-organised because it reaches a state which is determined purely by the dynamical interactions between the separate components of the system and is insensitive to its initial conditions. The state is called *critical* because there are no characteristic time or length scales involved. First, we consider complexity, and how it can be defined.

In classical physics, the existing generally accepted laws of physics (for instance, the equations of Newton, Maxwell, Einstein, etc) are simple and capable of describing most phenomena in nature sufficiently well. However, when one attempts to solve a problem for more than two objects, the mathematics can become quite complicated, often requiring substantial computing power to provide only an approximate solution. Physics is reductionist, condensing the world down into fundamental particles described by fundamental laws. However, this is not the world we live in and we see around us a vast array of interacting systems each with their own characteristic dynamics: such systems with large variability are termed *complex.*

7.2.1 Complexity

Complexity is seen in many more areas than simply physics: millions of species in the biological world compete and interact with each other and the environment; the human body itself consists of an intricate array of interacting cells; history, with its assortment of wars, politics and religions represents another complex system involving individuals (with individual opinions), governments and economics.

How, then, can we arrive at such complexity if we begin with such simple deterministic laws? If we observe a system exhibiting such variation we can only learn by hindsight and cannot predict the future, because the actually observed event depended on the outcomes of so many other unpredictable events. As a result, nothing is reproducible and experiments cannot be performed.

There are four phenomenological examples of systems whose complexity cannot be described simply by the existing scientific laws. They are examples that appear everywhere and will be discussed below.

Catastrophic behaviour

Catastrophic behaviour is a manifestation of the composite nature of complex systems, where one part can affect the entire system by means of a domino effect. Typical examples of this behaviour include earthquakes, stock market fluctuations and mass extinctions. In the case of earthquakes, the size of the earthquake is recorded as a function of how frequently an earthquake of that size occurs.

It was found that every time there were around 10^n earthquakes of magnitude m (m integer), there were 10^{n-1} earthquakes of magnitude (m + 1). This distribution is known as the Gutenberg-Richter law and is illustrated in Figure 7.5 as a straight line on a double logarithmic (log-log) plot. The catastrophic behaviour can be seen as a few very large earthquakes at one extreme with a very large number of small earthquakes at the other extreme. This law suggests that the particularly complex system of the earth's crust, incorporating mountains, basins, lakes and many other structures can be described by a simple law. It also shows that large earthquakes follow the same law as small earthquakes, which has implications for scientists who study only large earthquakes in any detail without observing the wider picture.

Large events in systems displaying complexity are not periodic even if a clear probability distribution has been constructed; even though a long time may have passed since the last large event, this does not imply that that one should be anticipated soon. Also, large events should not be considered cyclical; if the average time between two large events is known, it is still not possible to predict the next large event in a specific timeframe. The regularity (not periodicity) of events suggests that the same mechanism is responsible for all scales.

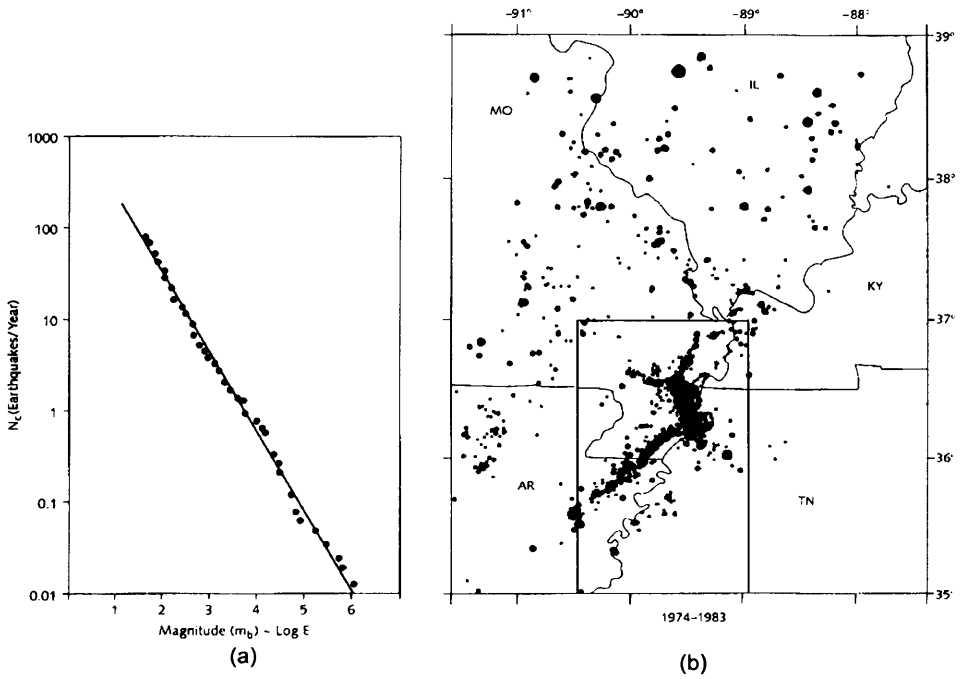

Figure 7.5: *Distribution of earthquake magnitudes in the New Madrid zone in the southeastern United States during the period 1974-1983, collected by Arch Johnston and Susan Nava of Memphis State University [5]. (a). Number of earthquakes N_c with a magnitude larger than a given magnitude m, fitted with the Gutenberg-Richter law. (b). Locations of the earthquakes used in plot (a). The size of the dots represents the magnitudes of the earthquakes.*

Our simple scientific laws express these phenomena as smooth continuous equations, so the occurrence of catastrophes is surprising. Lyell [6] proposes that change in a system is caused by processes with persistent rates which have not altered over time, for instance, the gradual formation of landscapes, rather than the cataclysmic event of Noah's flood. This proposal would seem sensible if one starts with the laws of physics which dictate smooth and gradual variations. In opposition, catastrophism claims that sudden cataclysmic events dictate most of the observed changes. However, this is mainly rejected since it evokes creationism, even though such events are actually observed.

Fractals

A *fractal* is a self-similar geometric shape containing features of all length sizes and the term was first used by Mandelbrot [7]. Examples of fractals include fjord length along Norway's coast, and mountain peak, cloud and galaxy size. When trying to measure the length of the Norwegian coast, if you have a picture of part of a fjord, the lengths on it are meaningless unless the picture includes a scale. The lengths measured depend on the resolution of that scale; a low resolution will produce a lower estimate than that found with a higher resolution.

To illustrate this, one can count how many boxes of a particular size δ are required to cover the coast. Figure 7.6 displays the coast line with some boxes placed over it. The smaller the box size, the more are required, and it follows that the length of the coast L as a function of

box size δ can be fitted with a straight line when plotted on a log-log plot (shown in Figure 7.6(b)).

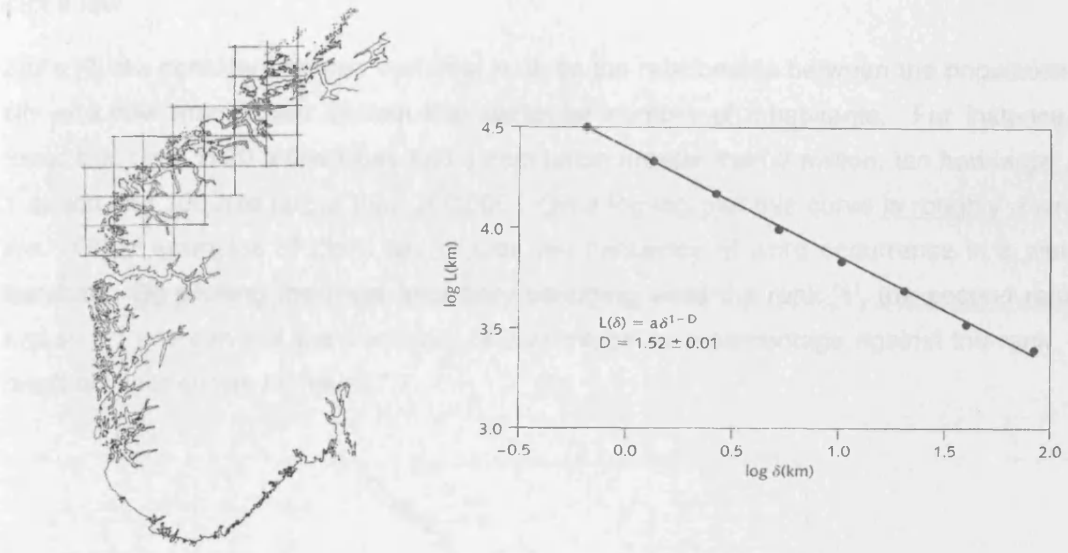

(a) (b)

Figure 7.6: *(a). The Norwegian coast [8]. Boxes have been added on part of the coast line, (b).The length L of the coast measured by covering the coast with boxes of various lengths δ*

If the coast was a straight line, the number of boxes required to cover the coast would be inversely proportional to δ, the measured length would then be independent of the box size and the curve would be flat. However, the boxes need to cover all the twists and turns of the coastline so the number required grows rapidly as the box size is reduced, which creates a straight line with a slope. This slope is the *fractal dimension* of the coast, which generally takes non-integer values. The fractal dimension of the illustrated piece of coast is given as 1.52, somewhere between a straight line and surface. Nothing in the accepted laws of physics lends itself to explain the origin of fractals.

1/f noise

Examples of 1/f noise include the flow of the River Nile, light emitted from quasars and highway traffic. The main characteristic of such noise is that it contains features of all sizes. Quasars will exhibit quick changes in signal over a several minutes, but also display slow variations of the order of years. In the same way that fractals display features of all sizes, 1/f noise displays features of all time durations. The signal can be a superposition of periodic signals of all frequencies, and the strength of the frequency component is larger for small frequencies. In this way the signal is inversely proportional to frequency, f, which is why it is termed 1/f noise. A simple illustration of 1/f noise would be that of the velocity of a car driving along a very busy road. There will be phases of movement and obstruction of varying duration which relate to the size of traffic jam encountered each time. 1/f noise is different to

random 'white' noise which has no slow variations and includes all frequencies in an equal amount. Although 1/f is observed in countless guises, its appearance is not understood.

Zipf's law

Zipf's [9] law considers human systems, such as the relationship between the population of a city and how many cities contain that particular number of inhabitants. For instance Zipf found that circa 1920 a few cities had a population greater than 2 million, ten had larger than 1 million and 100 had larger than 200,000. On a log-log plot this curve is roughly a straight line. Other examples of Zipf's law include the frequency of word occurrence in a piece of literature. By allotting the most frequently occurring word the rank '1', the second rank '2', and so on, one can plot the frequency of occurrence as a percentage against the rank. The result of this is shown in Figure 7.7.

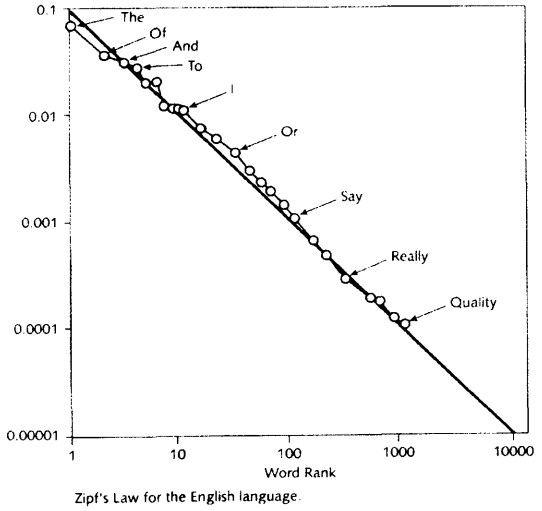

Figure 7.7: *Ranking of words in the English language. The vertical axis gives the frequency of occurrence as a percentage [5].*

Zipf's law is the regularity with which a logarithmic plot of frequency against rank provides a straight line with a gradient ≈1.

The laws described above are of a statistical nature; the frequency of earthquakes of a particular size (rather than *where* or *when* it occurs), or the number of cities with a particular population (rather than *why* the city has that population). These laws are distribution functions of measurable quantities, rather than predictions, so it follows that a theory to describe such effects must also be statistical.

7.2.2 What is *not* complexity?

Having discussed four key observations which define complexity, we now highlight a few effects which should not be considered complex.

Balanced systems

Balanced systems will not display complex behaviour as explained above. They are in equilibrium and are therefore called 'linear' systems: the system's response is proportional to the perturbation so a small perturbation of the system will only slightly disturb it. The phenomena described above cannot be described by equilibrium theories.

Chaos

Chaotic theory states that no matter how much is known about the initial conditions of a system we cannot predict the behaviour of the system. Feigenbaum [10], in his studies of populations, used the map

$$x_{n+1} = \lambda x_n (1 - x_n) \tag{6.49}$$

to construct a theory of transition from regular periodic behaviour to chaos. Rather than 1/f noise, chaotic systems exhibit a white noise spectrum. They do not build on past events and cannot evolve. However, complex behaviour does occur, just at the transition into chaos, i.e. complexity occurs at only one particular point and is not ubiquitous like catastrophes, fractals, 1/f noise and Zipf's law. Chaotic systems therefore depend on specific external parameters, whereas complex systems do not.

7.3 The sand-pile model

The simplest system which exhibits the features of self-organised criticality is described in the sand-pile model of Bak *et al.* An array of integers, h_n, represents the height of a pile of sand grains. A single sand grain is added to the pile from above at a regular time interval and at a random position. The sand-pile is therefore an *open* dynamical system (because the sand is added from the outside) with many degrees of freedom (provided by the separate sand grains). The critical factor in the sand-pile model is that of the incline variation over the pile of grains (or, angle of repose). As each sand grain is added, the system becomes a stationary state where the average amount of sand falling and the average slope of the pile become constant in time. As further sand is added, the system is transferred to a critical state, where the local slope exceeds some critical value. At this point sand will be redistributed in the form of avalanches so that the local slope shrinks just below the critical value. Redistribution of sand grains from this local area may increase the slope of a neighbouring region so that redistribution must also occur there. In this way, avalanches can spread through the whole pile via a domino effect leading to a chain reaction, which slows down as the system relaxes

below the critical point. In the meantime, the regular adding of a single grain of sand at random position begins to build the local slope in certain regions of the sand-pile and return it to the critical state. It is the large avalanches, rather than a gradual change which provide the global changes to the sand-pile. The outcome observed when a grain of sand is added to the pile relies on particular, and often minor, past events.

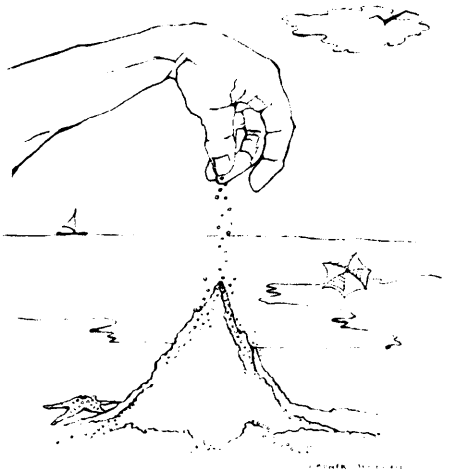

Figure 7.8: *The sand-pile [4]*

When the local slope exceeds the critical angle of repose through the adding of an extra grain of sand, it is expected that this grain of sand will cause the movement of a number of neighbouring grains until the state of the system becomes just about non-critical. However it cannot be known before-hand whether that one additional grain of sand will cause the shift of a single neighbouring grain, or an entire avalanche. The dynamics of the sand-pile cannot be predicted from the properties of the grains. This infers a lack of characteristic length scale which directly relates to a lack of characteristic time scale. It is then expected, and has been found by Bak *et al.* and Kadanov *et al.* [11], that the avalanche behaviour of a self-organised system can be described by a power law

$$N = A \cdot S^{-K} \tag{6.50}$$

where N is the number of avalanches, S is the size of the avalanche and A and K are constants. Then if N is plotted on a log scale against S, also on a log scale, the following straight line can be fitted:

$$\log(N) = \log(A) - K\log(S) \tag{6.51}$$

The straight line will fit for all data scales, and no scales along the line will diverge from it. However, this will not follow at large and small extremes. For instance, no fjord can be bigger than Norway, or smaller than a molecule of water; the largest earthquake is limited by the size

of the earth and also the size of the particles that constitute the earth. There will therefore be some divergence towards these length scales.

In the case of circulating eddy currents in a 2DEG within the quantum Hall regime, it is the redistribution of charge in the sample which is expected to move with avalanche-type characteristics as the magnetic field is swept, and the general qualities of the observed noise correspond to those observed in sand-piles [4] and magnetospheric activity [12]. When a critical Hall field is reached, charge is redistributed to the bulk through a series of avalanches; the sweeping magnetic field then tends to build up the charge again and the process is repeated. It is the discharge into the bulk at such critical thresholds that would infer a *self-organised* criticality in the experimental data presented. If the fine-structure noise does demonstrate self-organised criticality, a power law in the distribution of sudden jumps (N) and their sizes (S) would be expected, i.e. there should be many more small jumps than large jumps, but the large jumps supply the most change to the pile. The sizes of jumps will ultimately be limited, by the sample size at the large-scale end, and by the background noise magnitude at the small-scale end.

In this way sand-piles exhibit catastrophic behaviour because the number of avalanches as a function of avalanche size follows a power law. Fractal behaviour occurs since the avalanches of sand grains create fractal structures in the pile. Zipf's law is also obeyed: if the largest avalanche is ranked '1', and second largest '2', and so on, plotting the avalanche size as a function of rank on a log-log plot produces a straight line.

The data for samples NU2055 and A1157 have been analysed, and the statistics of the jump sizes examined. The procedure for analysis is detailed in section 7.4.

7.4 Statistical analysis: treatment of experimental data

Repeated sweeps over $\nu = 2$ at the same temperature and sweep rate show the same general features of the fine structure noise jumps although the noise itself is not duplicated *exactly* in the fine detail; the jump sizes and even position in field are similar each time but there is some variation. To be able to compare the patterns of the noise, the statistics of the jumps are analysed. This is accomplished through the use of some specially written computer code which treats each jump according to its magnitude.

The first piece of code, known as soc.cc and written in C++, reads through the data file of the eddy current peak looking for jumps in signal above a user-specified threshold. These jump size values are sorted into ascending order. The second piece of code, known as hist.cc, finds the range over which the jump sizes lie, and divides this range into a number of bins of equal width, where the number of bins is chosen by the user. The jump sizes are sorted into each bin according to size, and the number of jumps in each bin is counted; the outputted

data takes the form (bin centre value, number in bin). The codes of soc.cc and hist.cc are presented in Appendix 1.

An example of this analytic procedure is presented graphically below.

We begin with a typical field sweep in which the sample exhibits the fine structure noise, see Figure 7.9 (a). Trace (b) then shows all the jumps down in signal above a threshold of 0.6mV extracted from the signal and displayed as a function of magnetic field. The threshold value (of 0.6mV) was chosen as the level of noise away from the peak, therefore any change in signal smaller than this value would be discounted and attributed to background noise.

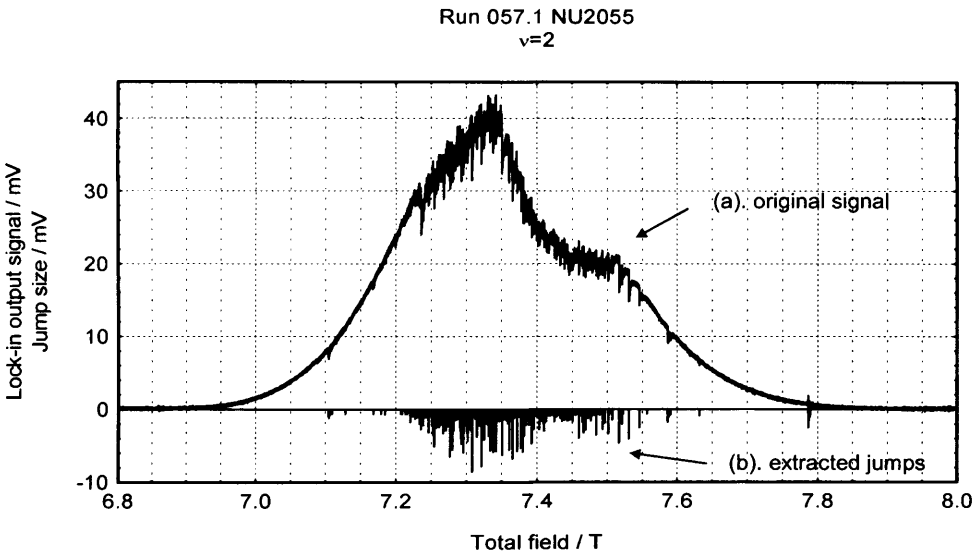

Figure 7.9: *Procedure for analysis of fine structure noise. Trace (a) shows the original signal of a positive field sweep at a rate of 1.42mTs^{-1} [083x_b], while trace (b) shows only the jumps larger than 0.6mV as they occur in the original signal [083x_unsorted]. The lock-in time constant for these measurements was set to its minimum, τ = 1ms; the calibration constant for all NU2055 data is 2.27x10^{-7} Nm/V*

For analysis purposes the jumps are then sorted into size order, as shown in Figure 7.10.

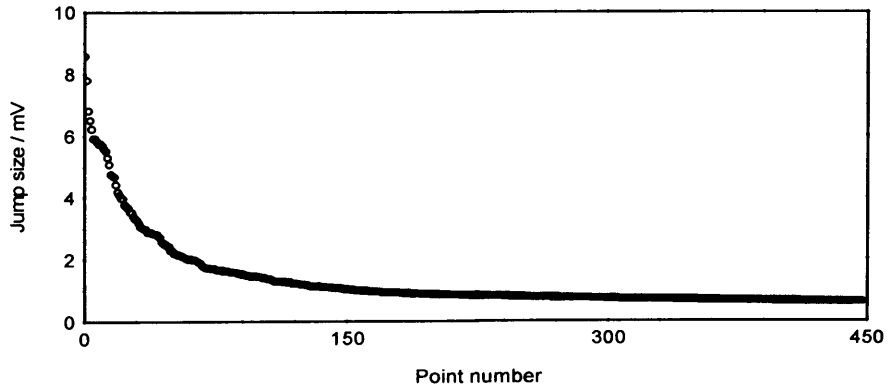

Figure 7.10: *The signal jumps (in mV), sorted into size order [083x_r].*

It can be seen that there are a few large jumps and many smaller jumps. The mV range covered by the array of jump sizes is then divided into a number of bins of equal width. In this case the jump sizes vary from 0.6mV to nearly 9mV and this signal range is divided into 10 bins of equal width. Each jump is then sorted into a particular bin depending on its size, and the number in each bin is counted. Clearly there will be a higher number of jumps in the bins at the lower end of the scale, and the number of jumps in each bin will decrease for larger jump sizes. The result of sorting the jumps into bins is shown in Figure 7.11.

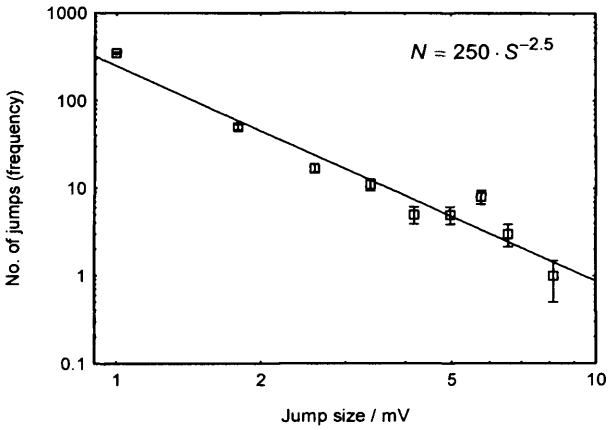

Figure 7.11: *Frequency of jumps plotted against the jump size (mV). The frequency of the jumps is plotted against the bin centre value [083x_hist].*

The 10 data points correspond to the 10 bins to which the jump sizes were sorted; one, at 7.4mV, contains no jumps for its range so has a value of zero which will not be displayed on the log scale. By plotting the frequency of jumps occurring on a log graph it is possible to show that the data follows a power law, as anticipated if the noise is a consequence of self-organised criticality [3, 4]. The fitted power law is also displayed in Figure 7.11.

Analysed data for samples NU2055 and A1157 is presented in the following section, in 7.5.1 and 7.5.2. Discussion of data for both samples follows in section 7.5.3.

7.5 Data Analysis

7.5.1 Sample NU2055

Eddy current signals recorded while sweeping the magnetic field over a peak corresponding to filling factor $\nu = 2$ for sample NU2055 have been analysed with respect to the fine structure noise as outlined in the previous section. Figure 7.12 displays the analysed data and the fitted power law for six peaks before illumination for sample temperatures of 0.3, 0.6 and 0.9K. Data for up and down sweeps showed very similar behaviour and exhibited very similar power law behaviour when fitted. Therefore up and down sweep data has been combined in one graph for each temperature.

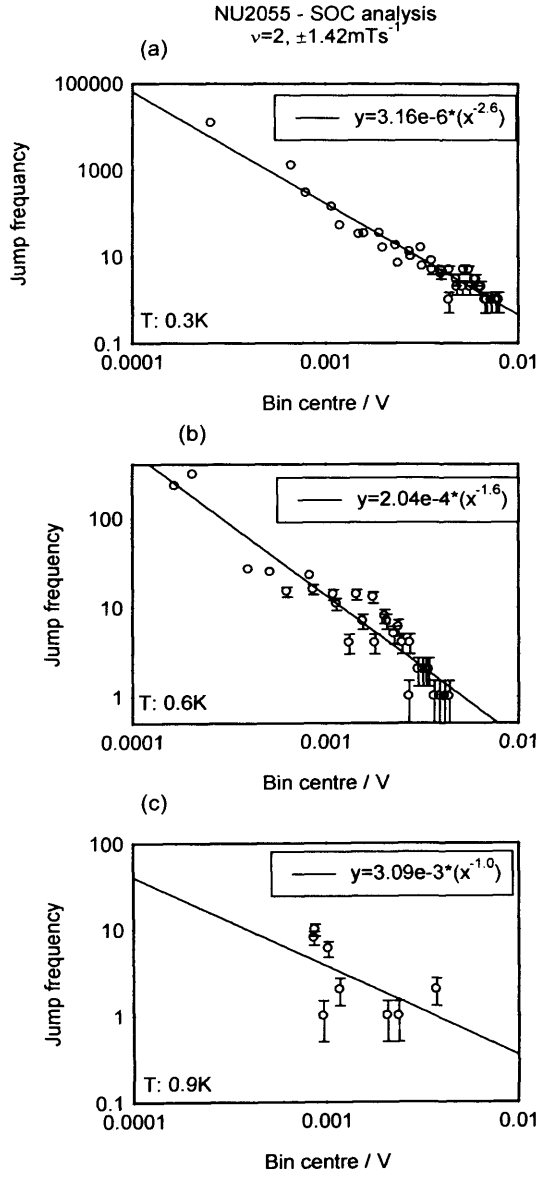

Figure 7.12: *Distribution of jump sizes across eddy current peak ν=2, pre-illumination. at a sweep rate of ± 1.42mTs^{-1}. Jump sizes have been sorted into 1 of 20 bins depending on their size. The frequency (number of occurrences) of jumps is then plotted against bin centre (the middle value of the bin width. Temperatures are marked: 0.3K (a), 0.6K (b) and 0.9K (c).*

Power laws have been fitted to the results in Figure 7.12; there were so few jumps at 0.9K (see bottom-left graph of Figure 5.31 for raw data) that only a few bins contain any jumps. Error bars have been added to the data, where the error takes the value $(N)^{0.5}$ where N ≡ jump frequency, or number of jumps.

Noise-analysed data for the same filling factor, sweep rate and temperatures, but *after* illumination are presented below in Figure 7.13. Again, data from up and down sweeps have been combined to improve the statistics.

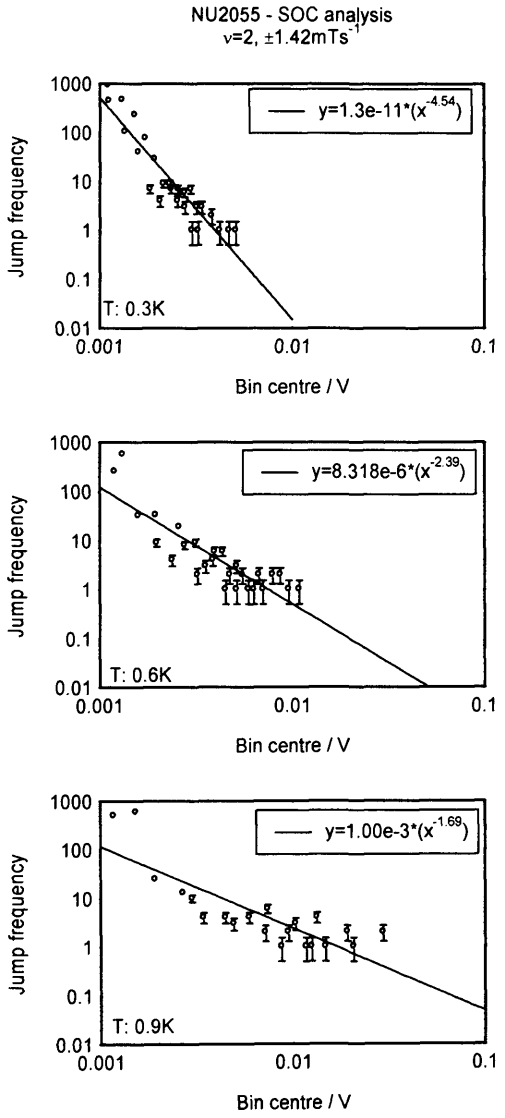

Figure 7.13: *Distribution of jump sizes across eddy current peak ν=2, post-illumination, at a sweep rate of ±1.42mTs⁻¹.*

It appears that the data follows power law behaviour fairly closely and the power to which the distribution adheres decreases with increasing temperature.

7.5.2 Sample A1157

Evidence of noisy discharge was also seen at filling factor ν=2 for sample A1157. Figure 7.14 below shows the number of jumps as a function of size, fitted with a power law, as for Figures 7.12 and 7.13.

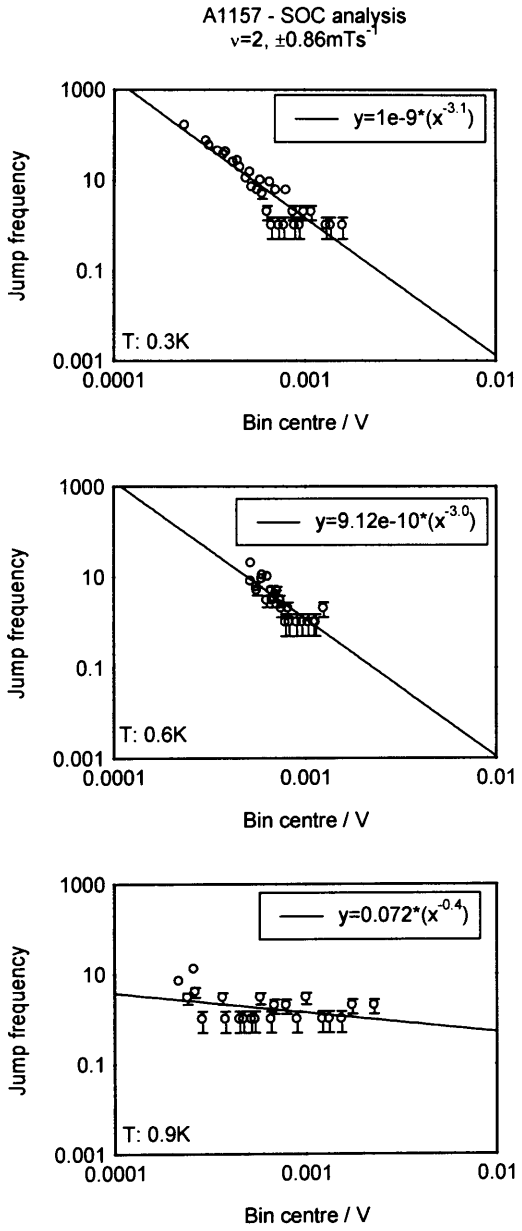

Figure 7.14: *Distribution of jump sizes across eddy current peak ν=2 of sample A1157 at a sweep rate of ± 0.86mTs^{-1}.*

Again, it can be seen that the data points follow a power law very well. Additional data is presented below in Figure 7.15 for sample A1157 at a slower sweep rate.

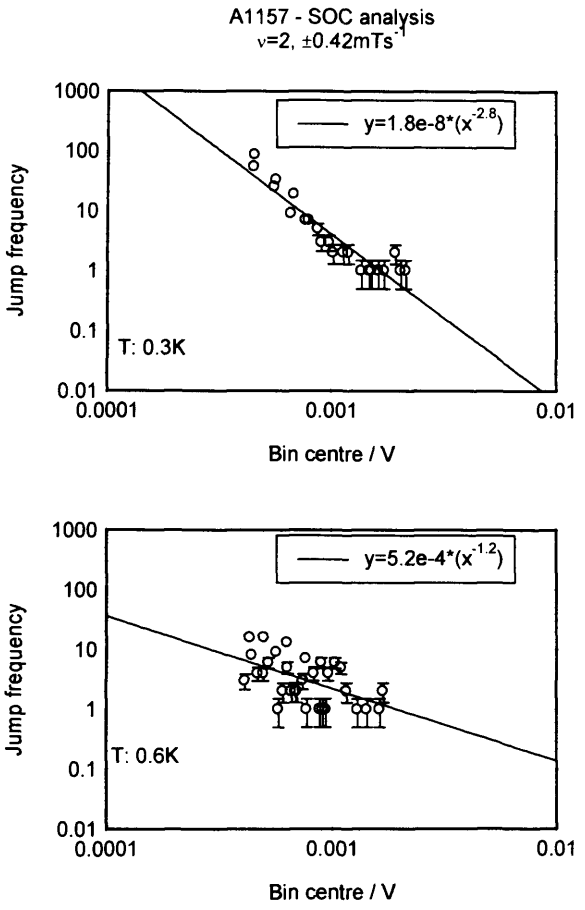

Figure 7.15: *Distribution of jump sizes across eddy current peak ν=2 of sample A1157 at a sweep rate of ± 0.42mTs^{-1}.*

Although the exponent of the power law reduces with increasing temperature, it can be seen that the actual power value is similar at a different sweep rate for a given temperature. This is an important property of a system exhibiting self-organised criticality in that the avalanche behaviour of the discharge does not depend on the driving mechanism, i.e. the sweep rate. A slight variation in the value of the power could suggest that the system is not being driven slowly enough. Further measurements at varying sweep rates and improved data acquisition rates would provide more information for this observation and allow more thorough analysis.

7.5.3 Discussion of results

It has been shown that the jump sizes of the fine structure noise observed at filling factor $\nu=2$ closely follow a power law in two separate samples, one of which was also illuminated. The noise is thought to be due to a sudden local redistribution of charge occurring as a result of a critically high electric field. As the magnetic field is swept, charge is built up around the edge of the sample, therefore inducing a perpendicular Hall electric field. This charge build up continues to grow with magnetic field until the electric field has reached some critical value, at which point an amount of charge is rapidly redistributed to the bulk. Since the magnetic field continues to sweep, the process begins again and charge builds up at the edge of the sample until the critical point is reached and charge redistribution again occurs.

This behaviour has been compared with the sand-pile model of self-organised criticality [3]. In our case the magnetic field is the driving mechanism and can be compared with the rate at which sand is added to the pile. In the sand-pile model the speed at which the sand is added plays no role and the pile continues to organise itself into a critical state with avalanches of all sizes [4]; analysis of the jump sizes exhibited by the 2DEG sample confirms that the range of jump sizes (charge redistributions) remains largely unaffected for different sweep rates and the data continues to follow a power law, indicating that the system has self-organised into a critical state. The sand-pile model counts the number of avalanches of particular sizes that occur when a specific parameter (the angle of repose) exceeds a critical limit. At this point an avalanche occurs to reduce this parameter to just below the critical value. When the pile has become adequately shallow at a particular point, the avalanche will slow to a stop. In the same way, charge redistributions in the 2DEG sample allow local relaxation of the electric field to just below its critical value: the jump size, rather than redistributing *all* charge and reducing the output signal to zero, causes a decrease in electric field that returns it to a sub-critical state. For an avalanche to occur at a particular area on a sand-pile a vast number of prior events must have occurred to cause that area to reach the critical point; in the same way, the amount of charge built up in a local area of sample relies on the previous history of that area and surrounding areas. Both systems have 'memory' and each past event has made a crucial contribution to the current state. If only a single prior event had occurred slightly differently, the pattern of events would have taken an entirely different course. This explains why the noise jumps can be reproduced on a qualitative scale, but not on a detailed quantitative scale.

It was possible to extract more noisy jumps for sample NU2055 than A1157; this was mainly due to the reduced background noise observed during experiments on this sample. NU2055 was tested using the newly developed Mark IIIc probe, which was more sensitive while also providing a reduction in background noise. Therefore, the threshold value (below which any jumps in signal are neglected) could be chosen as a smaller quantity for data from sample NU2055 which implies that smaller jumps will be included in the analysis.

Fewer jumps were observed as the temperature increased; this was expected since inspection of the peaks (see for instance Figures 5.20 and 5.28) shows that the noise begins to develop at around 0.9K as the temperature is reduced.

The power value of the fitted power laws appears to take values between 1 and 5. This value is generally slightly less for down-sweeps than for up-sweeps, and decreases with increasing temperature.

The actual microscopic process through which local edge charge is suddenly dissipated from into the bulk is unknown, although several models describe possible methods.

The quasi-elastic inter-Landau level scattering model of Eaves and Sheard [13] suggests that breakdown of the quantum Hall effect is due to transitions of electrons from the highest filled to the lowest unfilled Landau level, induced by critically high electric fields. When no scattering is permitted, the Landau levels are simply separated by an energy $\hbar\omega_c$. The distance over which an electron may tunnel is controlled by the requirement of spatial overlap of neighbouring states between which the electron tunnels and the electric (Hall) field must provide an energy difference of $\hbar\omega_c$ across this distance. The critical field, E_c, is then given as

$$E_C = \frac{\hbar\omega_c}{el_B\left((2n+1)^{1/2}+(2n+3)^{1/2}\right)},$$

where the denominator includes the spatial overlap of the two wavefunctions, approximated by the semi-classical cyclotron orbit. At this critical electric field, electrons can tunnel from one Landau level to the level above. Tunnelling of electrons is enabled by the emission of acoustic phonons, as well as via impurities, charge inhomogeneities and many-body effects, and these processes ensure momentum is conserved.

Through the use of numerical simulations, Tsemekhman *et al* [14] have constructed a theory in which breakdown of the quantum Hall effect is explained through the sudden formation of a conducting path across the sample which allows electrons to travel from one side to the other, dissipating energy. Incompressible insulating regions percolate the sample and are responsible for the quantum Hall effect; they separate compressible regions that behave like metallic liquids. When the sample is injected with a high enough current, the insulating region breaks down and the conducting regions are joined. A metallic path percolates the sample between opposite edges, and dissipation is suddenly established. Tsemekhman *et al* argue that the process of connection of metallic regions of the sample must take an avalanche form. The local electric field of a particular insulating region separating two metallic regions is much larger than the average Hall field of the sample. Therefore the average Hall field is only required to rise by a small amount in order to induce breakdown in the local area, allowing the

adjacent metallic areas to join up. The high local electric field of the former insulating region is then expelled resulting in a further increased local field in a newly-formed insulating region, which facilitates more avalanche-type connections, as the current rises. This model suggests that small breakdowns occur in multiple regions which spread in an avalanche-type way, which would correspond to the structural form of the noise observed in our experiments. However, it is not possible to distinguish which model could describe the noise detected through our measurements.

The breakdown of the integer quantum Hall effect has been extensively investigated, but no theory has been constructed as yet that adequately explains the origin of the phenomenon. In addition, many effects associated with breakdown have been observed, but no single model is able to describe them all.

7.5.4 Time constant variation over peak

By fitting an exponential curve to a small growing portion of the peak just after the sudden noise decay, it is possible to extract the time constant for that particular portion (the peak must first be transformed so that the signal varies with time rather than field). If this process is repeated over the range of the curve, a map of the time constants can be constructed to see if it varies in any particular, reproducible way across the peak. Figure 7.16 illustrates how an exponential curve can be fitted to an individual noisy jump.

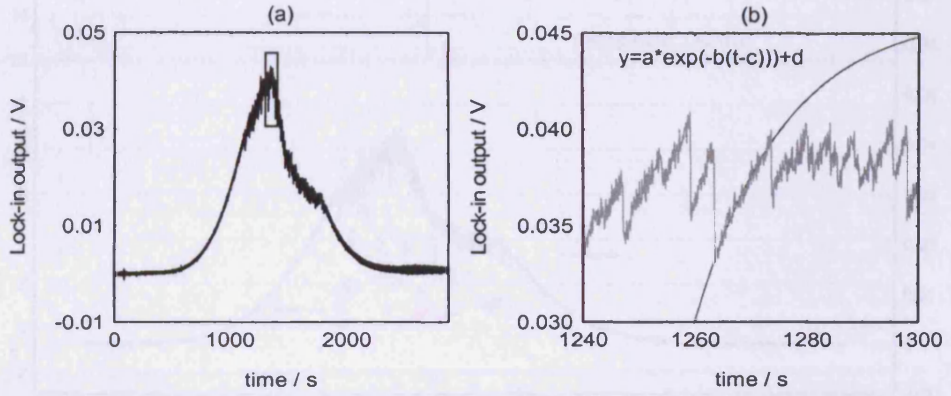

Figure 7.16: *Fitting an exponential curve to the re-growth of the signal: (a) the peak is transformed so that it is displayed as a function of time, rather than magnetic field (a box marks the area of the peak shown in (b)); (b) an exponential function of the form shown is fitted just after a noisy decay, in order to extract the time constant of the re-growth. The time constant is taken as (1/b).*

The procedure mentioned above was repeated over the peak of filling factor $\nu=2$ of sample NU2055, at a temperature of 0.3K and sweep rate 0.39mTs^{-1}. Figure 7.17 displays the result of a particularly thorough analysis of such data for sample NU2055.

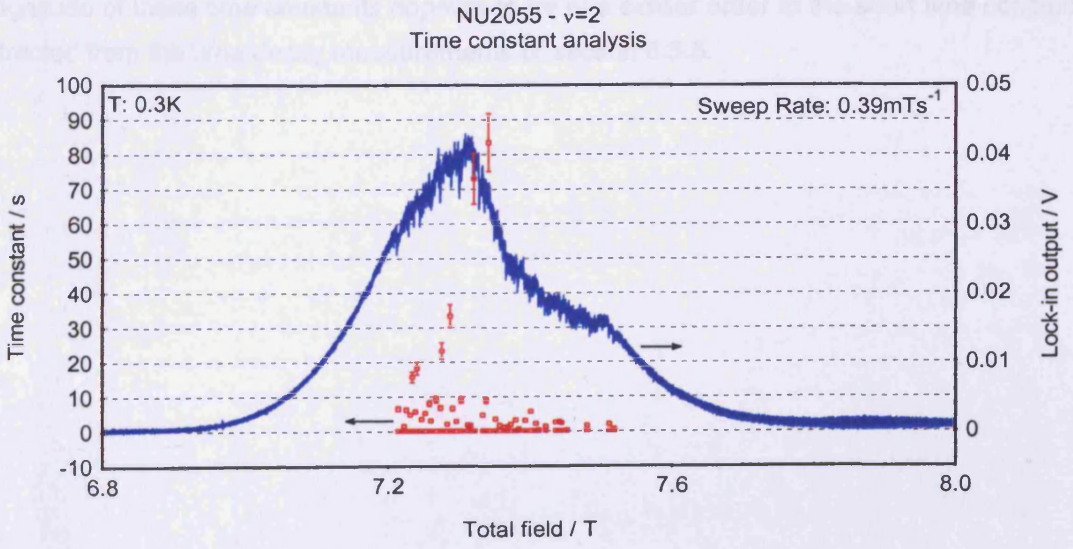

Figure 7.17: *Variation of time constant over the width of the $\nu=2$ peak at 0.39mTs^{-1}, as a function of magnetic field. The peak signal value (in V) is displayed on the right-hand axis.*

The time constants extracted from exponential fits to growing portions of the signal appear to contain errors that scale with the time constant size at approximately 20%. This seems

sensible when one considers that the long time constants are extracted from portions of charging-up signal that are quite linear in shape. In this case, errors obtained from exponential fits will be larger than those obtained to more curved portions (with smaller time constants), where the exponential form is more defined. Figure 7.18 below shows the same analysis performed on similar data recorded at a sweep rate of $1.42mTs^{-1}$ and a temperature of 0.3K.

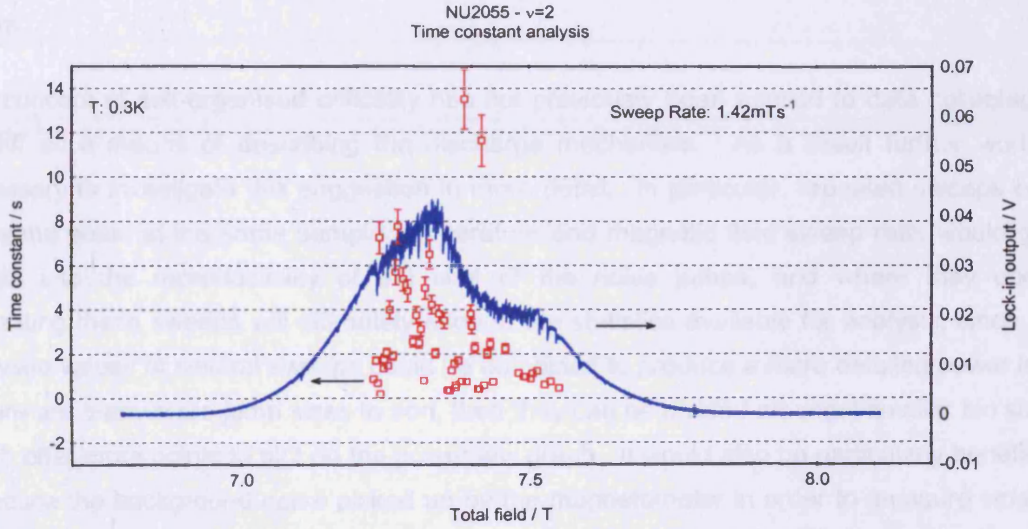

Figure 7.18: *Variation of time constant over the width of the v=2 peak at $1.42mTs^{-1}$, as a function of magnetic field. The peak signal value (in V) is displayed on the right-hand axis.*

It can be seen that there is an array of values for the time constant in the range (0.5 – 85)s, although the majority lie in the range of several seconds. The largest time constants seem to appear towards the centre of the range, as the signal reduces steeply just past the peak. The magnitude of these time constants appears to be of a similar order to the short time constants extracted from the time decay measurements of section 6.5.5.

7.6 Summary and future work

The appearance of noisy fine structure of the eddy current peaks of filling factor $\nu=2$ has been presented and discussed for two independent samples. This noise has been attributed to local discharge into the bulk of the sample occurring when the local electric field reaches a critical value. This mechanism has been compared to the sand-pile model of self-organised criticality. Time constants of individual noisy jumps have also been extracted across the peaks.

The concept of self-organised criticality has not previously been applied to data collected at Cardiff as a means of describing the discharge mechanism. As a result further work is necessary to investigate this suggestion in more detail. In particular, repeated sweeps over the same peak, at the same sample temperature and magnetic field sweep rate, would give insight into the reproducibility of the size of the noise jumps, and where they occur. Repeating these sweeps will ultimately expand the statistics available for analysis, since the analysed values of several sweeps could be combined to produce a more detailed power law: if there are many more jump sizes to sort, then they can be divided amongst smaller bin sizes which offer more points to plot on the power law graph. It would also be particularly beneficial to reduce the background noise picked up by the magnetometer in order to measure smaller jumps, and again provide additional contributions to the power law at the small-scale end.

7.7 References

[1] Y. Lu, PhD Thesis: *Study of the quantum Hall effect using a contactless method*, Cardiff University (2002).

[2] Y. Lu, M. Elliott, W. G. Herrenden-Harker, K. L. Phillips, A. Usher, A. J. Matthews, J. D. Gething, M. Zhu, M. Henini and D. A. Richie, *submitted to Physical Review Letters*, 2004.

[3] P. Bak, C. Tang and K. Wiesenfield, *Physical Review A* Vol. 38, 364 (1988).

[4] P. Bak, *How nature works: The science of self-organized criticality.* Oxford: Oxford University Press, 1997.

[5] A. C. Johnston and S. Nava, *Journal of Geophysical Research* Vol. 90, 6737 (1985), *as quoted in Ref. [5]*

[6] C. Lyell, *Principles of Geology 12th ed.*, London: John Murray, 1875, *as quoted in Ref. [5].*

[7] B. Mandelbrot, The Fractal Geometry of Nature, New York: Freeman, 1983, *as quoted in Ref. [5].*

[8] J. Feder, Fractals, New York: Plenum, 1988, *as quoted in Ref. [5].*

[9] G. K. Zipf, Human Behaviour and the Principle of Least Effort, Cambridge MA: Adison-Wesley, 1949, *as quoted in Ref. [5].*

[10] M. J. Feigenbaum, Journal of Statistical Physics Vol. 19, 25 (1978), *as quoted in Ref. [5].*

[11] L. P. Kadanov, S. R. Nagel, L. Wu and S. Zhou, *Physical Review A* 39, 6524 (1989), *as quoted in Ref. [5].*

[12] S. C. Chapman, Physics of Space Plasmas (MIT Center for Theoretical Geo/Cosmo Plasma Physics, Cambridge, MA, 1998), p. 67, 15, *as quoted in Ref. [5].*

[13] L. Eaves and F. W. Sheard, *Semiconductor Science and Technology* Vol. 1, 346 (1986).

[14] V. Tsemekhman, K. Tsemekhman, C. Wexler, J. H. Han and D. J. Thouless, *Physical Review B* Vol. 55, R10201 (1997).

Appendix: Code used in statistical analysis of SOC noise

The following pieces of code are written in C++ and have been annotated to clarify analytical procedures used in Chapter 7.

SOC.CC

```
// soc
// Finds sudden jumps in a generic signal versus time and
// sorts jump sizes into order if -s switch used.
// Usage: soc -f infile.dat -o outfile.dat -t threshold -s -r
// the -s option is to sort the data in size order
// additional to the -s flag, use the -r option to make the sort in reverse order
// (c) M Elliott March 2002
// Fri Jul 26 15:03:33 2002
// Thu Feb 12 10:24:48 GMT 2004 for check of PRL submission

#include <iostream>
#include <fstream>
#include <cmath>     // fabs needed
#include <vector>
#include <algorithm>
#include <string>
#include </home/orion/spxpj/kate/getopt.h>

using namespace std;

//#include "mystring.h"

const double PI = 3.141592653589793238462 6;

// Globals ...
string input_filename;
ifstream infile;          // logical name of input file
vector<double> B,G;  // data arrays
string output_filename;
ofstream outfile;         // logical name of output file
double threshold;         // threshold for a jump

//extern char *optarg;
//extern int optind, optopt, opterr;

bool sort_flg, errflg, rev;


// Start of main ...
int main(int argc, char* argv[]) {

        int c;
        // get command line parameters ...
        while ((c = getopt(argc, argv, ":sf:o:t:r")) != EOF) {
                switch(c) {
                case 't':                                       // threshold switch
                        threshold=atof(optarg);                 // reads in threshold value
                        //cout << "threshold is " << threshold << endl;
                                break;
                case 'r':                                       // reverse sort switch
                        rev=true;;
                        break;
                case 's':                                       // sort switch
                        sort_flg=true;
                        //cout << "data will be sorted" << endl;
                        break;
                case 'f':                                       // input file switch
```

```
                    input_filename = optarg;
                    //cout << "filename is " << input_filename << endl;
                    break;
            case ':':
                    cerr << "-" << char(optopt) << " without parameter" << endl;
                    errflg++;
                    break;
            case 'o':                                   // output file switch
                    output_filename = optarg;
                    //cout << "output filename is " << output_filename << endl;
                    break;
            case '?':
                    cerr << "unknown switch -" << char(optopt) << endl;
                    errflg++;
                    break;
            case 'h':
                    errflg++;
                    break;
            }
        }
        if (errflg) {
        cerr << "Saves values of sudden jumps (greater than a threshold) in a signal to file." << endl;
                cerr << "Usage: soc -f infile.dat -o outfile.dat -t threshold -s" << endl;
                cerr << "       use the -s option to sort the data in size order" << endl;
 exit(2);
 }

        // try to open file ...
        infile.open(input_filename.c_str());
        // check that file is there ...
        if (!infile) {
                cerr << "No such file\n";
                exit(1);
        }

// then read in the data ...
        while (!infile.eof()) {
        char c; char tempstring[256]; double temp; // to read in data
// check for comment lines ...
        c=infile.peek();
        switch (c) {
   case '#': infile.getline(tempstring, 256);
        cout << tempstring << endl;
            break;
   case '/': infile.getline(tempstring, 256);
       cout << tempstring << endl;
       break;
   case 13:  infile.getline(tempstring, 256);
       //cout << "13";
            break;
   case 10:  infile.getline(tempstring, 256);
            //cout << "LF";
            break;
   case EOF: break;

                default:  infile >> temp; // field
      // cout << "B " << temp;
                B.push_back(temp);
       infile >> temp; // x-signal
      // cout << "  x " << temp << endl;;
            G.push_back(temp);
       //infile.getline(tempstring, 256);
                    //int t;
                    //cin >> t;
                    //infile >> temp; // y-signal
                    //cout << "  y " << temp << endl;
       break;
```

```
  }
 }
 infile.close();

 // find max and min values...
        float Gmin = *min_element(G.begin(), G.end());
 //cout << "The smallest element is " << Gmin << endl;
        float Gmax = *max_element(G.begin(), G.end());
 //cout << "The largest element is " << Gmax << endl;

 // Form differences - size T of jumps
        vector<double> T;
 // Determine where change in G is greater than a threshold value. This means
 // there is a jump of some sort.
        for (unsigned int i=0; i<G.size()-1; i++) {
        double dG=(G[i+1]-G[i]);

                if (threshold<0) {              // look for -ve jumps
                        if (dG<threshold) {             // big enough jump
                          T.push_back(dG);
                        }
                        else {
                                T.push_back(0);
                        }
                }

                if (threshold>0) {              // look for +ve jumps
                        if (dG>threshold) {             // big enough jump
                          T.push_back(dG);
                        }
                        else {
                                T.push_back(0);
                        }
                }
 }
 // Sum consecutive jumps ...
        double temp=0;
        for (unsigned int i=0; i<T.size(); i++) {
                if (T[i]!=0) {
    temp=temp+T[i];
                        T[i]=0;
                }
                else {
                        T[i]=temp;
                        temp=0;
                }
        }

 // try to create output file ...
        outfile.open(output_filename.c_str());
 // check file opened OK ...
 if (!outfile.is_open()) {
  cout << "Error opening file"; exit (1);
 }
 // sort data ...
  if (sort_flg) {
                  sort(T.begin(), T.end());
                  if (rev) {
                    reverse(T.begin(),T.end());
                  }
         }

 // save data in descending order ...
        unsigned int count=0;
 //     outfile << "// Threshold: " << threshold << endl;
        for (unsigned int i=0; i<T.size(); i++) {
   if (sort_flg) {
```

```
                        if (T[T.size()-1-i]!=0) {
                                count++;
                                outfile << count << "  " << fabs(T[T.size()-1-i]) << endl;
                        }
        }
                else {
                  outfile << B[i] << "  " << T[i] << endl;
                //fabs(S[i]) << endl;
                }
 }


 outfile.close();

 for (unsigned int i=0; i<T.size()-1; i++) {
   //cout << S[i] << endl;

 }

}

/*

Note: const char* c_str() const;

For compatibility with "older" code, including some C++ library routines, it is sometimes necessary to
convert a string object into a character array ("C-style string"). This function does the conversion. For
example, you might open a file stream with a user-specified file name:

string filename;
cout << "Enter file name: ";
cin >> filename;
ofstream outfile (filename.c_str());

*/
```

HIST.CC

```
// hist
// takes an array of sorted jump sizes
// sorts into a user-defined number, n, of equally spaced bins
// usage: hist.exe infile.dat n > outfile.dat
#include <iostream>
#include <fstream>
#include <sstream>
#include <string>
#include <cmath>
#include <vector>
#include <algorithm>

using namespace std;

int main(int argc, char* argv[]) {

 vector<double> y;          // original data array
 vector<int> N;    // number in bin

        // read in data ...
 if (argc != 3) {
   cout << "Usage: hist2 input.dat nbins," << endl;
   cout << "       where nbins is the number of bins required." << endl;
   cout << "Sorts the second column data into (ascending) values" << endl;
   cout << "and outputs pairs (bin value, number in bin)" << endl << endl;
   exit(1);
 }
```

```
  string infilename=argv[1];
  ifstream infile;                          // logical name of the file
  int nbins = atoi(argv[2]);   // number of bins

          // try to open file ...
          infile.open(infilename.c_str());
          // check that file is there ...
          if (!infile) {
                  cerr << "No such file\n";
                  exit(1);
          }

           double temp;                  // to read in data

          // then read in the data ...
      while (!infile.eof()) {

    // check for comment lines ...
    infile >> temp; cout << temp;
    infile >> temp; y.push_back(temp);

      }
   infile.close();

  // Output details in the output file ...
  cout << "# Histogram of " << infilename  << endl;
  cout << "# Number of bins: " << nbins << endl;
  // find max and min ...
  float ymin = *min_element(y.begin(), y.end());
  cout << "# The smallest element is " << ymin << endl;
  float ymax = *max_element(y.begin(), y.end());
  cout << "# The largest element is " << ymax << endl;
          cout << "# Original number of data points " << y.size() << endl;

          // initialise histogram ...
          for (unsigned int i=0; i<nbins; i++) {
                  N.push_back(0);
          }
//
          sort(y.begin(), y.end());
          double w=(ymax-ymin)/nbins; // bin width
          // fill the bins ...
          for (unsigned int i=0; i<y.size(); i++) {
                  //cout << y[i] << " " << endl;
                  int bin=(y[i]-ymin)/w; // calculate which bin
                  N[bin]++;
          }

          for (unsigned int i=0; i<N.size(); i++) {
                  cout << (ymin+w/2) +i*w << " " << N[i] << " " << endl;
          }

   return(0);

}
```